









# NAVAL POSTGRADUATE SCHOOL

## Monterey, California



# THESIS

THEORETICAL MODELING OF FLUID INTERACTIONS  
PRODUCED BY SHIP BOW THRUSTERS

by

Thomas Charles Cooper

March 1982

Thesis Advisor

R. H. Nunn

Approved for public release; distribution unlimited

T204006



REPORT DOCUMENTATION PAGE		READ INSTRUCTIONS BEFORE COMPLETING FORM
1. REPORT NUMBER	2. GOVT ACCESSION NO.	3. RECIPIENT'S CATALOG NUMBER
4. TITLE (and Subtitle) Theoretical Modeling of Fluid Interactions Produced by Ship Bow Thrusters		5. TYPE OF REPORT & PERIOD COVERED Master's Thesis March 1982
		6. PERFORMING ORG. REPORT NUMBER
7. AUTHOR(s) Thomas Charles Cooper		8. CONTRACT OR GRANT NUMBER(s)
9. PERFORMING ORGANIZATION NAME AND ADDRESS Naval Postgraduate School Monterey, California 93940		10. PROGRAM ELEMENT, PROJECT, TASK AREA & WORK UNIT NUMBERS
11. CONTROLLING OFFICE NAME AND ADDRESS Naval Postgraduate School Monterey, California 93940		12. REPORT DATE March 1982
		13. NUMBER OF PAGES 115
14. MONITORING AGENCY NAME & ADDRESS (if different from Controlling Office)		15. SECURITY CLASS. (of this report)
		15a. DECLASSIFICATION/DOWNGRADING SCHEDULE
16. DISTRIBUTION STATEMENT (of this Report) Approved for public release, distribution unlimited.		
17. DISTRIBUTION STATEMENT (of the abstract entered in Block 20, if different from Report)		
18. SUPPLEMENTARY NOTES		
19. KEY WORDS (Continue on reverse side if necessary and identify by block number) Bow-thrusters                      Vortices Thrusters                            Plumes Jets		
20. ABSTRACT (Continue on reverse side if necessary and identify by block number) An analytical model of a jet injected normally from a flat plate into a uniform crossing flow was modified to provide an improved method of predicting the interference effects arising from the complex flow fields induced by ship bow-thrusters. This model is an extension of previous work based upon a description of the jet as a series of distributed vortices. The analysis takes into account the position of the effective source of the		





Block 20 Continued:

jet and the blockage due to presence of the jet in the crossflow. Improvement in the predicted pressure distribution on the plate was obtained by adopting a new formula for determining the effective jet source which more closely approximates the experimental results. Further improvement resulted from the incorporation of a symmetric foil shape to simulate the presence of the jet and its highly turbulent wake. The accuracy of the model was evaluated for representative jet-to-crossflow velocity ratios. Good agreement with experimental results was achieved for large portions of the interaction field with particular improvement in the near-field and downstream regions.



Approved for public release; distribution unlimited.

Theoretical Modeling of Fluid Interactions  
Produced by Ship Bow Thrusters

by

Thomas Charles Cooper  
Lieutenant Commander, United States Navy  
B.S.M.E., Ohio State University, 1970

Submitted in partial fulfillment of the  
requirements for the degree of

MASTER OF SCIENCE IN MECHANICAL ENGINEERING

from the

NAVAL POSTGRADUATE SCHOOL  
March, 1982



## ABSTRACT

An analytical model of a jet injected normally from a flat plate into a uniform crossing flow was modified to provide an improved method of predicting the interference effects arising from the complex flow fields induced by ship bow-thrusters. This model is an extension of previous work based upon a description of the jet as a series of distributed vortices. The analysis takes into account the position of the effective source of the jet and the blockage due to the presence of the jet in the crossflow. Improvement in the predicted pressure distribution on the plate was obtained by adopting a new formula for determining the effective jet source which more closely approximates the experimental results. Further improvement resulted from the incorporation of a symmetric foil shape to simulate the presence of the jet and its highly turbulent wake. The accuracy of the model was evaluated for representative jet-to-crossflow velocity ratios. Good agreement with experimental results was achieved for large portions of the interaction field with particular improvement in the near-field and downstream regions.



## TABLE OF CONTENTS

I.	INTRODUCTION -----	9
II.	BACKGROUND -----	16
III.	IMPROVEMENT IN THE EXISTING MODEL -----	22
IV.	CONCLUSIONS -----	30
V.	RECOMMENDATIONS FOR FURTHER STUDY -----	32
	APPENDIX A - DERIVATION OF THE JOUKOWSKY TRANSFORMATION -----	53
	APPENDIX B - COMPUTER PROGRAM -----	56
	APPENDIX C - COMPARISON OF PRESENT MODEL WITH EXPERIMENTAL RESULTS -----	61
	LIST OF REFERENCES -----	113
	INITIAL DISTRIBUTION LIST -----	115





## LIST OF FIGURES

1. Hull low pressure areas at various speeds. -----	35
2. Hull suction effects vs R. -----	36
3. $-Y_s/Y_t$ vs. R for a "typical" hull. -----	37
4. Center of action of the suction force. -----	38
5. Comparison of experimental findings, VR=4. -----	39
6. Comparison of experimental findings. -----	40
7. Jet axis and conforming vortex loop system. -----	41
8. Comparison of pressure coefficient contours, experiment vs. source corrected conforming vortex model, VR=8. -----	42
9. Comparison of pressure coefficient contours, experiment vs. fully corrected conforming vortex model, VR=8. -----	43
10. Comparison of pressure coefficient contours, experiment vs. fully corrected conforming vortex model, VR=4. -----	44
11. Fully corrected conforming vortex model with the effective source $Z_e = 0.6 \sqrt{VR}$ vs. experiment, VR=8. -----	45
12. Plots of coefficients of pressure along the freestream axis used to determine the length of the foil. Data from [5]. -----	46
13. The Joukowski transformation. -----	47
14. Comparison of pressure coefficient contours, experiment vs. present analytical model, VR=4. -----	48
15. Comparison of pressure coefficient contours, experiment vs. present analytical model, VR=8. -----	49
16. Comparison of pressure coefficient contours, experiment vs. present analytical model, VR=10. -----	50



17. Conforming vortex model with a half cylinder for blockage correction vs. experiment, VR=8. -----	51
18. Comparison of theoretical values of $-Y_s/Y_t$ with experimental findings. -----	52



## ACKNOWLEDGEMENT

The author wishes to extend his appreciation to Professor Robert H. Nunn for his advice, guidance, and patience during the development of this analysis. Without his valuable assistance, it would not have been completed.



## I. INTRODUCTION

Since man first set sail, ships and boats have been steered by stern-mounted rudders or rudder-like devices. The bow has been left relatively uncontrolled. As the size of ships increased, they became more difficult to maneuver in close quarters, as when entering port. Tug boats were often required to provide lateral thrust at both ends of the ship. This was a satisfactory solution to the problem for many years. It did not provide the degree of independence desired by ship operators, however, and other methods were considered. Although experimental lateral thrust units were used in the mid-nineteenth century, the first practical unit was not installed until 1955. This unit, a through-tunnel type bow thruster installed in the "Princess of Vancouver" proved highly successful [1]. Since then, bow thrusters have steadily gained in popularity. The advantages of these units include providing a greater degree of maneuverability, increased safety, increased ability to operate in rough weather at oil rigs and research sites, and reduced tug charges.

In the past twenty-five years, ports have become increasingly crowded, labor and fuel costs have greatly increased tug boat charges, and ships have been built that are much larger and less maneuverable. Thus lateral thrust units





have not only become economical, but they are standard equipment for many new-construction ships.

As more bow thrusters came into use, it became apparent that although they work well at zero or very low forward speed, their effectiveness drops considerably as the ship's speed is increased [2]. In view of the large number of these units currently installed, there is suprisingly little information available concerning thruster/hull interactions.

Soon after the first unit was installed in 1955, it was learned that the operation of a tunnel-type thrust unit causes a low pressure area to form on the ship's hull [2] (see Fig. 1). To find the net resultant thrust, this suction force must be integrated over the effected area and subtracted from the thrust of the unit. When a thrust unit is operated, water surrounding the jet is entrained, as in an eductor, causing a low pressure area to be formed on the ship's hull in a small area about the jet. In addition, if a ship is moving forward, a plume is developed aft of the thrust unit and a system of vortices is formed. These vortices induce a velocity in the water at the ship's hull, causing a pressure drop. Additionally, the jet itself acts as an obstruction to the flow of water past the ship, causing the flow to change speed as it passes, thus causing another pressure variation. These induced velocity and blockage effects are so severe that a thrust unit's



effectiveness can drop as much as fifty percent with a speed increase of only three knots [1].

The effects of bow thruster jet/hull interactions upon a ship motion can be better understood by considering the equations of motion for a ship moving in a horizontal plane. The general forms of the equations are [3]:

$$m(\dot{u} - v\dot{\psi}) = X \quad \text{Surge equation}$$

$$m(\dot{v} + u\dot{\psi}) = Y \quad \text{Sway equation}$$

$$I_z \ddot{\psi} = N \quad \text{Yaw equation}$$

The linearized forms of these equations are sufficient for this analysis and, making the ship's center of gravity the coordinate system reference point, they become respectively:

$$-X_u(u - u_0) + (m - x_{\dot{u}})\dot{u} = X \quad (1)$$

$$-Y_v v + (m - Y_{\dot{v}})\dot{v} - (Y_r - mu_{\dot{v}})r - Y_{\dot{r}}\dot{r} = Y \quad (2)$$

$$-N_v v - N_{\dot{v}}\dot{v} - N_r r + (I_z - N_{\dot{r}})\dot{r} = N \quad (3)$$

where:

$m$  = mass of the ship

$u$  = velocity in the x-direction (initial value  $u_0$ )

$v$  = velocity in the y-direction

$\psi$  = yaw angle

$r$  = angular velocity =  $\dot{\psi}$

$I$  = mass moment of inertia



X = excitation forces in the x-direction

Y = excitation forces in the y-direction

N = excitation torque

Dots indicate differentiation with respect to time.

The subscripts u,  $\dot{u}$ , v,  $\dot{v}$ , r,  $\dot{r}$ , denote differentiation with respect to the subscript variable.

The left sides of these equations contain the velocity and acceleration-dependent terms such as added mass, added inertia, and hydrodynamic drag. The right sides implicitly represent the total forces in the x and y directions and the total moment about a vertical axis through the center of gravity. Although these terms are used to represent various excitation forces acting on a ship due to rudders, stabilizers, propellers, etc., this analysis will deal solely with the forces and moments caused by a through-tunnel bow-mounted thrust unit.

In the y-direction, the force due to a bow thruster may be written as:

$$Y = Y_t + Y_s$$

where:

$$Y_t = -\dot{m}_j u_j, \text{ the ideal jet thrust}$$

$$Y_s = \text{the induced "suction" force on the hull}$$

$$\dot{m}_j = \text{the mass flow rate of the jet}$$

$$u_j = \text{the jet velocity (positive to starboard).}$$



Inspection of Fig. 2 reveals that  $-Y_s/Y_t$  is nearly linear in the  $|u_\infty/u_j|$  ratio range of .1 to .3. Using this velocity ratio range as an example, an approximation of the right side of equations (2) and (3) can be made. This portion of the curves is of interest because the largest decrease in thruster performance takes place here. Since the slope and intercept of this line are dependent on hull shape, an average performance curve has been plotted in Fig. 3 to represent a "typical" hull. A straight line having a slope of 5.3 and an intercept of -0.65 is used to approximate the curve in the  $|u_\infty/u_j|$  ratio (hereafter R) of .1 to .3.

Thus:

$$-Y_s/Y_t = 5.3R - .65$$

Then since

$$Y_t = -\dot{m}_j u_j$$

$$Y_s = \dot{m}_j u_j (5.3R - .65) \quad (4)$$

and

$$Y = -\dot{m}_j u_j (1.65 - 5.3R) \quad .1 \leq R \leq .3 \quad (5)$$

By substituting this equation into equation (2), the motion in the y-direction is explicitly coupled to the motion in the x-direction through the dependency upon R.

The total turning moment N is the moment produced by the force Y acting at a distance  $x_c$  from the center of gravity.





This characteristic moment arm varies non-linearly as the ship's speed changes and is given as:

$$x_c = \frac{x_t Y_t + x_s Y_s}{Y}$$

where:

$x_t$  = the distance from the center of gravity  
to the thrust unit

$x_s$  = the distance from the center of gravity  
to the center of action of the hull  
suction force.

Chislett and Bjorheden [2] found that  $x_s$  varies linearly with ship's speed. The curve in Fig. 4, which is adapted from their data, has a slope of  $-.7$  and an intercept of  $1.0$ . Therefore:

$$x_s = x_t(1 - .7R) \quad R \leq 1.2 \quad (6)$$

When equations (4) and (5) are substituted for  $Y_s$ ,  $Y_t$  and  $Y$ , the location of the center of action of the combined force system is given by:

$$x_c = \frac{(3.71R^2 - 5.76R + 1.65)}{(1.65 - 5.3R)} x_t \quad .1 \leq R \leq .3 \quad (7)$$

and

$$N = Yx_c$$



Thus the yaw equation is coupled to the sway and surge equations. Note that equation (7) is only valid for velocity ratios between .1 and .3 for this particular fictitious hull.

Although this analysis has been greatly simplified, it demonstrates the complication of the relationships between turning moments and ship's speed when a lateral thrust unit is used. It can be seen from Fig. 2 that model tests of each ship type are necessary in order to accurately predict the performance characteristics of a lateral thrust unit. With a thorough understanding of the fluid mechanics of bow thruster systems, thrust units could be designed to reduce the hull suction effect and thus make them more usable under a wider range of conditions. An accurate analytical method for predicting jet/hull interactions would be useful in supplying this information without lengthy and costly model tests. Unfortunately, an accurate model that can be superposed with other effects is not available. It is the purpose of this thesis to propose an analytical method for predicting the jet/hull interactions of a through-tunnel type lateral thrust unit.



## II. BACKGROUND

As demonstrated in the preceeding section, the ship's hull/thruster interactions, when a ship has way on, can seriously degrade a bow-thruster's effectiveness. In order for naval architects to design a bow thruster installation so that it can be used effectively when the ship is moving, a complete knowledge of these effects is required. Unfortunately, only a few waterborne tests have been performed. These experiments (Fig. 2), while clearly demonstrating the overall effects on turning ability, do not provide information on the actual pressure distribution on the hull. For an incompressible flow, the jet path and the induced flow are dependent mainly on the momentum flux ratio  $\rho_j U_j^2 / \rho_\infty U_\infty^2$  and are relatively independent of the Reynolds number [4]. Thus an air jet injected into a crossing air flow will induce a reaction similar to that of the water jet of a thrust unit at the same velocity ratio. There have been a number of studies of air jets emitted from a flat plate into a crossing air flow in connection with the design of VSTOL (Vertical and Short Take Off and Landing) aircraft. Notable studies have been made by Bradbury and Woods [4] and Fearn and Weston [5].

While the results of these experimental studies are useful to the naval architect when making an initial design intended to improve thruster efficiency, they provide no



method for evaluating the resultant configuration. Lengthy and expensive model or shipboard tests are required for this purpose. An accurate and versatile analytical model of the flow interaction effects would provide a quick and inexpensive means of evaluating new designs, thereby reducing the required number of model tests. Some empirical and semi-empirical models have been developed. While they can predict the pressure distributions on a plate, they cannot be easily superposed with other effects such as a secondary jet. Because a fluid jet injected into a crossing stream is a turbulent, three dimensional, highly non-linear problem, empiricism to some degree has been used in all models to date. In this study an effort has been made to eliminate or at least reduce the empirical inputs to existing analytical models while improving their accuracy.

A review of available models revealed that Wooler's formulation [6] minimized empiricism, requiring only an experimentally determined jet trajectory. Hence his model, as modified by Waterman [7], was selected as a basis for further investigation.

In order to visualize the interaction field and determine the accuracy of an improved model, once formulated, accurate experimental results were required. A review of available studies revealed that the pressure contours\* for a given

---

\* In this thesis, values of local pressures,  $P$ , are expressed in the form of pressure coefficients,  $C_p$ , where:

$$C_p = \frac{P - P_\infty}{\frac{1}{2} \rho U_\infty^2}$$





velocity ratio vary considerably from one report to the next, as illustrated in Fig. 5 and 6. This difference is especially noticeable in the downstream region for values of  $|U_j/U_\infty|$  (hereafter VR) of about 4, and is present to some degree at all velocity ratios. Figure 5 seems to imply that the induced flow may not be solely a function of velocity ratio since the different studies were not made at the same freestream velocities. However, considering studies made with the cross-flow velocity nearly equal, as in Fig. 6, it is seen that the discrepancies are more probably due to variations in the equipment and test procedures used. This serves to point out the uncertainty of the available experimental results. The results of Fearn and Weston [5] agree well with those of other researchers over a broad range of velocity ratios. Additionally their report was the most complete of those reviewed. It contains not only the usual plots of pressure contours, but also raw data, time variation of pressure information, and a comparison with other reports. For these reasons, the results reported in [5] were selected as the basis for determining the accuracy of the analytical model.

Before attempting to develop an improved model, a thorough review of Wooller's and Waterman's work was made in order to understand their approaches and verify their results. A rederivation of these basic formulations will not be presented here as it can be found in references [6] and [7]. It was noted that Waterman's adoption of a conforming vortex



model was a considerable improvement to Wooler's formulation. In the conforming vortex model the vortices are constrained to lie within the jet rather than being tangential to the jet axis as in Wooler's model. By making this alteration, the horseshoe vortices are made to conform to the curvature of the jet described by the empirical trajectory equation (see Fig. 7):

$$\frac{x}{d} = B[\cosh(Z/Bd) - 1] \quad (8)$$

Where:

x = the distance down-stream from the jet center.

d = the jet diameter.

z = height of the jet axis above the plate.

B = trajectory parameter =  $.19(VR)^2$ .

The interference velocity at an arbitrary point on the plate is determined by applying the Biot-Savart Law. The trailing vortices are approximated as straight line segments. As these segments become small, the linear approximation can be made to conform to the curvature of the jet. The total interference component at a particular point due to the entire jet results from the summation of all the elemental contributions.

A comparison of the results of both formulations reveals that Wooler's work more closely agrees with the experimental findings of Bradbury and Woods [4] than does Waterman's,



even though the trailing vortices in Wooler's model do not follow the jet trajectory as in the actual case. This result is, in part, due to the fact that in Wooler's formulation the perturbation velocity at a particular point on the plate is caused by vortices acting at different distances from the plate. In Waterman's model the interference velocities result from the trailing horseshoe vortex contributions acting at a single radius. Thus the interference velocities predicted by Waterman's conforming vortex model are generally higher and hence produce lower coefficients of pressure than those of Wooler. In addition to modifying Wooler's model, and noting studies by Keffer and Baines [8] and Schmidt [9], Waterman introduced the concept of an effective origin of the vortex sheet at a distance,  $z_e$ , above the plate given by the formula:

$$z_e = \frac{VR \sqrt{VR}}{15} \quad (9)$$

Applying this expression to the conforming vortex model, Waterman produced the same, if not better far-field agreement (Fig. 8). However, the model lacked accuracy in the near-field.

Waterman further noted that the discrepancies observed in the upstream region can be at least partially attributed to the blockage of the freestream flow by the jet. It was noted that the downstream area is dominated by separation, vortex



shedding, and turbulent entrainment. Waterman interpreted the blockage effect as that of a circular cylinder in an irrotational flow. Using potential flow theory to predict the velocity perturbations in the uniform flow caused by a doublet centered at the jet origin, Waterman, after some numerical experimentation, arrived at an estimate for an effective jet diameter given by  $.96 \sqrt{VR}$ . The results of this model (Fig. 9) are significantly better than Wooler's model in the upstream region and far field. This improvement was accomplished at the expense of introducing two additional empirical relationships, the position of the effective source and the effective jet diameter.





### III. IMPROVEMENT IN THE EXISTING MODEL

Evaluation of Waterman's "fully-corrected conforming vortex model" (Figs. 9 and 10) revealed that the correlation of the analytical model with the experimental data in the area just forward of the jet is adequate at each of the velocity ratios reported. However, his model is accurate in the far-field only for the velocity ratio of 8.0 and in the near-field to the sides of the jet for a velocity ratio of 4.0. The correlation is poor in the area aft of the jet for all velocity ratios. It was apparent that the near and mid-field regions, especially aft of the jet, required the greatest attention.

In order to gain a better understanding of the effects of the empirical inputs to Waterman's model, it was run a number of times using various values of the constants in the trajectory, effective source, and effective diameter equations. It was learned that small changes in the trajectory parameter,  $B$  in equation (8), cause little change in the overall pressure distribution. The correlation with experimental data was improved at some velocity ratios while it diverged at others for a particular value of  $B$ . A value of  $B = .19(VR)^2$ , as before, resulted in the best overall correlation of the pressure distribution on the plate. Changing the effective diameter of the jet causes



major changes in the near-field pressure distribution, but has little effect in the far-field. This was expected considering the short range of the disturbance caused by a doublet in a uniform flow using inviscid relationships. The model proved to be particularly sensitive in both the near and far-field regions to changes in the position of the effective source. Since the quality of the model depends so greatly on the effective source correction, the equation for it was investigated more closely.

Equation (9), the empirical formula for the effective source height, was formulated by Schmidt [9] who refers to Jordinson [10] and Keffer and Baines [8] for the experimental data used as a basis for his work. The Jordinson paper could not be obtained for review. The data presented by Keffer and Baines, however, does not fit the equation presented by Schmidt. The equation,  $z_e/d = .8\sqrt{VR}$  fits the Keffer and Baines data much better as seen in Table I.

TABLE I  
COMPARISON OF VALUES OF  $z_e/d$

VR	Schmidt	Experimental Keffer & Baines	$.8\sqrt{VR}$
4	.53	1.59	1.60
6	.97	1.95	1.93
8	1.51	2.30	2.26



However,  $Z_e/d$  can vary from  $.54 \sqrt{VR}$  to  $.8 \sqrt{VR}$  and still be in the range of the heights given in Table I. Using an effective source location of  $Z_e/d = .8 \sqrt{VR}$  in the Waterman model significantly improves the correlation. But, if  $Z_e/d = .6 \sqrt{VR}$  is used, the correlation is much better even without the effective diameter correction. Thus, by establishing the effective source at  $.6 \sqrt{VR}$  diameters above the plate, the full jet diameter can be used in the model and the diameter correction is eliminated. See Fig. 11 for an example of the improved correlation resulting from this change.

Concentrating on the area aft of the jet, it can be seen by comparing Fig. 8 with Fig. 10 that this area is primarily affected by the blockage near the plate due to the jet. In making multiple runs of Waterman's model and varying the parameters of the vortices within the plume, it was confirmed that they have little effect on the near-field pressures. The far-field to either side of the jet is dominated by the vortices within the plume. Therefore, to improve the model's accuracy in the near-field, the analysis centered on the jet blockage effect. Wu and Wright [11] proposed that a fictitious afterbody exists downstream of the jet. This afterbody encompasses the highly turbulent, three-dimensional flow caused by vortex shedding and entrainment of fluid within and downstream of the jet. Outside of this area, the fluid streamlines are fairly smooth and close to those of an inviscid flow. With this concept in mind, consideration was



given to using an elongated shape such as an ellipse or a symmetrical foil to approximate the blockage effect.

In order to establish a probable shape for the afterbody, the coefficients of pressure along the corssflow axis from the forward edge of the jet to seven diameters aft of the jet were plotted using the data of [5] (Fig. 12). These pressure contours resemble those in reference [12] and [13] for a symmetrical foil in a uniform flow. Thus a symmetrical foil was selected to approximate the jet and the afterbody near the plate.

To determine a length for the foil, it was assumed that the foil should end where the coefficient of pressure reaches an undisturbed (zero) value. It was not expected that the coefficient of pressure should necessarily rise above zero aft of the jet due to severe dissipation in the near-wake region and the interference effects of the vortices within the plume. Indeed the coefficient of pressure leveled-off at approximately -0.1 for all available data. Therefore, -0.1 was selected as a first approximation of the value of the coefficient of pressure used to determine the length of the foil. The corresponding distances from the jet center to the trailing edge were determined to be 6.2, 3.0, and 2.5 jet diameters for the velocity ratios of 3.9, 8.0, and 10.0, respectively.

For simplicity, a standard Joukowski foil was selected since it can be easily approximated through mapping methods.





Referring to Fig. 13, the Joukowski transformation,

$$Z = \zeta + \frac{\ell^2}{\zeta}$$

is used to transform the foil in the  $z$ -plane to a cylinder in the  $\zeta$ -plane so that the foil can be treated as a doublet in a uniform stream. The perturbation velocities due to the presence of the foil are then:

$$\frac{u}{U_\infty} = \mathcal{R} \left[ \left( \frac{\zeta}{\zeta'} \right)^2 \frac{(\zeta' + a)}{(\zeta + \ell)} \right] - 1$$

and

$$\frac{v}{U_\infty} = - \mathcal{I} \left[ \left( \frac{\zeta}{\zeta'} \right)^2 \frac{(\zeta' + a)}{(\zeta + \ell)} \right]$$

Where:

$u$  = the surface perturbation velocity in the direction of the cross-flow due to the presence of the jet and afterbody as modeled by the foil.

$v$  = the surface perturbation velocity perpendicular to the cross-flow due to the presence of the jet and afterbody as modeled by the foil.

$\ell$  =  $1/4$  the distance from the forward focus of the foil (corresponding to the point  $(-\ell, 0)$  in the  $\zeta$ -plane) to the trailing edge.

$a$  = the radius of the transformed circle. This term is a function of  $r$ , the distance from the forward focus of the foil to the leading edge.



Appendix A contains a complete derivation of the above transformation.

The thickness of the foil is a function of both  $r$  and  $\ell$ . As described above, the foil length is a function of the velocity ratio so that the length  $\ell$  is given by:

$$\frac{\ell}{d} = \frac{6}{VR} \quad (10)$$

Initially it was assumed that the forward focus of the foil should be at the center of the jet. This makes  $r$  equal to one-half the jet diameter. When substituted for the doublet in the fully corrected model, this method provided significant improvement in the downstream area. The upstream correlation was poor, however, since the foil was too thick and too blunt at the leading edge. It was necessary to adjust the value of  $r$  to provide a thinner and more streamlined body. Next a foil with its thickness equal to one jet diameter was tested. Using the formula, maximum thickness/ $d = 5.2(m/\ell - .7(m/\ell)^2)$  [13], where  $m$  is a function of  $r$ . It was found that if  $r/d = .12d/\ell$ , where  $\ell$  is given by equation (10), the thickness is nearly equal to the jet diameter for the entire range of velocity ratios. The foil is then moved forward so that its leading edge coincides with that of the jet. This configuration (App. B) produced the results shown in Figs. 14, 15, and 16 in comparison with experimental values [5] for velocity ratios of 4.0, 8.0, and



10.0 respectively. Radial and circumferential pressure distributions for velocity ratios of 3.9 and 8.0 are plotted against the experimental findings of Fearn and Weston [5] in Figs. C-1 through C-52.

Attempts were made to use other fictitious shapes such as ellipses and ovals as well as distributed source-sink combinations. The foil shape, however, produced the best results. So the simple relationships for the near-field blockage effect given above were retained in the final model.

Reviewing the results, it is seen that for a velocity ratio of 8.0, the correlation between this model and the experimental data is very close except in the area of highly turbulent flow immediately aft (within two diameters) of the jet. This is a region of uncertainty for all velocity ratios due to the three-dimensional flow caused by entrainment, vortex shedding, and other highly-viscous wake phenomena. Since this area is small, it contributes little to the overall thruster/hull interaction. For a velocity ratio of 3.9, the correlation is excellent except for the mid- and far-field regions aft of the jet centerline.

This was expected since it was determined earlier that the blockage effect of the jet has little effect in the far-field. It was observed that if  $r$  is such that it causes the foil to have a circular shape at the leading edge the correlation in the area forward of the jet is improved.



However, the agreement deteriorated in the areas to the sides and aft of the jet. By varying  $r/d$  as a function of the location of the point at which the velocity perturbations are being calculated, the shape of the foil can be altered so that it is nearly circular at the leading edge and becomes thin aft of the jet centerline. This configuration worked better, but it failed to significantly improve the overall pressure distribution resulting from  $r/d = .12d/l$ . This observation did lead to the idea of using a half-cylinder shape for the jet blockage. That is, the fluid forward of jet "sees" a cylinder but once past the jet centerline the influence of the cylinder is rapidly diminished. The results of this configuration are presented in Fig. 17 from which it can be seen that while this is a significant improvement over Waterman's model, it is not as accurate as the full foil-shape model. It is concluded that further improvement of the model must involve a more sophisticated treatment of the vortices within the plume as well as the blockage effect of the jet.





#### IV. CONCLUSIONS

As evidenced by Figs. 14, 15, 16, and C-1 through C-52 this analysis adequately predicts the pressure distribution on a flat plate from which a jet is emitted into a crossflow. Application of the model is limited, however, to velocity ratios  $VR = 3.9$  or greater. This is due to the method by which the length of the fictitious afterbody is determined. Above velocity ratios of about 4, this length decreases for increasing  $VR$ , but plots of the coefficients of pressure along the crossflow axis similar to Fig. 12 indicate that the afterbody length should decrease also for values of  $VR$  less than about 4. This is consistent with the observations of Fearn and Weston. They reported that an anomaly in the pressure distribution in the wake occurs at a velocity ratio of 3.9. The implication is that the rate of pressure recovery in the wake region is a minimum for a velocity ratio of about 3.9 [5].

No attempt has been made to accurately predict the pressure distribution in the highly turbulent wake of the jet. This area, having a width of about one jet diameter, extends downstream from the jet along the crossflow axis. The predicted values of the plate pressures reported here cannot be relied upon since most of this area is contained within the fictitious afterbody.



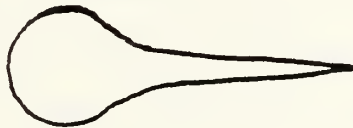
Figure 18 shows the results of this analysis plotted as the ratio of the induced side force to the jet thrust,  $-Y_s/Y_t$ , versus the velocity ratio VR. These results are compared with NPL pressure measurements on a flat plate and the model tests of English [1] and Chislett and Bjorheden [2]. The slope of the predicted  $-Y_s/Y_t$  curve is approximately 5.5, whereas that of the experimental data is about 5.3 for both the flat plate and the model tests. While this analysis predicts somewhat larger values for the overall (integrated) interference effects, the small difference between these slopes indicates that the nature of the relationship between the interference effects and the velocity ratio predicted by the analytical model is correct. Fearn and Weston did not report overall interference effects so the correlation between their work and the NPL experiments is not known. Since the assumptions concerning the shape and size of the afterbody were based on Fearn and Weston's data, the degree to which this analysis is in error cannot be determined from Fig. 18 alone. Even with these deficiencies, it is felt that this analytical model adequately predicts the pressure distribution on a flat plate and can be used as a first approximation for design purposes.



## V. RECOMMENDATIONS FOR FURTHER STUDY

In Chapter III it was noted that afterbody shapes other than a symmetric foil have been tried without significant improvement. This does not mean that this approach showed no promise for possible improvement in the model, but only that the actual shapes tested were not the best. It is felt that this model can be improved by changing the shape used for the jet and afterbody.

As reported earlier, the crossflow fluid particles near the plate apparently see a cylindrical shape when approaching the jet. As they pass the jet, some particles are entrained, some join the turbulent flow within the wake, and, further out, they pass as if the jet and wake together are a solid object. Just downstream of the jet, along the crossflow axis, there is an area of high entrainment. This causes a high local pressure drop out to about one jet diameter for  $VR = 8$ . Pressure recovery is rapid past this point. This leads to the idea of using a shape such as:



This shape has a cylindrical leading edge, the maximum thickness is just downstream of the jet center, and then it



narrows quickly to a relatively thin tail. The total length is the same as that for the symmetric foil.

It is expected that this shape can be formed using the Joukowski transform of the existing model by varying  $r$  as a function of the angular position of the particular point at which the perturbation velocities are being calculated. Although a functional relationship which will work over a range of velocity ratios has not yet been found, it is possible that one exists. This idea might also be pursued using panel (distributed singularity) methods.

Another area of uncertainty during the course of this study was the empirical jet trajectory equation. Reports of experiments to determine the jet axis provide a wide range of possible trajectories. If the trajectory equation used in this model is accepted as correct, the trajectory constant  $B = .19VR^2$  still may not be accurate over a wide range of velocity ratios. In particular, it is suspected that it may be in error for velocity ratios near 4 where an anomaly in the plate pressure distributions occurs. The cause of this anomaly is not clear, but it is suspected that this is the point where the jet momentum is so low compared to that of the crossflow that the jet reattaches to the plate within a few jet diameters. If so, the jet trajectory would be quite different than that which is currently modeled.

Finally, the entrainment of the crossflow fluid into the jet is implicitly accounted-for in the formulation of the





horseshoe vortices. However, the pressure drop associated with the jet entraining the surrounding fluid is not explicitly determined. This model predicts a zero pressure distribution at very high velocity ratios (zero ship speed). Further improvement of this model in accounting for entrainment is needed if it is to be used to predict the performance of bow-thrusters in ships with no way on.



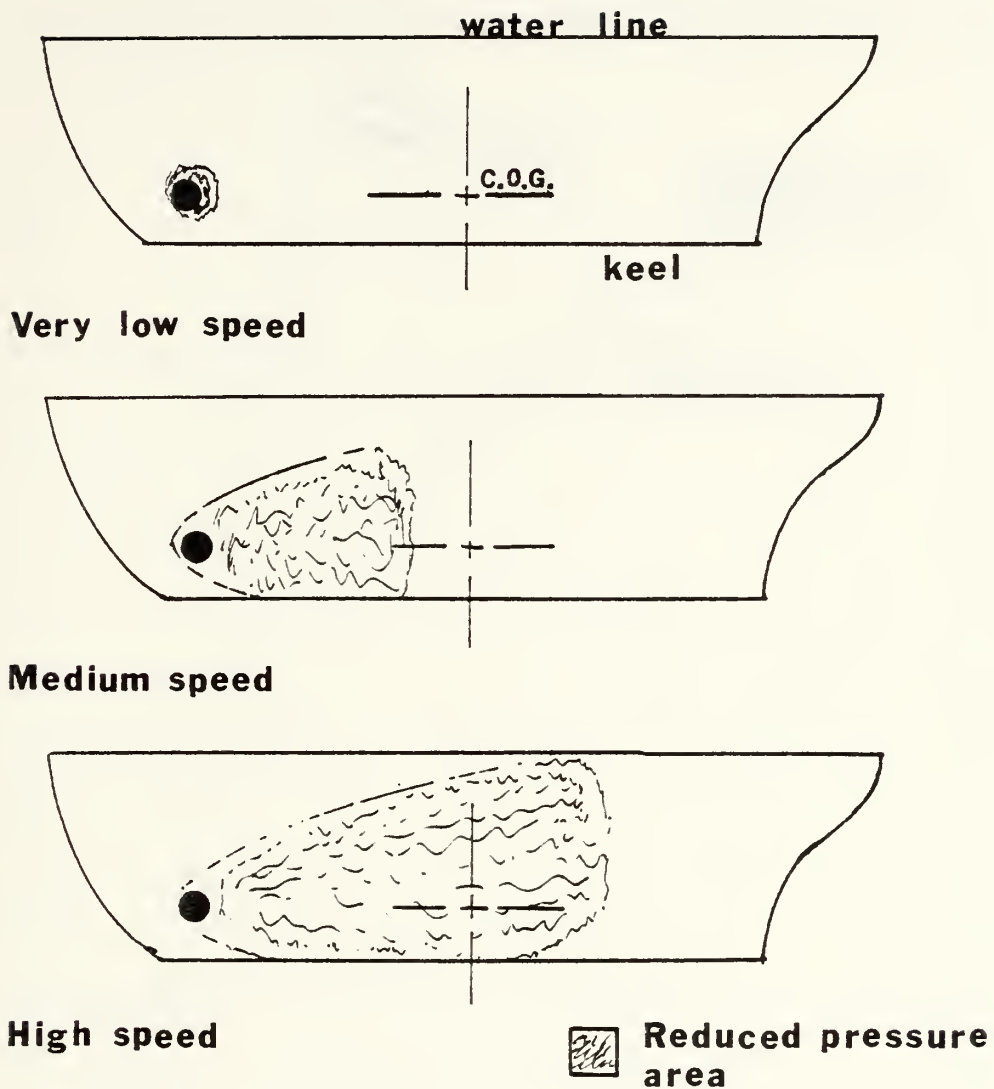


Figure 1. Hull low pressure areas at various speeds.



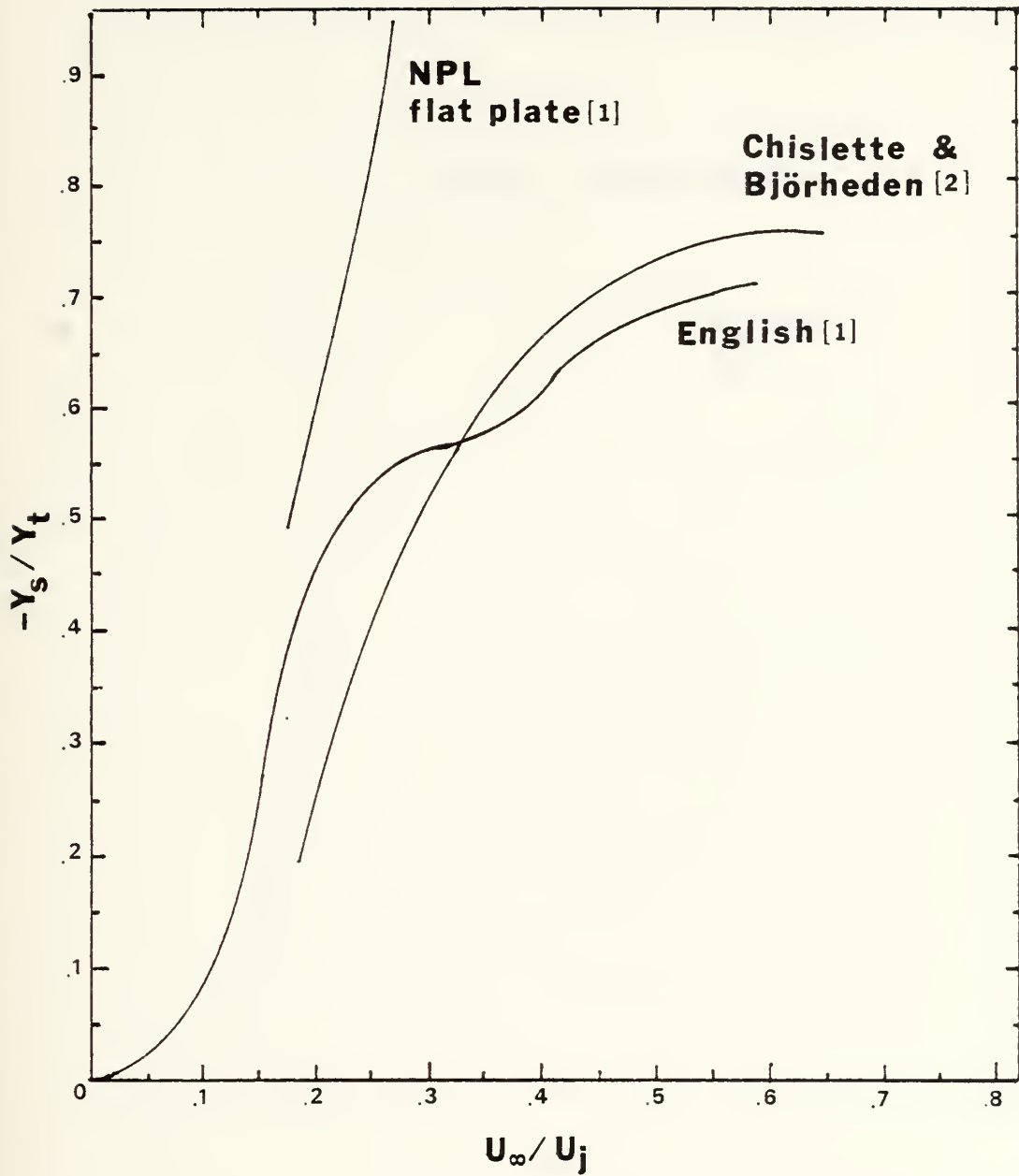


Figure 2. Hull suction effects vs. R.



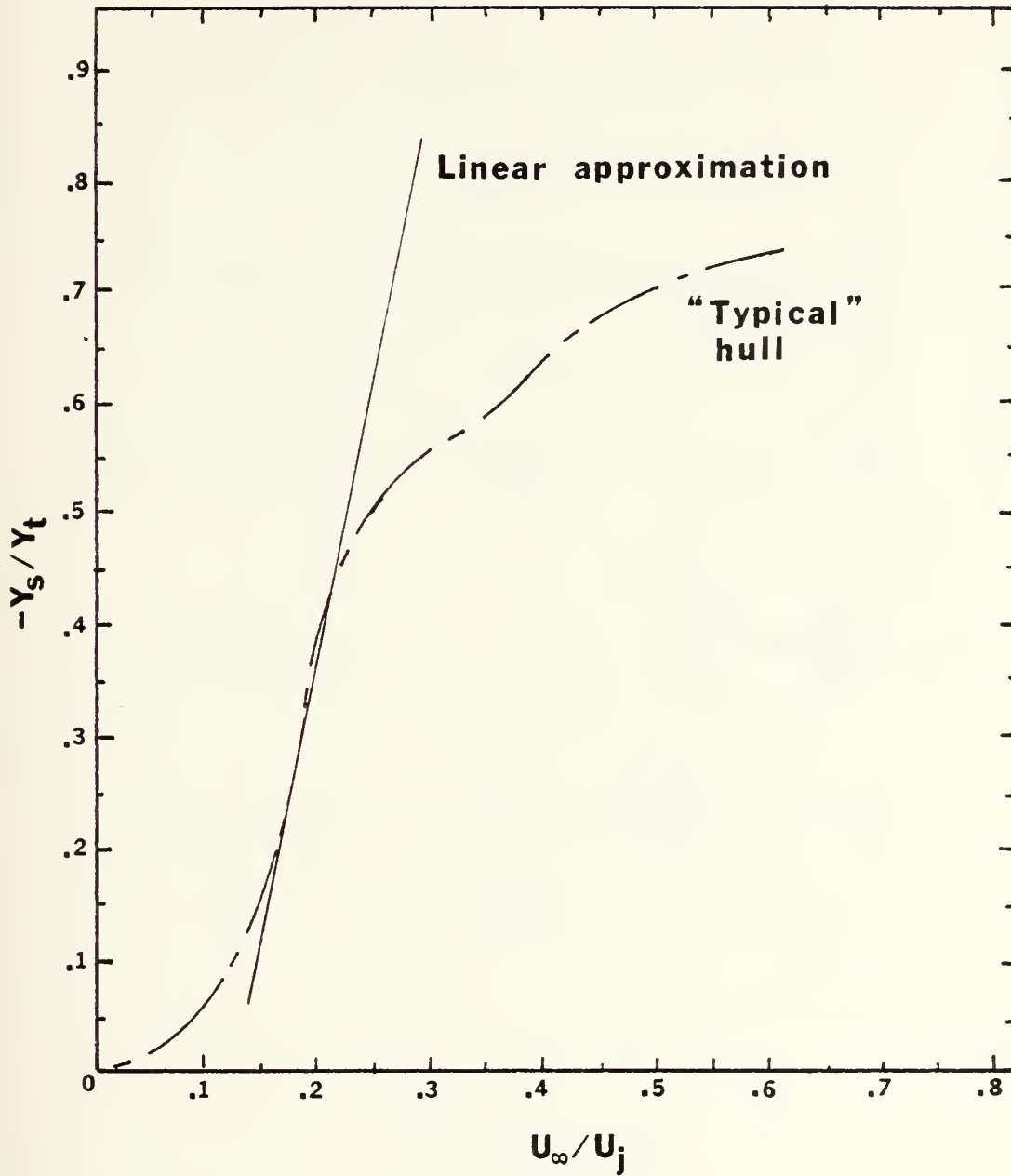


Figure 3.  $-Y_s/Y_t$  vs.  $R$  for a "typical" hull.





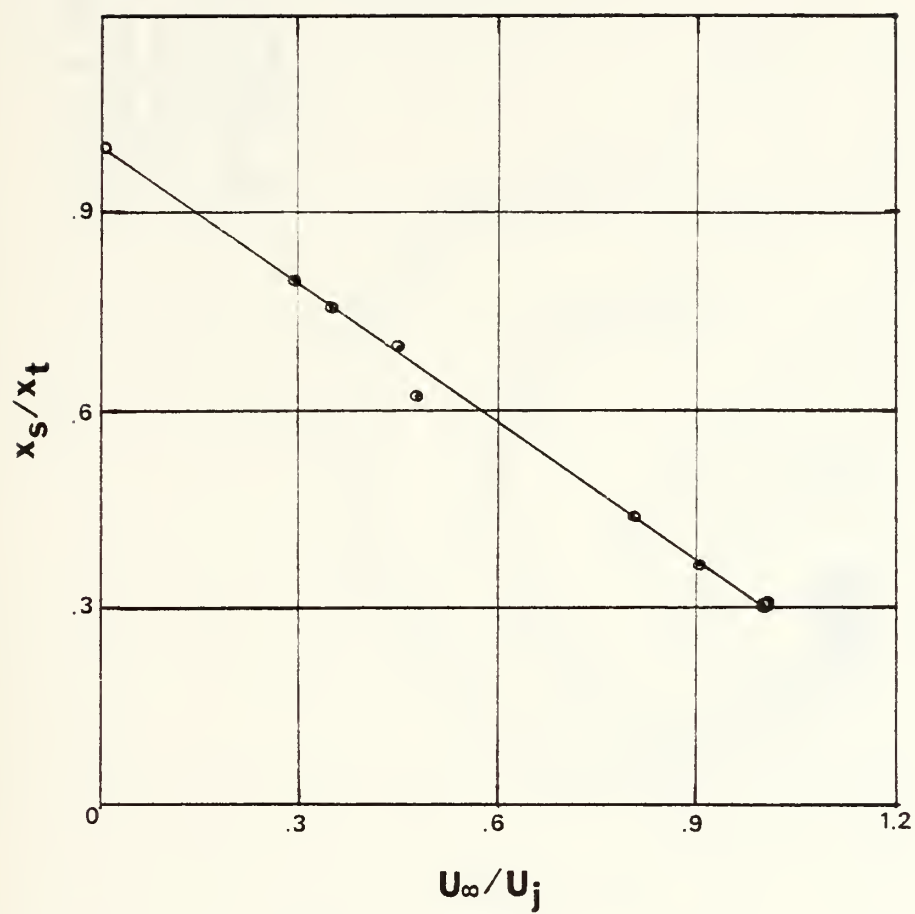


Figure 4. Center of action of the suction force. [2]



Fearn & Weston  
 $U_\infty : 67 \text{ m/s}$   
 Thompson  
 $U_\infty : 12 \text{ m/s}$   
 Bradbury & Wood  
 $U_\infty : 18 \text{ m/s}$

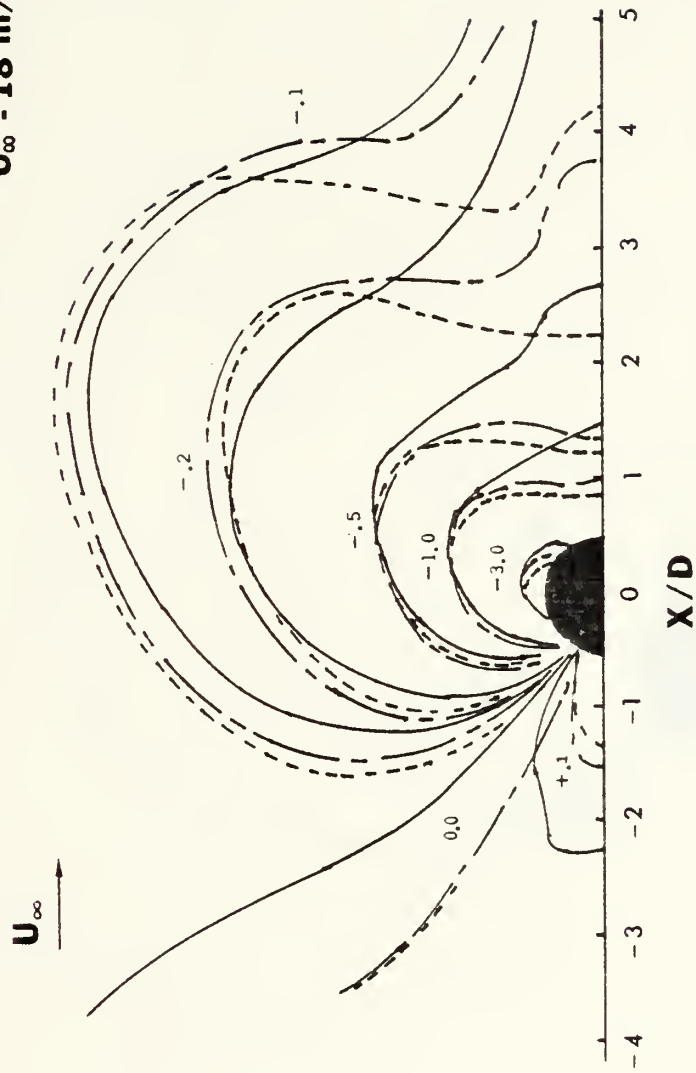


Figure 5. Comparison of experimental findings,  $VR=4$ . [5]



— Fearn & Weston  
 VR : 3.4  
 $U_{\infty}$  : 31.4 m/s  
 - - - Ousterhout  
 VR : 3.3  
 $U_{\infty}$  : 27.8

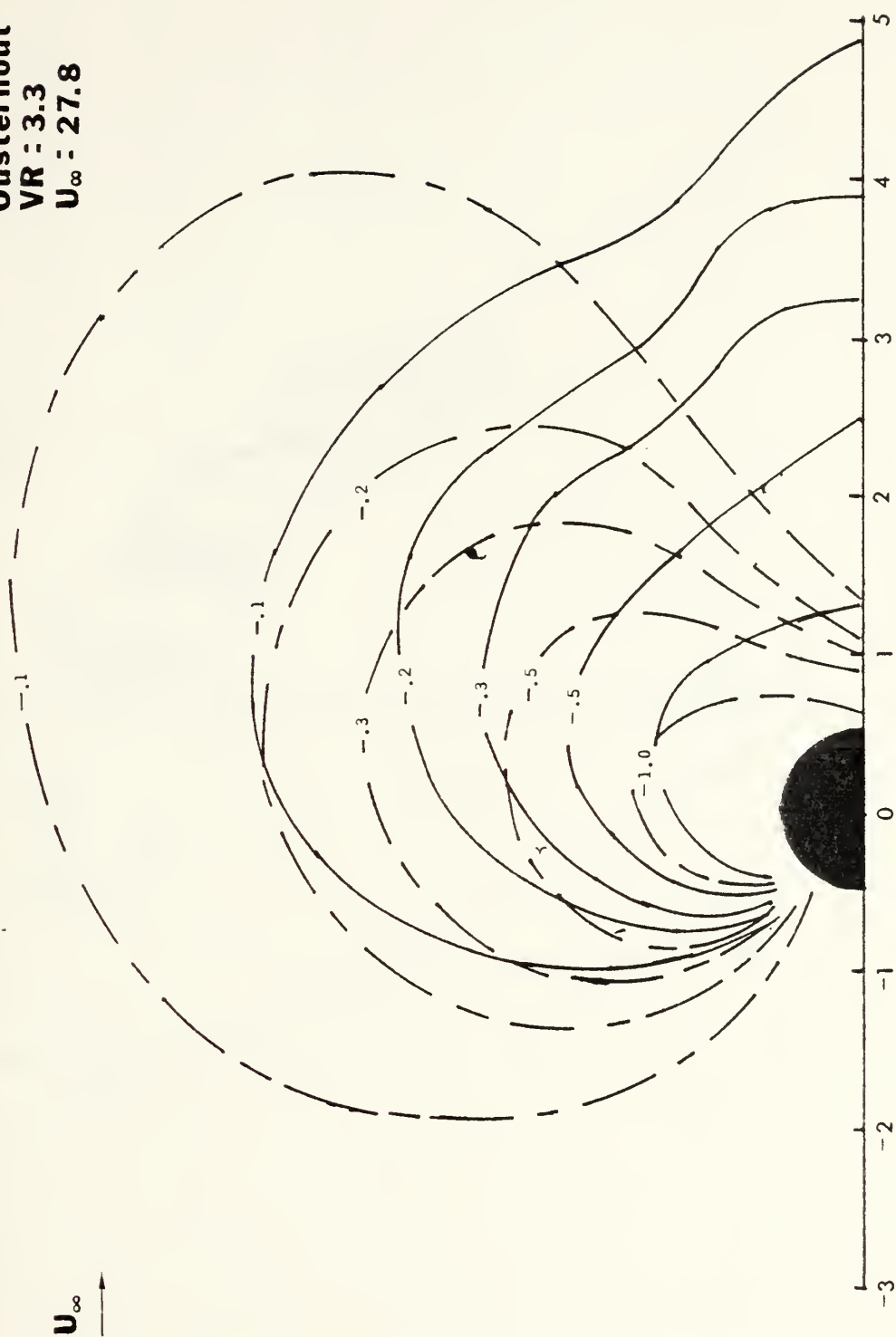


Figure 6. Comparison of experimental findings. [5]



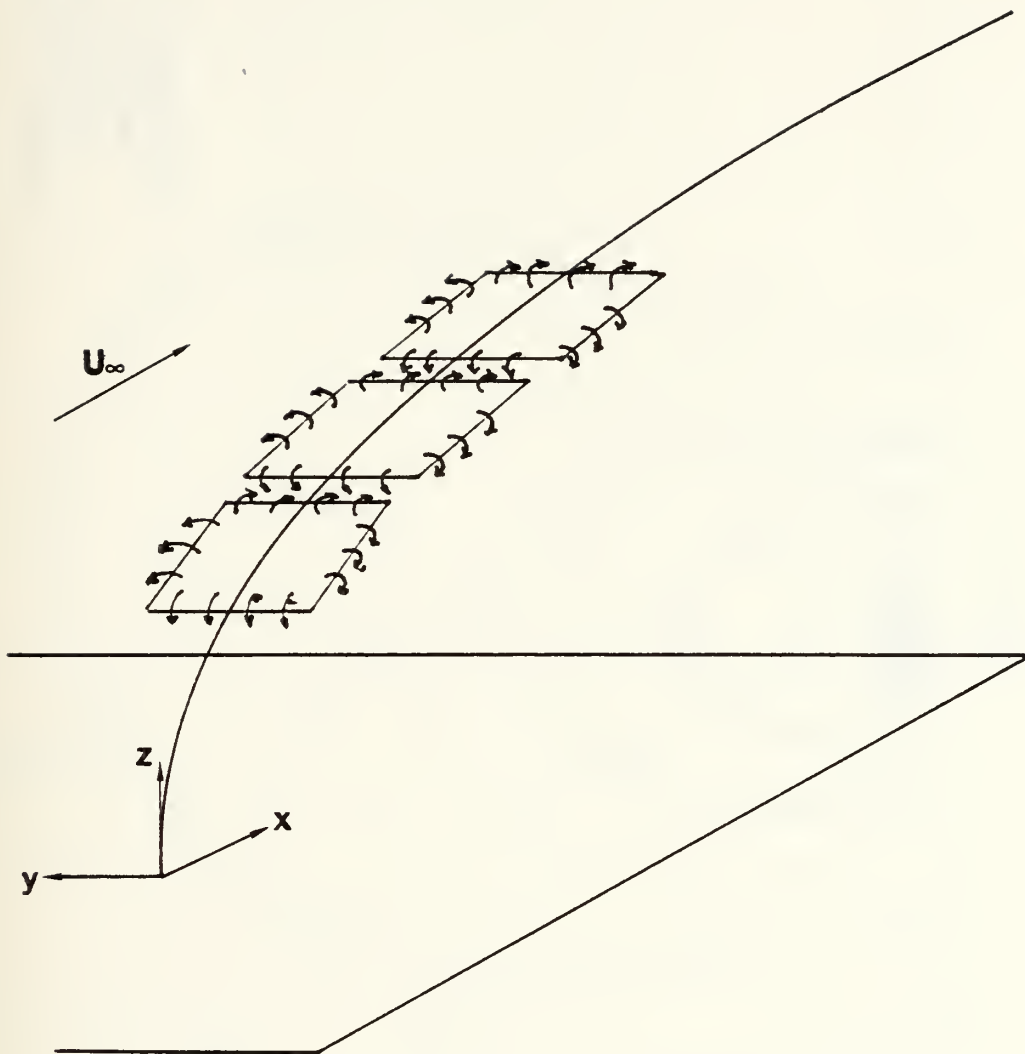


Figure 7. Jet axis and conforming vortex loop system. [7]





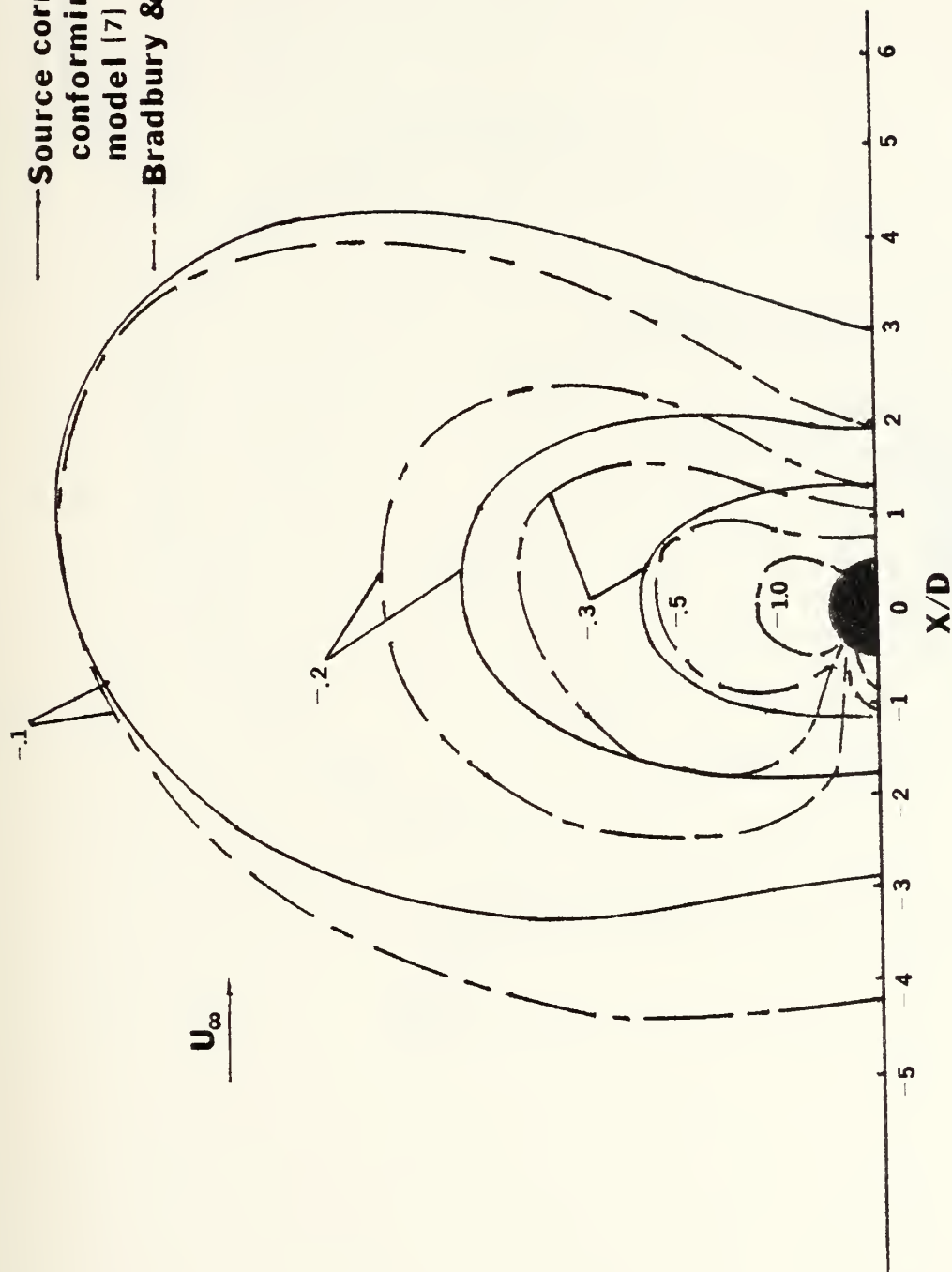


Figure 8. Comparison of pressure coefficient contours, experiment vs. source corrected conforming vortex model,  $VR=8$ .



— Fully corrected  
 conforming vortex  
 model [7]  
 - - - Bradbury & Wood [4]

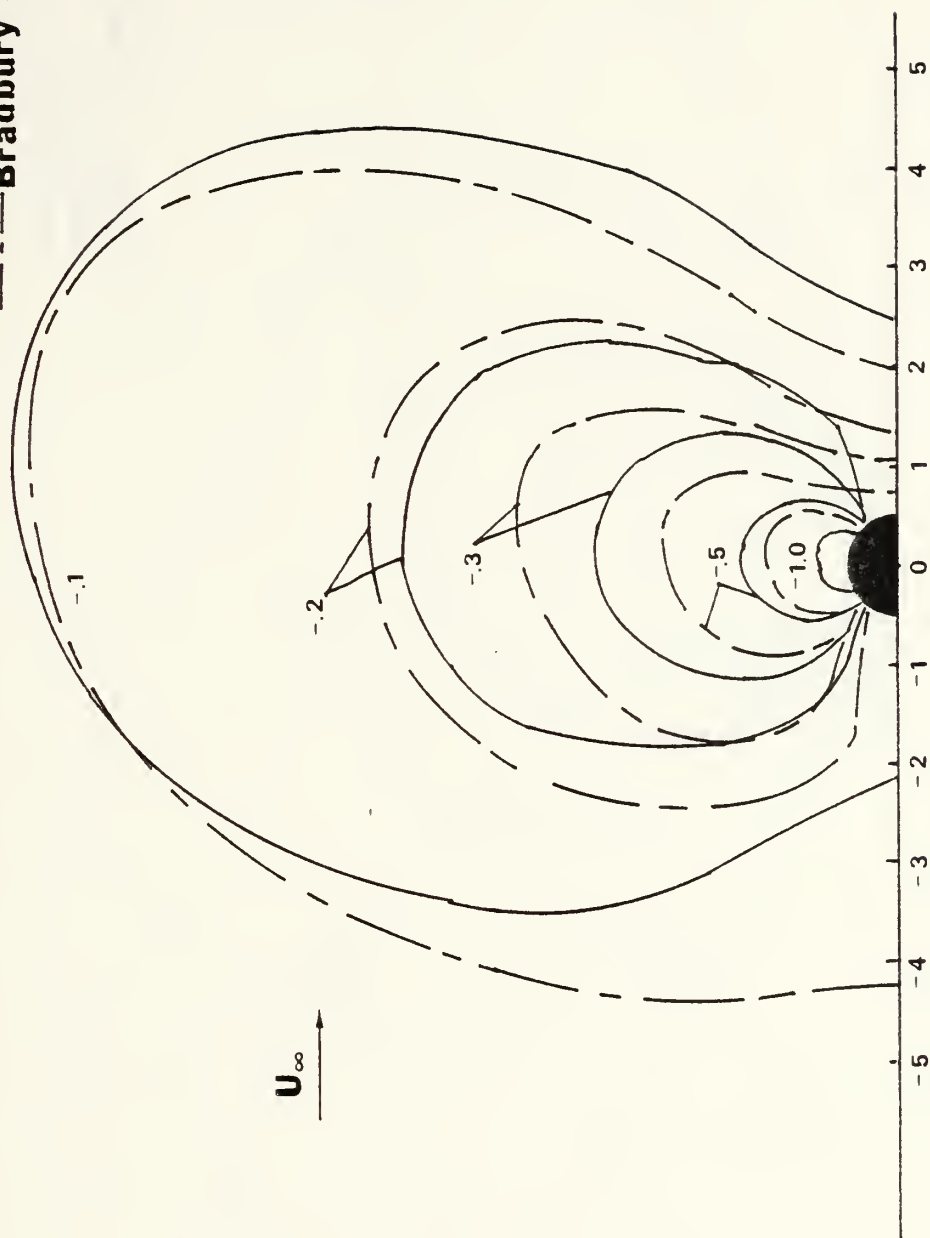


Figure 9. Comparison of pressure coefficient contours, experiment vs. fully corrected conforming vortex model,  $VR=8$ .



**Fully corrected  
conforming vortex  
model [7]  
Bradbury & Wood [4]**

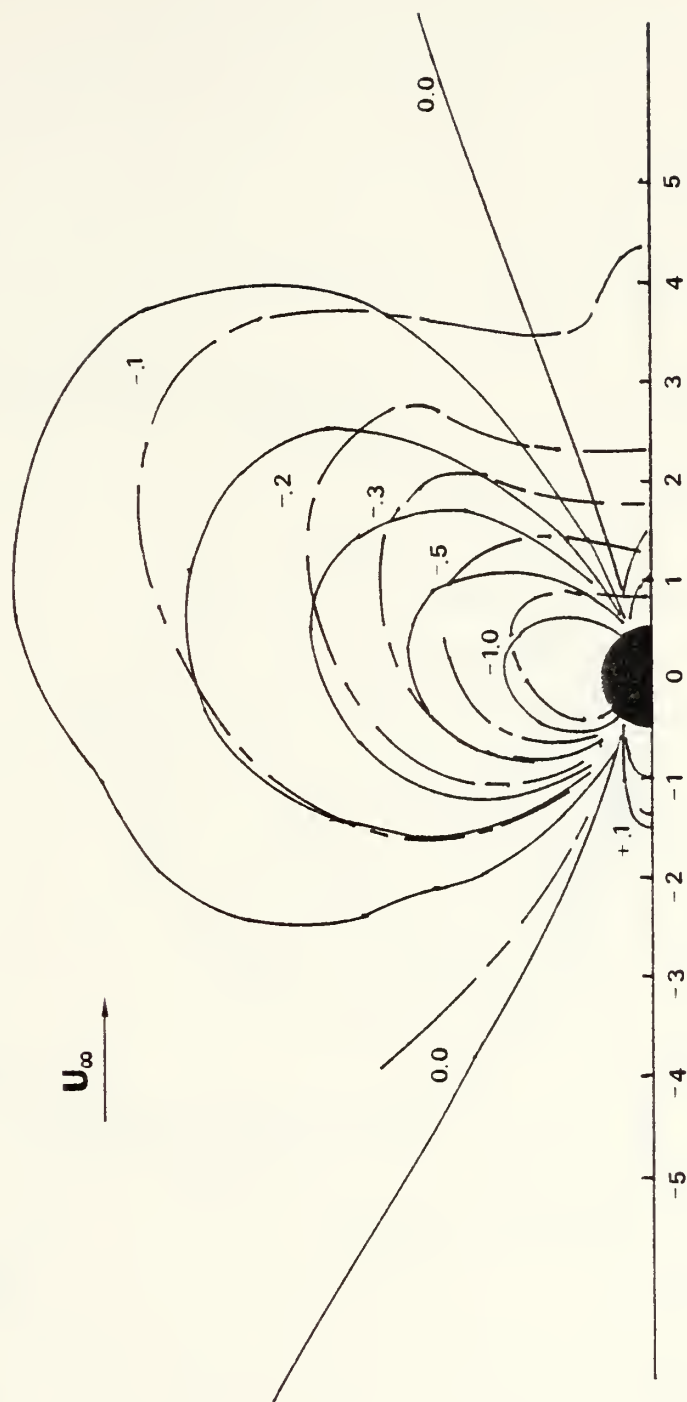


Figure 10. Comparison of pressure coefficient contours, experiment vs. fully corrected conforming vortex model,  $VR=4$ .



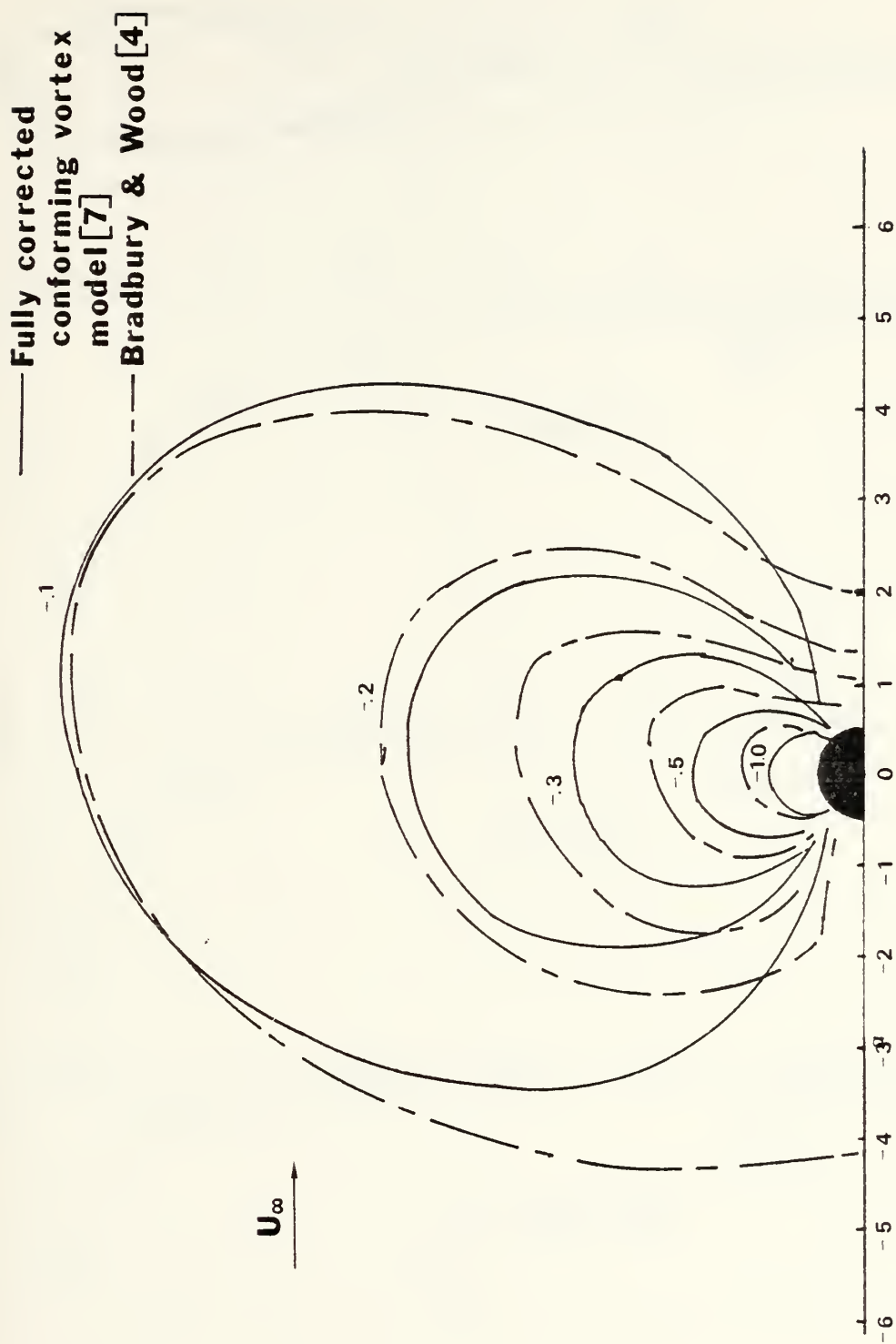


Figure 11. Fully corrected conforming vortex model with the effective source  $Z_e = .6 \sqrt{VR}$  vs. experiment,  $VR = 8$ .





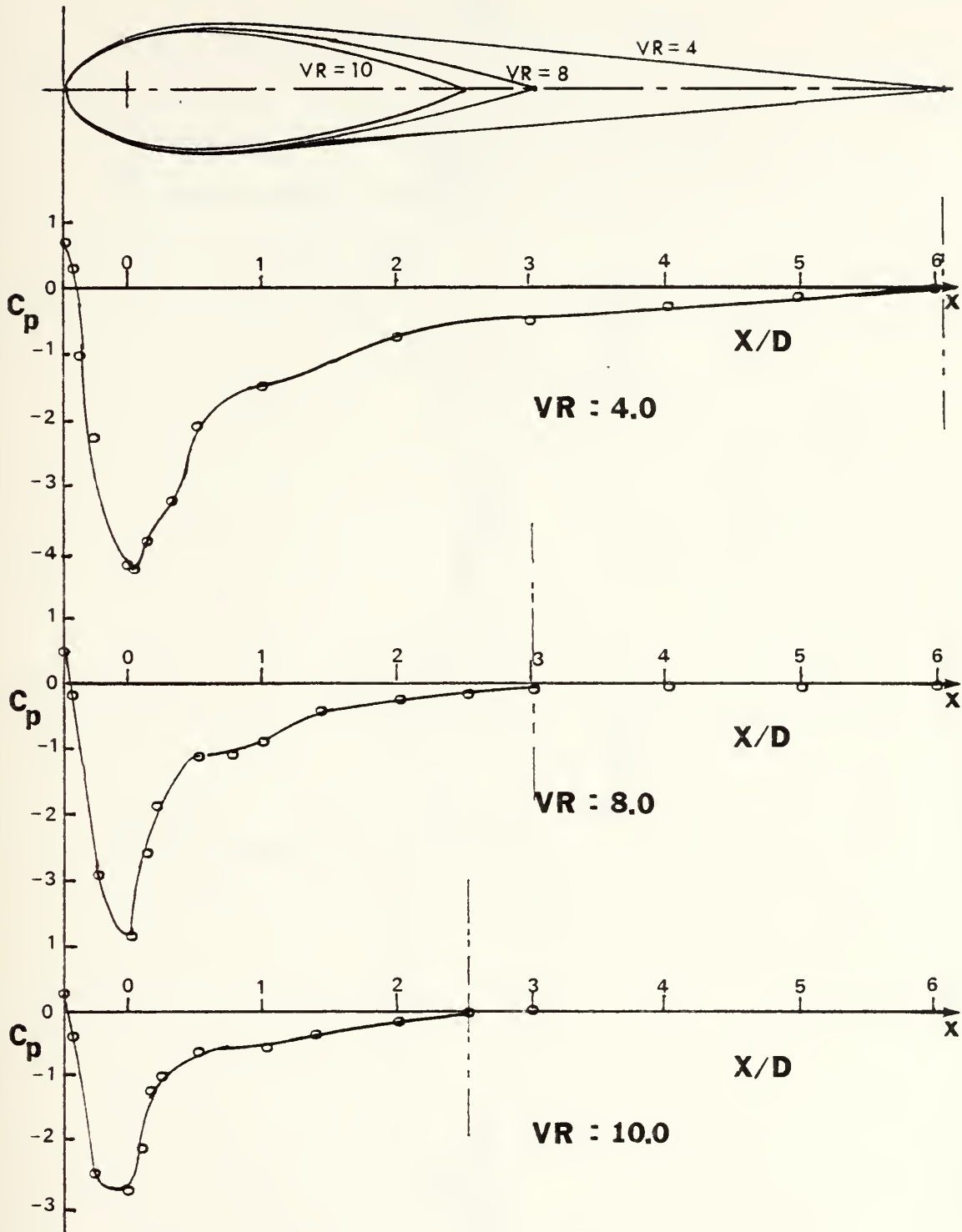


Figure 12. Plots of coefficients of pressure along the free-stream axis used to determine the length of the foil. Data from [5].



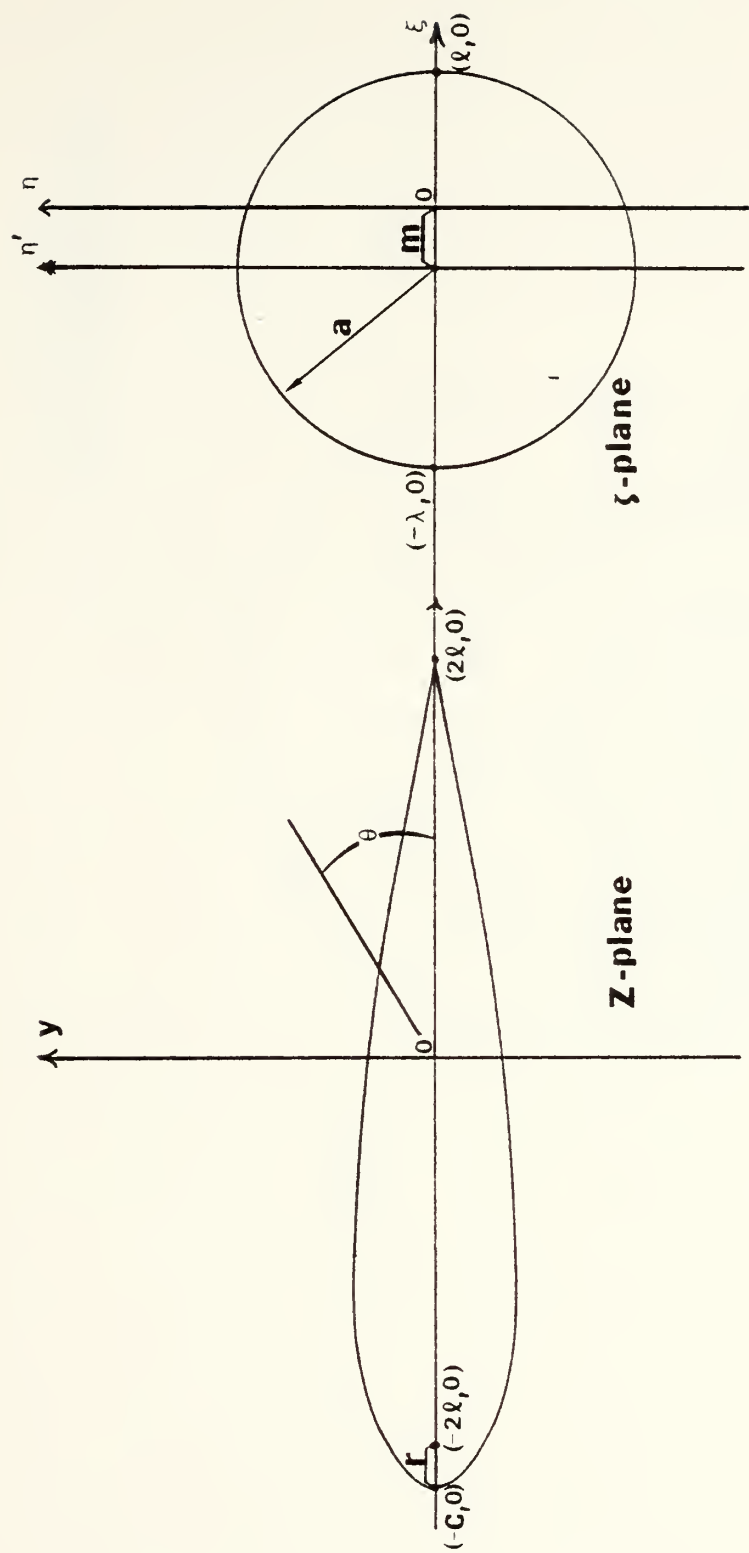


Figure 13. The Joukowski transformation.



— Present model  
 - - - Fearn & Weston [5]

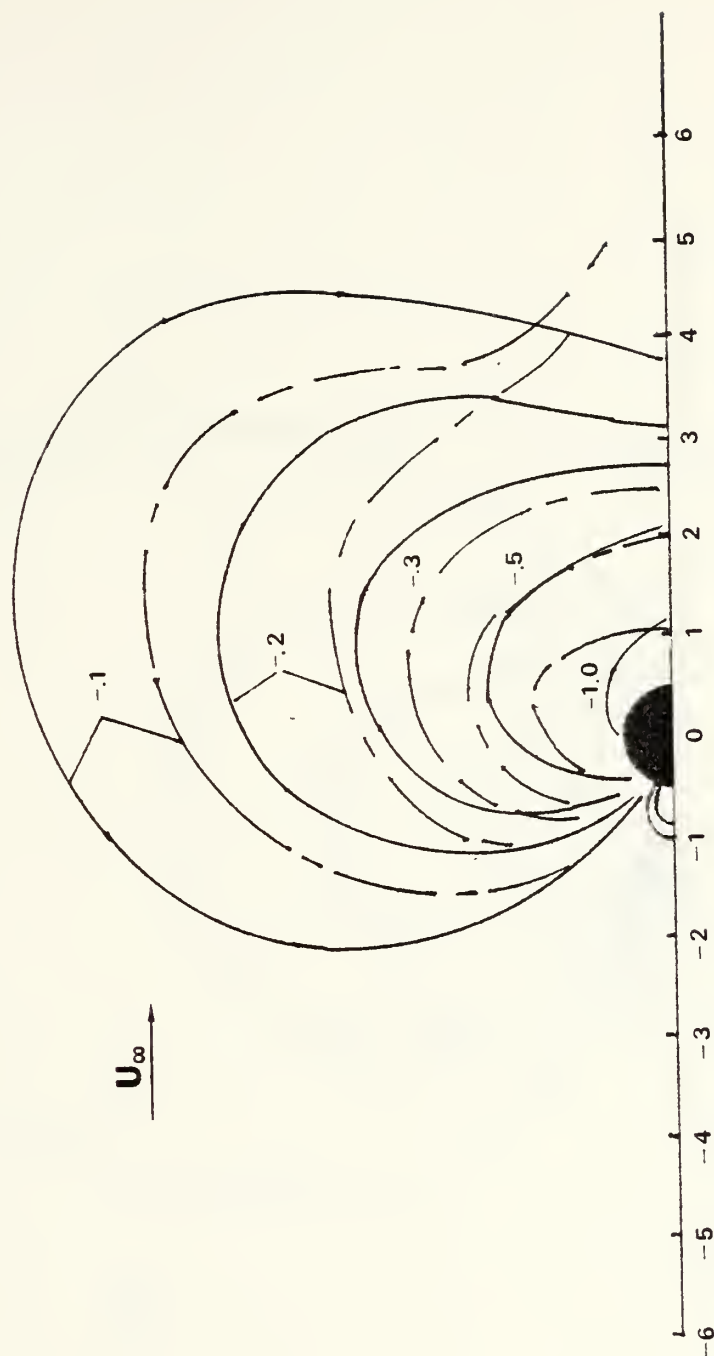


Figure 14. Comparison of pressure coefficient contours, experiment vs. present analytical model,  $VR=4$ .



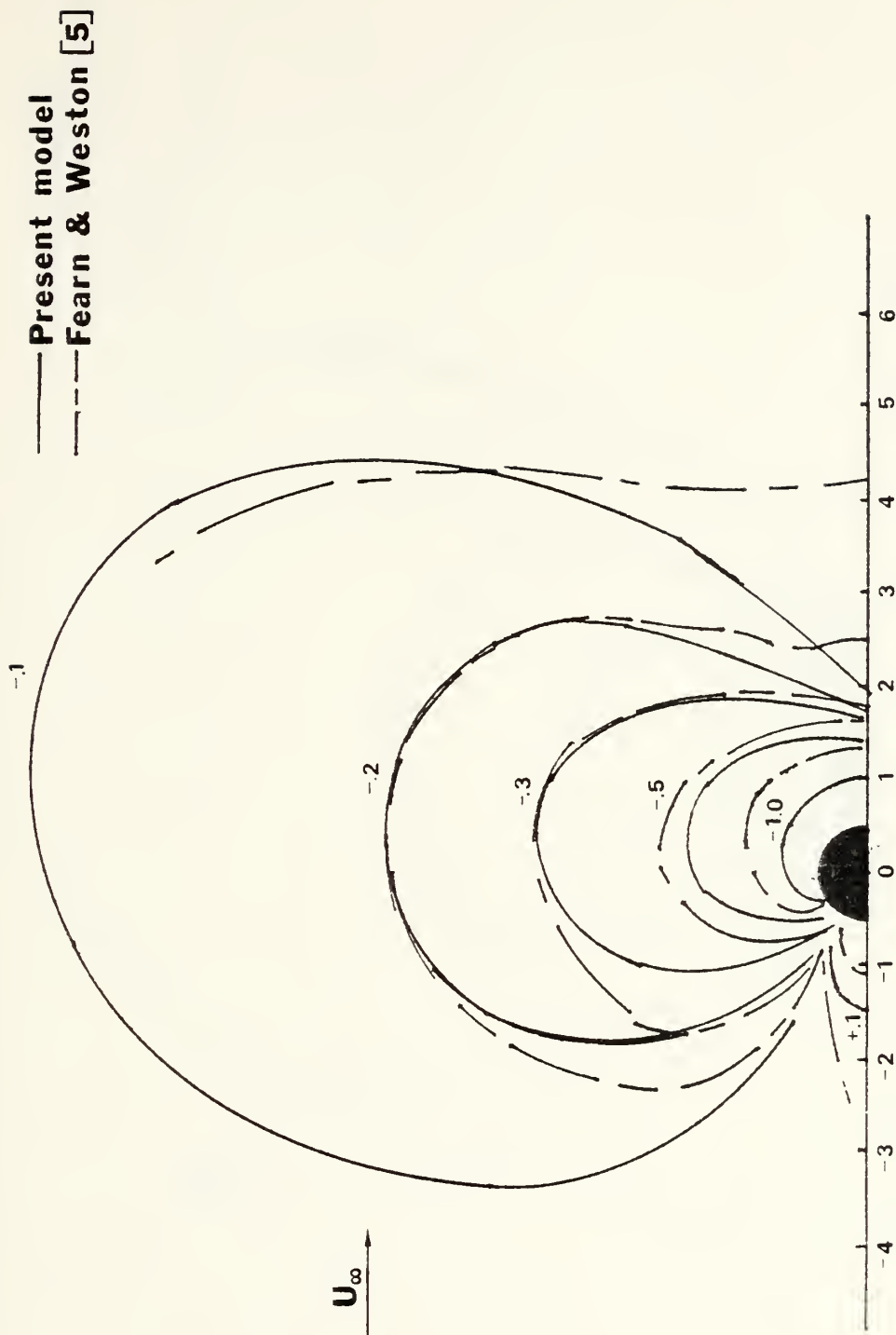


Figure 15. Comparison of pressure coefficient contours, experiment vs. present analytical model,  $VR=8$ .





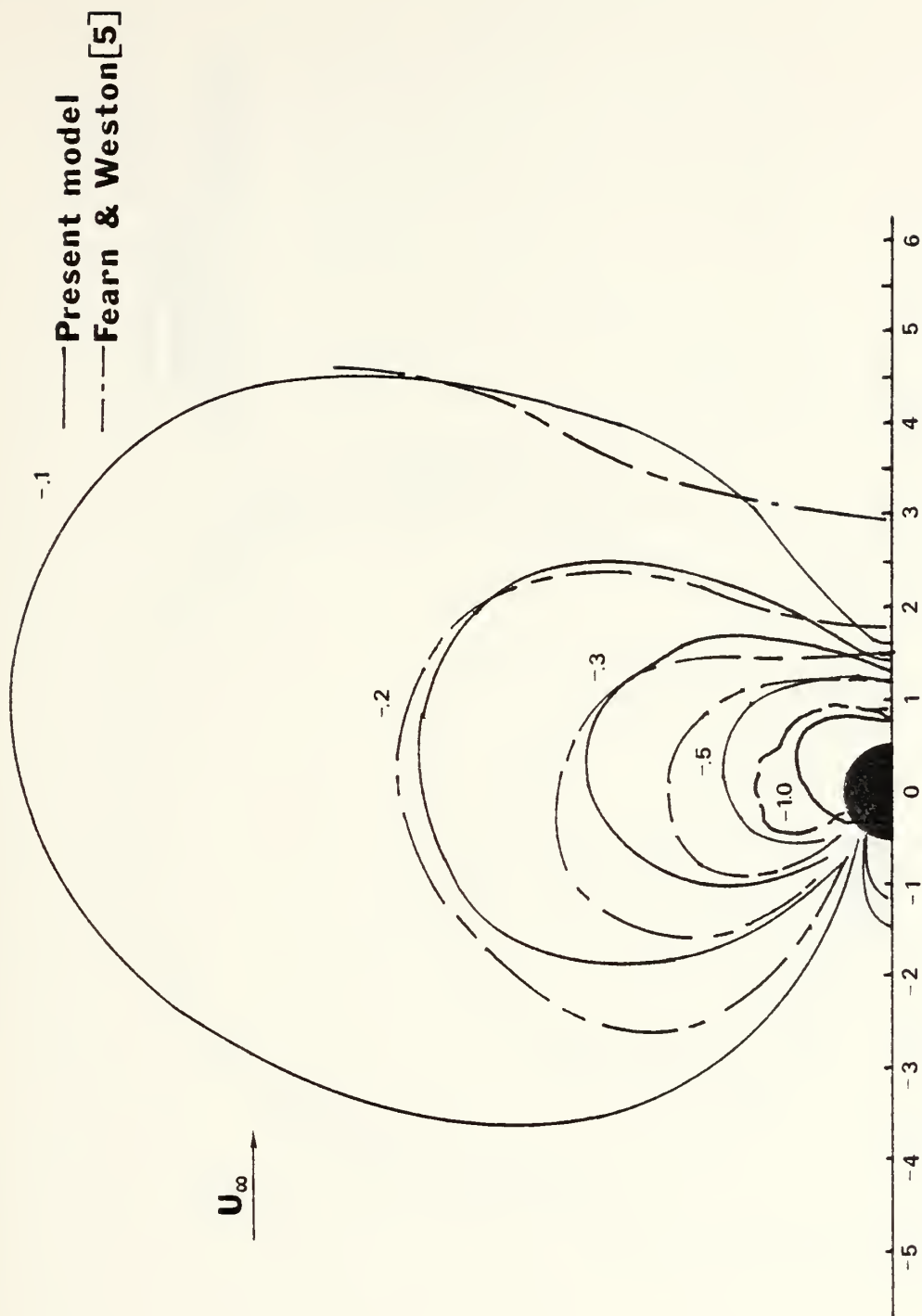


Figure 16. Comparison of pressure coefficient contours, experiment vs. present analytical model,  $VR=10$ .



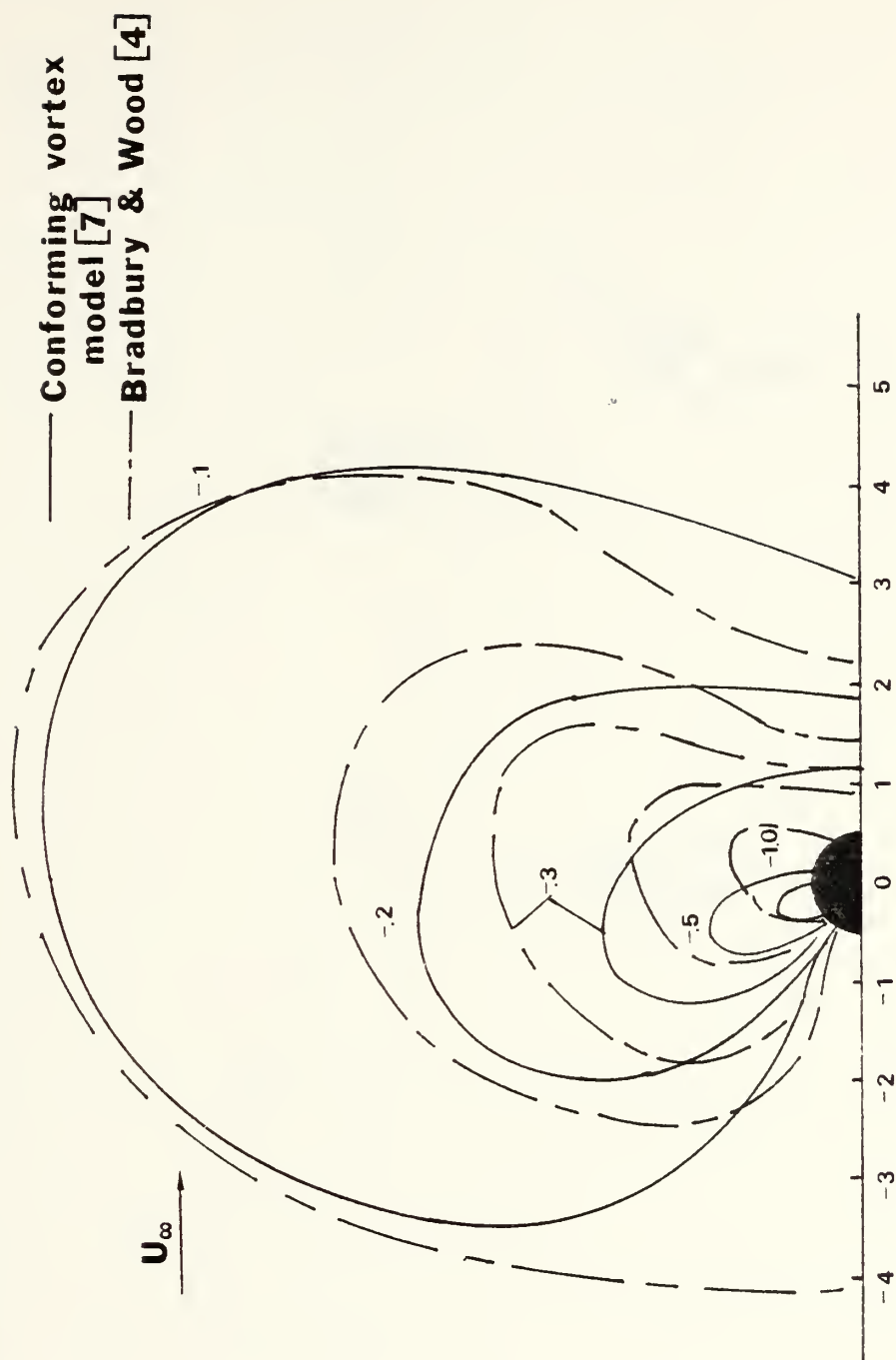


Figure 17. Conforming vortex model with a half cylinder for blockage correction vs. experiment,  $VR=8$ .



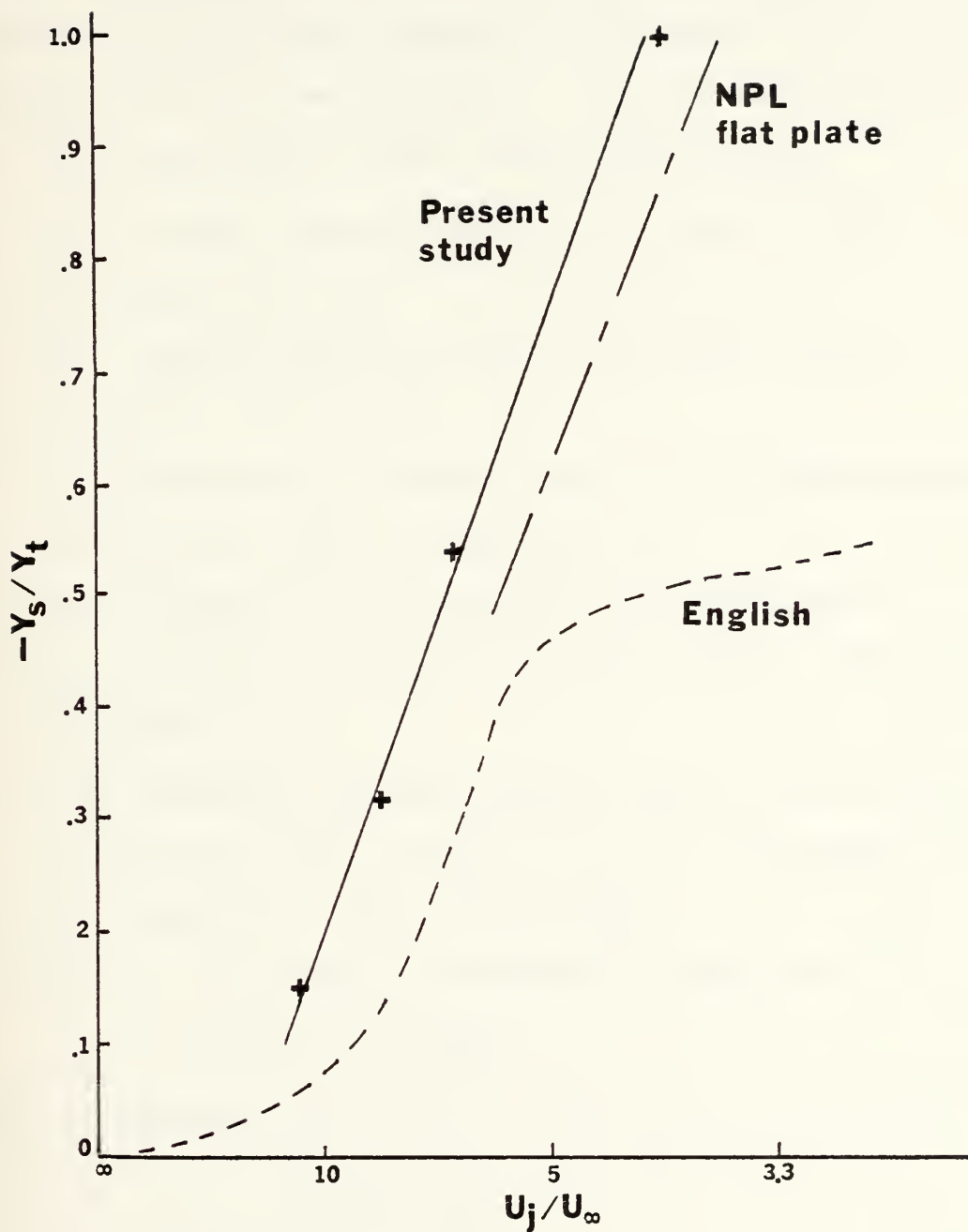


Figure 18. Comparison of theoretical values of  $-Y_s/Y_t$  with experimental findings. [1]



## APPENDIX A

### DERIVATION OF THE JOUKOWSKY TRANSFORMATION

The Joukowski transformation,  $Z = \zeta + \ell^2/\zeta$ , is used to transform a foil in the  $z$ -plane to a cylinder in the  $\zeta$ -plane so that the foil can be treated as a doublet in a uniform flow. The terms used in this transformation are:

$Z$  - the complex position vector of a point in the  $Z$ -plane  $Z = x + iy$

$\zeta$  - The complex position vector of a point in the  $\zeta$ -plane.  $\zeta = \xi + i\eta$

$\ell$  - A positive real constant equal to  $1/4$  the distance between the foci of the foil.

$a$  - The diameter of the cylinder in the  $\zeta'$ -plane.

$m$  - The distance between the  $\eta$  and  $\eta'$  axes. This is a function of  $r$ .

$r$  - The distance from the forward focus to the leading edge of the foil. That is  $r = |c - 2\ell|$  where  $-c$  is the abscissa of the leading edge.

$\zeta'$ -plane - The linearly transformed  $\zeta$ -plane used to give the foil thickness.  $\zeta' = \xi' + i\eta'$

From the Joukowski transformation and Fig. 13 it is seen that:

$$\zeta = .5(Z \pm \sqrt{Z^2 - 4\ell^2}) \quad (A1)$$





$$m = .5(\lambda - \ell) \quad (A2)$$

$$\zeta' = \zeta - (-m) = \zeta + m \quad (A3)$$

The complex potential of a cylinder in a uniform stream is given by:

$$\omega(\zeta') = U_{\infty}(\zeta' + a/\zeta') \quad (A4)$$

The complex velocity is then found as follows:

$$U_{\infty} + u - iv = \frac{d\omega}{dZ} = \frac{d\omega}{d\zeta'} \cdot \frac{d\zeta'}{dZ}$$

$$\frac{d\omega}{dZ} = \frac{d\omega}{d\zeta'} \cdot \frac{d\zeta'}{dZ} \quad (A5)$$

then substituting

$$\frac{d\omega}{dZ} = U_{\infty} \left( \frac{\zeta'}{\zeta} \right)^2 \frac{(\zeta'^2 - a^2)}{(\zeta^2 - \ell^2)}$$

and since  $\zeta' - a = \zeta - \ell$

$$\frac{d\omega}{dZ} = U_{\infty} \left( \frac{\zeta'}{\zeta} \right)^2 \frac{(\zeta' + a)}{(\zeta + \ell)} \quad (A6)$$



Then

$$\frac{u}{U_{\infty}} = \mathcal{R} \left[ \left( \frac{\zeta}{\zeta'} \right)^2 \frac{(\zeta' + a)}{(\zeta + \ell)} \right] - 1 \quad (\text{A7})$$

$$\frac{v}{U_{\infty}} = -\mathcal{I} \left[ \left( \frac{\zeta}{\zeta'} \right)^2 \frac{(\zeta' + a)}{(\zeta + \ell)} \right] \quad (\text{A8})$$



## APPENDIX B

### COMPUTER PROGRAM

```

XXXXXXXXXXXXXXXXXXXXXXXXXXXXX
X
X THIS PROGRAM SIMULATES A X
X FLUID JET INJECTED INTO X
X A UNIFORM CROSSFLOW AND X
X FURTHER DETERMINES THE X
X PRESSURE DISTRIBUTION ON X
X THE SURFACE FROM WHICH X
X THE JET IS EJECTED X
X
XXXXXXXXXXXXXXXXXXXXXXXXXXXXX

```

#### DEFINITION OF TERMS

NRAD - NUMBER OF RADIAL POSITIONS ON SURFACE  
 (INPUT)

NANG - NUMBER OF ANGULAR POSITIONS ON SURFACE  
 (INPUT)

NPOINT - NUMBER OF ARBITRARY POINTS ON SURFACE  
 (NRAD\*NANG)

UJ - JET VELOCITY (INPUT)

UM - MAIN STREAM VELOCITY (INPUT)

D - ACTUAL DIAMETER OF JET ORIFICE (INPUT)

R - NON-DIMENSIONAL RADIAL POSITION OF SURFACE  
 POINTS (DIMENSIONED AT LEAST NRAD) (INPUT)

THETA - ANGULAR POSITION OF SURFACE POINTS  
 (DIMENSIONED AT LEAST NANG)

XP - X-POSITION OF SURFACE POINTS  
 (DIMENSIONED AT LEAST NPOINT)

YP - Y-POSITION OF SURFACE POINTS  
 (DIMENSIONED AT LEAST NPOINT)

X - HORIZONTAL COORDINATE OF JET AXIS

Z - VERTICAL COORDINATE OF JET AXIS

ZINC - NON-DIMENSIONAL INCREMENTAL STEP SIZE FOR Z

DELTAZ - Z-POSITION OF EFFECTIVE/VIRTUAL SOURCE

HKSAV - CUMULATIVE VORTICITY ALONG THE JET

XI - NATURAL COORDINATE TANGENT TO JET

ZETA - NATURAL COORDINATE NORMAL TO JET

ETA - NATURAL COORDINATE PERPENDICULAR TO XI  
 AND ZETA

ALPHA - ANGLE BETWEEN X-AXIS AND XI-AXIS



```

C      PAREA  - INCREMENTAL PLATE AREA
C
C      TOTFCR - TOTAL RESULTANT FORCE ON PLATE
C
C      XRAR   - X-POSITION OF RESULTANT FORCE
C
C      YT     - NORMALIZED INDUCED FORCE
C
C      ELL    - 1/4 THE DISTANCE BETWEEN THE FOCI
C              OF THE FOIL USED FOR THE BLOCKAGE EFFECT
C
C      RADJ   - THE DISTANCE FROM THE FORWARD FOCUS OF THE
C              FOIL TO THE LEADING EDGE
C
C      ZCP    - THE COMPLEX VELOCITY INDUCED IN THE UNIFORM
C              FLOW DUE TO THE PRESENCE OF THE FOIL
C
C      IMPLICIT REAL*8 (A-H,O-Z)
C      DIMENSION U(50,50),V(50,50),W(50,50),R(50),THETA(50),
C      X VFL(450),CP(50,50)
C      DIMENSION XP(450),YP(450),ZP(450)
C      COMPLEX ZED*16,ZST*16,ZCP*16,ZSTP*16,ZR*16,
C      *ZEL*16,Z4*16,ZHA*16,ZM*16
C DATA INPUT
C      READ(5,60) NRAD
C      READ(5,60) NANG
C 6C FORMAT(I4)
C      NPOINT = NRAD*NANG
C      ZERO OUT STORAGE MATRICES
C      DO 30 I = 1,NRAD
C      DO 20 J = 1,NANG
C      U(I,J) = 0.0
C      V(I,J) = 0.0
C      CP(I,J) = 0.0
C 20 CONTINUE
C 30 CONTINUE
C      READ(5,40) UJ,UM,D
C      WRITE(6,50) UJ,UM,D
C      VELOCITY RATIO
C      VR = (UJ/UM)
C      READ(5,70) ZINC
C      READ(5,70) (R(I),I=1,NRAD)
C 70 FORMAT(F10.5)
C      SET CONSTANTS USED IN FOIL BLOCKAGE CALCULATIONS
C      BL = 1.0
C      BHA = 0.5
C      B4 = 4.0
C      SET FOIL PARAMETERS
C      ELL = 6.0/VR
C      RADJ = .12/ELL
C      ALAM = .5*(2.*ELL+RADJ+DSQRT((2.*ELL+RADJ)**2-
C      *4.0*ELL**2))
C      EM = 0.5*(ALAM - ELL)
C      POSITION OF EFFECTIVE SOURCE
C      DELTAZ = .6*DSQRT(VR)
C      WRITE(6,80) DELTAZ
C      WRITE(6,90) ZINC
C 40 FORMAT(3F3.4)
C 50 FORMAT('0',2X,'JET VELOCITY = ',F3.4,2X,'UNIFORM',
C      X'VELOCITY = ',F3.4,2X,'JET DIAMETER = ',F3.4)
C 80 FORMAT('0',2X,'EFFECTIVE SOURCE IS',F5.2,2X,
C      X'DIAMETERS ABOVE THE PLATE')
C 90 FORMAT('0',2X,'Z STEP SIZE = ',F5.3)
C      DEFINITION OF PI
C      PI = 2.0*AR SIN(1.00000000)
C      TRAJECTORY CONSTANT
C      B = 0.19*VR**2

```





```

C  CALCULATION OF INTERFERENCE VELOCITY
    L = 0
    CALCON = DFLQAT(NANG) - 1.0
C  INCREMENT RADIUS (INPUT VALUES)
    DO 140 I = 1, NRAD
        RCALC = R(I)
C  INCREMENT THETA (5 DEGREE INCREMENTS)
    DO 130 J = 1, NANG
        K = J-1
        THETA(J) = DFLQAT(K)* (PI/CALCON)
        ARAD = ALAM - EM
C  SHIFT TO CARTESIAN COORDINATES
        L = L+1
        XP(L) = RCALC*DCOS(THETA(J))
        YP(L) = RCALC*DSIN(THETA(J))
        HKSAV = 0.0
100    Z2 = 0.00001
        Z1 = Z2
        Z2 = Z1 + ZINC
        Z11 = Z1 + DELTAZ
        Z22 = Z2 + DELTAZ
C
        X1 = B*(DCOSH(Z1/B)-1.0)
        X2 = B*(DCOSH(Z2/B)-1.0)
C
        ALFONE = DATAN(1.0/DSINH(Z1/B))
        ALFTWO = DATAN(1.0/DSINH(Z2/B))
        ALFBAR = DATAN((Z2-Z1)/(X2-X1))
C
        SINAI = DSIN(ALFONE)
        SINAI2 = DSIN(ALFTWO)
        SINAB = DSIN(ALFBAR)
C
        COSAI = DCOS(ALFONE)
        COSAI2 = DCOS(ALFTWO)
        COSAB = DCOS(ALFBAR)
C  NATURAL COORDINATES IN TERMS OF CARTESIAN COORDINATES
        XIONE = -(Z11*SINAI + (X1-XP(L))*COSAI)
        XITWO = -(Z22*SINAI2 + (X2-XP(L))*COSAI2)
        XIBAR1 = -(Z11*SINAB + (X1-XP(L))*COSAB)
        XIBAR2 = -(Z22*SINAB + (X2-XP(L))*COSAB)
C
        ETA = YP(L)
C
        ZETA1 = (Z11*COSAI - (X1-XP(L))*SINAI)
        ZETA2 = (Z22*COSAI2 - (X2-XP(L))*SINAI2)
        ZETAB = (Z11*COSAB - (X1-XP(L))*SINAB)
C  GEOMETRIC CONSTANTS
        ETPL = ETA + 0.5
        ETMI = ETA - 0.5
        SA = XIONE**2
        SB = XITWO**2
        SC = XIBAR1**2
        SD = XIBAR2**2
        SE = ZETA1**2
        SF = ZETA2**2
        SG = ZETAB**2
        SH = ETPL**2
        SI = ETMI**2
        DA = DSQRT(SA + SF + SH)
        DB = DSQRT(SA + SE + SI)
        DC = DSQRT(SB + SF + SH)
        DE = DSQRT(SB + SE + SI)
        DF = DSQRT(SD + SG + SI)

```



```

      DG = DSQRT(SC + SG + SI)
      DH = DSQRT(SD + SG + SH)
      DI = DSQRT(SC + SG + SH)

C
      CON1 = (ETPL/DA - ETMI/DB)/(SA + SE)
      CON2 = (ETPL/DC - ETMI/DE)/(SB + SF)
      CON3 = (XIBAR2/DF - XIBAR1/DG)/(SG + SI)
      CON4 = (XIBAR2/DH - XIBAR1/DI)/(SG + SH)

C
      U1 = ZETA1*CON1
      U2 = ZETA2*CON2
      V3 = ZETAB*CON3
      V4 = ZETAB*CON4
      W1 = XICNE*CON1
      W2 = XITWD*CON2
      W3 = ETMI*CON3
      W4 = ETPL*CON4

C INCREMENTAL VORTICITY TERM
      FF = ((DEXP(Z2/B)-DEXP(Z1/B))/(1.0+DEXP((Z2+Z1)/B)))
      HK = (1.0/8.0)*VR**2 * DATAN(FF)
      HK = HK + HKSAV
      HKSAV = HK

C INCREMENTAL INTERFERENCE VELOCITY COMPONENTS
      UP = 0.0
      UP = HK*((-W1*SINA1+W2*SINA2+(-W3+W4)*SINAB+U1*COSA1)
      X -(U2*COSA2))
      VP = 0.0
      VP = HK*(V3 - V4)
      U(I,J) = U(I,J) + UP*2.0
      V(I,J) = V(I,J) + VP*2.0

C TEST FOR CONVERGENCE
      TEST = DABS(UP) + DABS(VP)
      IF (TEST.LE.0.000001) GO TO 110
      GO TO 100
110 CONTINUE

C CALCULATION OF BLOCKAGE VELOCITY TERM
C TRANSFORM COORDINATES TO Z PLANE
83 AZ = XP(L)- 2.0*ELL + (.5-RADJ)
      IF (AZ.EQ.0.0.AND.YP(L).EQ.0.0) GO TO 115
C CHANGE VARIABLES TO COMPLEX NUMBERS
      BZ = YP(L)
      BB = 0.0
      ZED = DCMPLX(AZ,BZ)
      ZR = DCMPLX(ARAD,BB)
      ZEL = DCMPLX(ELL,BB)
      Z4 = DCMPLX(B4,BB)
      ZM = DCMPLX(EM,BB)
      ZHA = DCMPLX(BHA,BB)
      IF (AZ.LT.0.0) GO TO 89
C TRANSFORM POSITION VECTOR IN Z PLANE TO ZETA PLANE
      ZST = ZHA*(ZED + CDSQRT(ZED**2-Z4*ZEL**2))
      GO TO 91
89 ZST = ZHA*(ZED - CDSQRT(ZED**2-Z4*ZEL**2))
C TRANSFORM POSITION VECTORS FROM ZETA PLANE TO
C ZETA PRIME PLANE
91 ZSTP = ZST + ZM
C SET VELOCITIES TO ZERO WHEN WITHIN THE FOIL
      XED = DREAL(ZSTP)
      YED = DIMAG(ZSTP)
      PR = DSQRT(XED**2 + YED**2)
      IF (PR.LE.(ARAD/14.0)) GO TO 95
C CALCULATE THE DERIVATIVE OF THE COMPLEX POTENTIAL
95 ZCP = ((ZST/ZSTP)**2)*(ZSTP + ARAD)/(ZST + ELL)
C EXTRACT THE HORIZ. AND VERT. PERTABATION VELOCITIES
      UC = DREAL(ZCP) - 1.0
      VC = -DIMAG(ZCP)
      GO TO 119

```



```

115 UC = 0.0
    VC = 0.0
119 U(I,J) = U(I,J) + UC
    V(I,J) = V(I,J) + VC
C  CALCULATION OF PRESSURE COEFFICIENT
120 CP(I,J) = -2.0*(U(I,J)**2 + .5*V(I,J)**2)
C  CHANGE DESIGNATION OF VARIABLE
    ZP(I) = CP(I,J)
    VEL(I) = DSQRT((U(I,J)+1.0)**2 + V(I,J)**2)
130 CONTINUE
140 CONTINUE
C  CALCULATION OF INCREMENTAL FORCE
    TOTFOR = 0.0
    TYMOM = 0.0
    NAREA = NRAD - 1
    DO 170 I=1,NAREA
        K = I + 1
        RI = R(I)
        RK = R(K)
C  CALCULATION OF INCREMENTAL AREA
        AREA = PI*(RK**2 - RI**2)
        PAPEA = AREA/(2.0*CALCON)
    DO 160 J=1,NANG
C  CALCULATION OF AVERAGE PRESSURE COEFFICIENT
        CPAVG = (CP(I,J) + CP(K,J))/2.0
C  CALCULATION OF EFFECTIVE FORCE
        FORCE = PAPEA*CPAVG
        IF(J.EQ.1) GO TO 150
        IF(J.EQ.NANG) GO TO 150
        FORCE = 2.0*FORCE
C  CALCULATION OF MOMENT ARM
150 XM = ((RK + RI)/2.0)*DCOS(THETA(J))
C  CALCULATION OF MOMENT ABOUT Y-AXIS
        YMOM = FORCE*XM
C  SUMMATION OF TOTAL FORCE
        TOTFOR = TOTFOR + FORCE
C  SUMMATION OF TOTAL MOMENT
        TYMOM = TYMOM + YMOM
160 CONTINUE
170 CONTINUE
C  CALCULATION OF CENTER OF ACTION
    XBAR = TYMOM/TOTFOR
C  CALCULATION OF NORMALIZED INDUCED FORCE: Y/T
    VRINV = 1.0/VR
    YT = 2.0*TOTFOR*VRINV**2/PI
C  DATA OUTPUT
    WRITE(6,230) TOTFOR,XBAR
    WRITE(6,240) YT, VRINV
180 DO 220 I = 1,NANG
    ANGLE = THETA(I)*180.0/PI
    WRITE(6,190) ANGLE
190 FORMAT('0',2X,'THETA = ',F6.2,8X,'R',9X,'CP',9X,'U',
    X 9X,'V')
    DO 210 J = 1,NRAD
        WRITE(6,200) R(J),CP(J,I),U(J,I),V(J,I)
200 FORMAT(' ',23X,F6.2,2X,F8.2,3X,F6.2,4X,F6.2)
210 CONTINUE
220 CONTINUE
230 FORMAT('0',2X,'RESULTANT FORCE OF ',1X,F7.2,1X,
    X'ACTS AT X = ',F6.2)
240 FORMAT('0',2X,'Y/T = ',F6.2,1X,'FOR UM/UJ = ',F6.3)
    WRITE(7,250)(XP(I),YP(I),ZP(I),I=1,NPOINT)
250 FORMAT(3F20.4)
270 STOP
    END

```



# APPENDIX C

## COMPARISON OF PRESENT MODEL WITH EXPERIMENTAL RESULTS

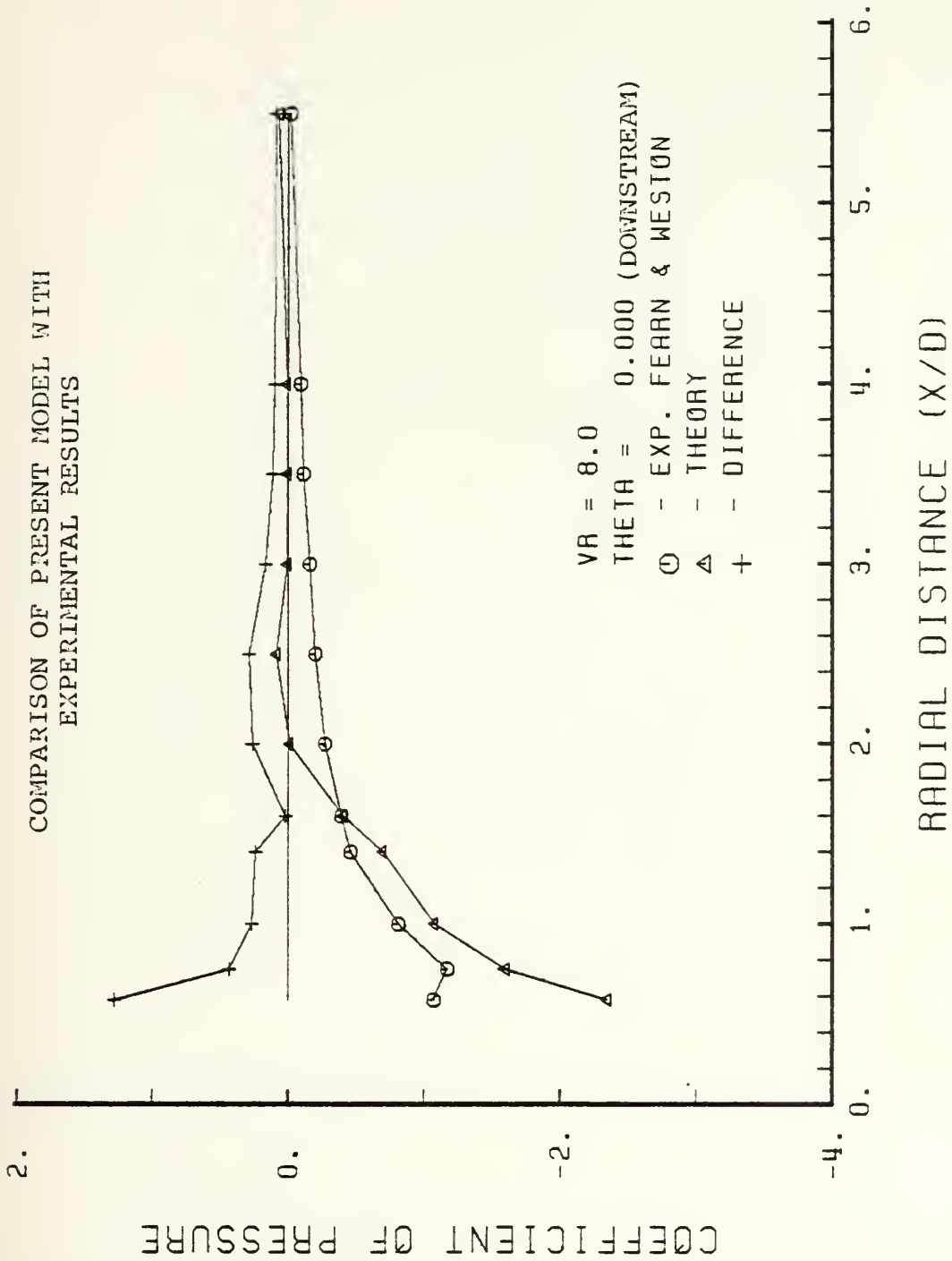


Figure C-1.  $C_p$ 's along radial lines, VR = 8, theta = 0 degrees.





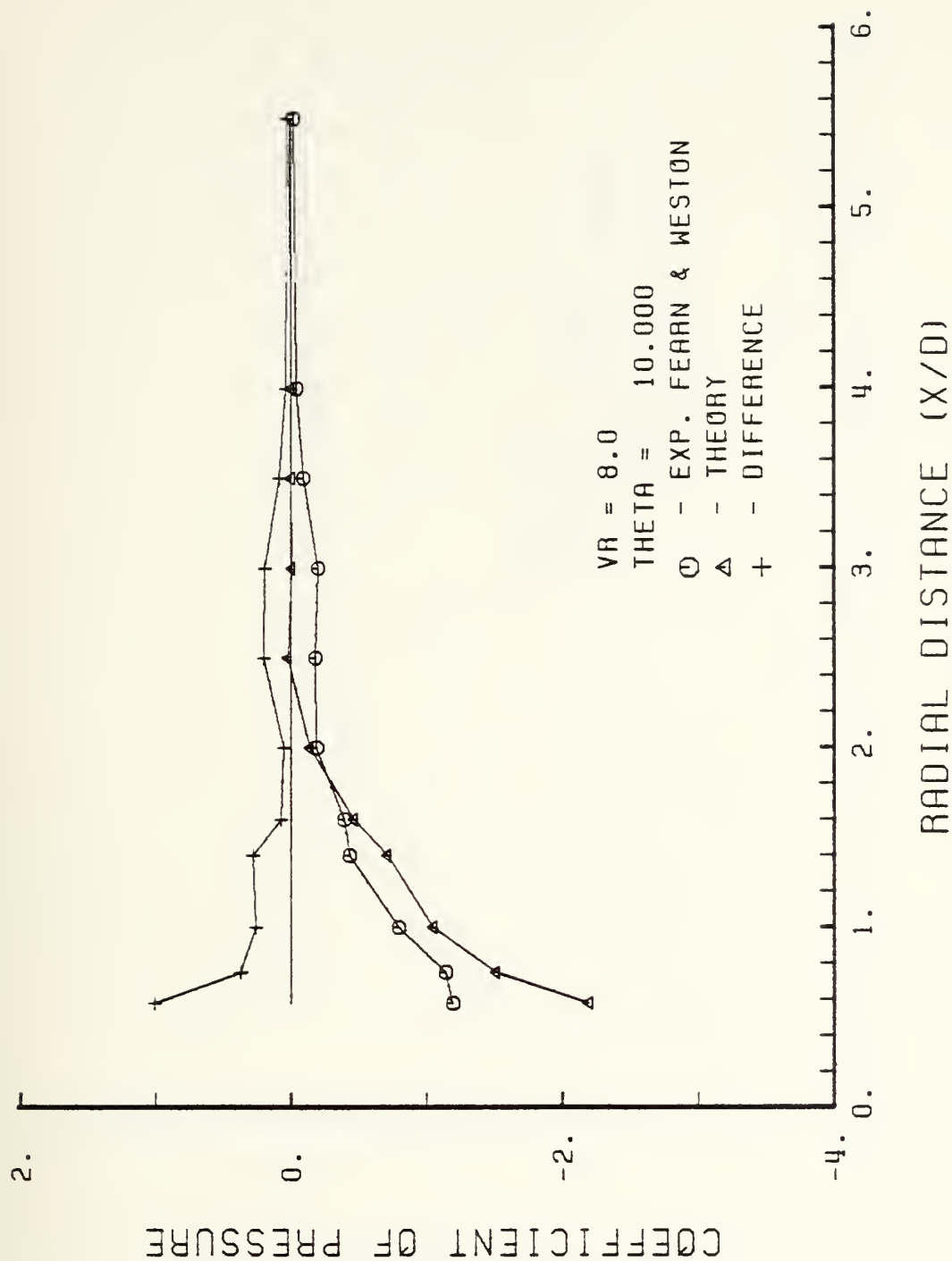


Figure C-2.  $C_p$ 's along radial lines, VR = 8, theta = 10 degrees.



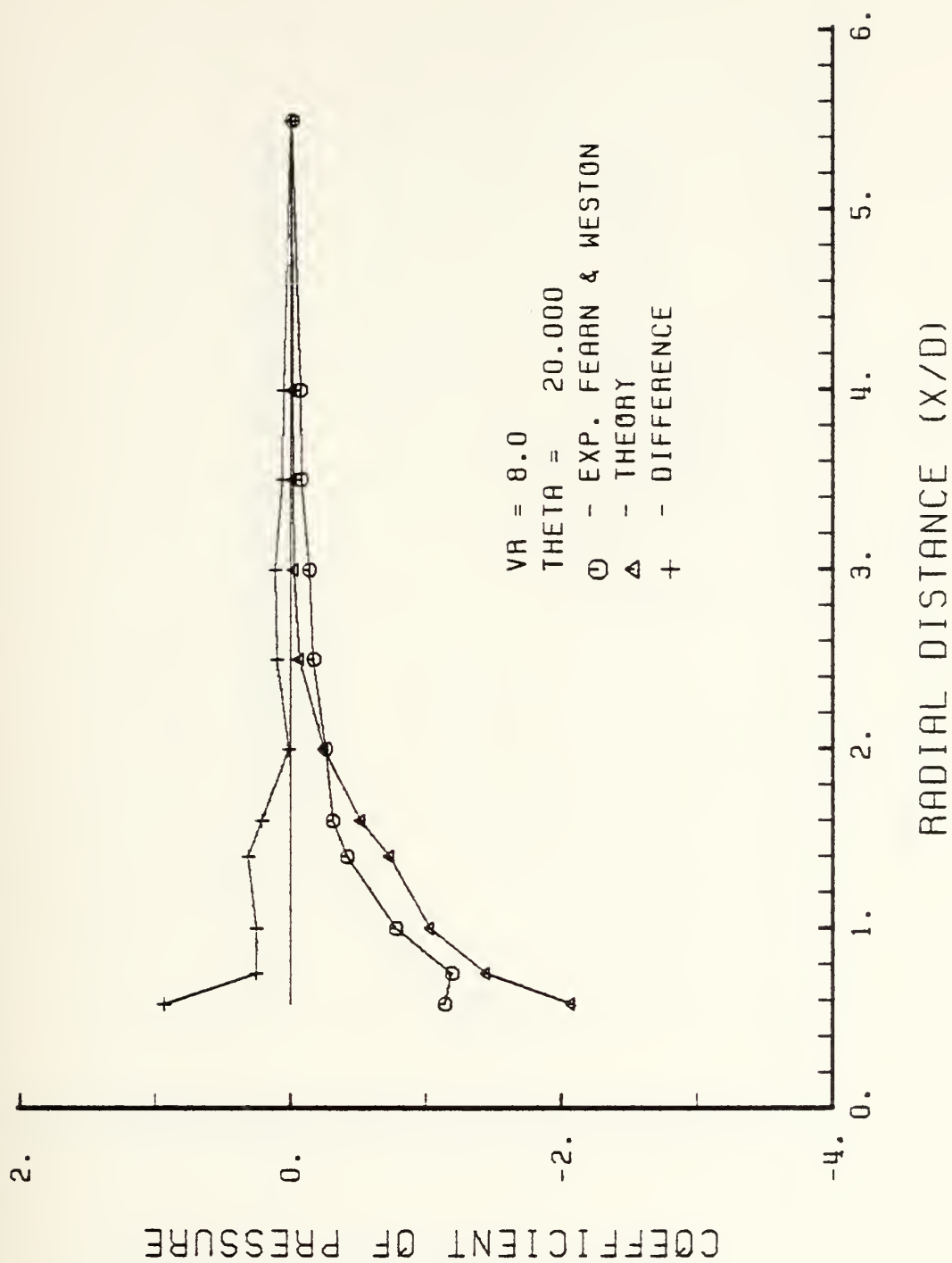


Figure C-3.  $C_p$ 's along radial lines, VR = 8, theta = 20 degrees.



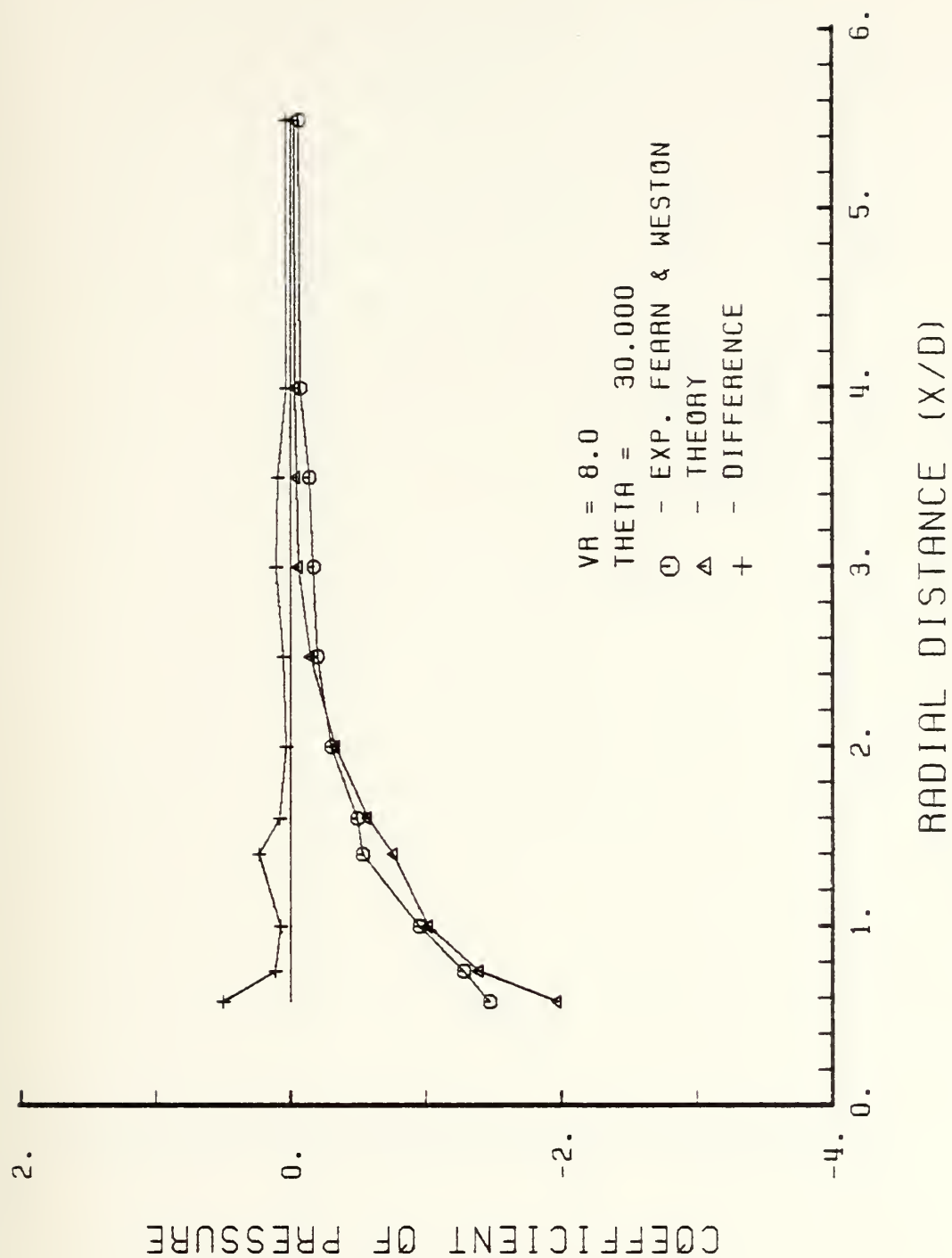


Figure C-4.  $C_p$ 's along radial lines, VR = 8, theta = 30 degrees.



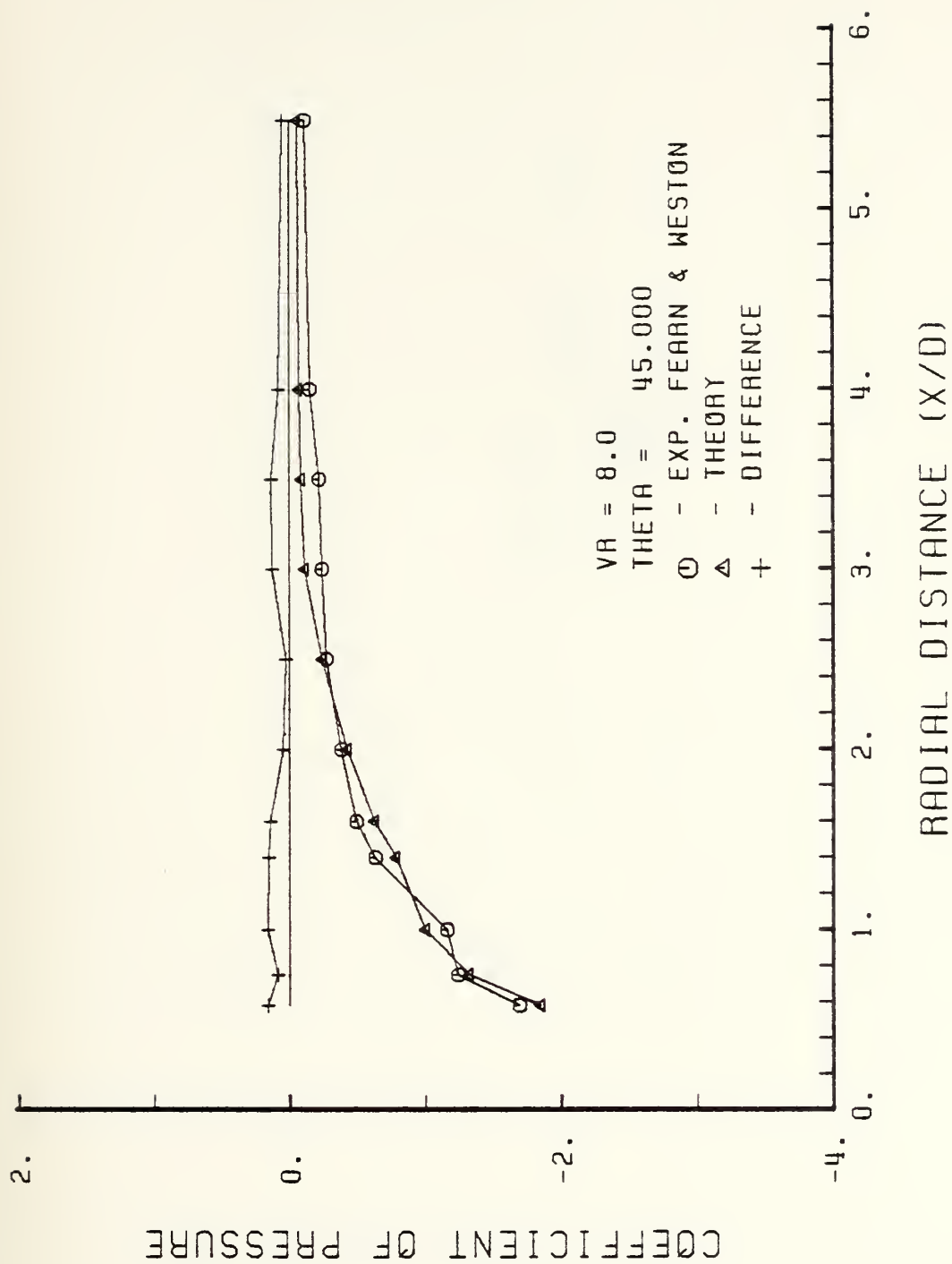


Figure C-5.  $C_p$ 's along radial lines,  $VR = 8$ ,  $\theta = 45$  degrees.





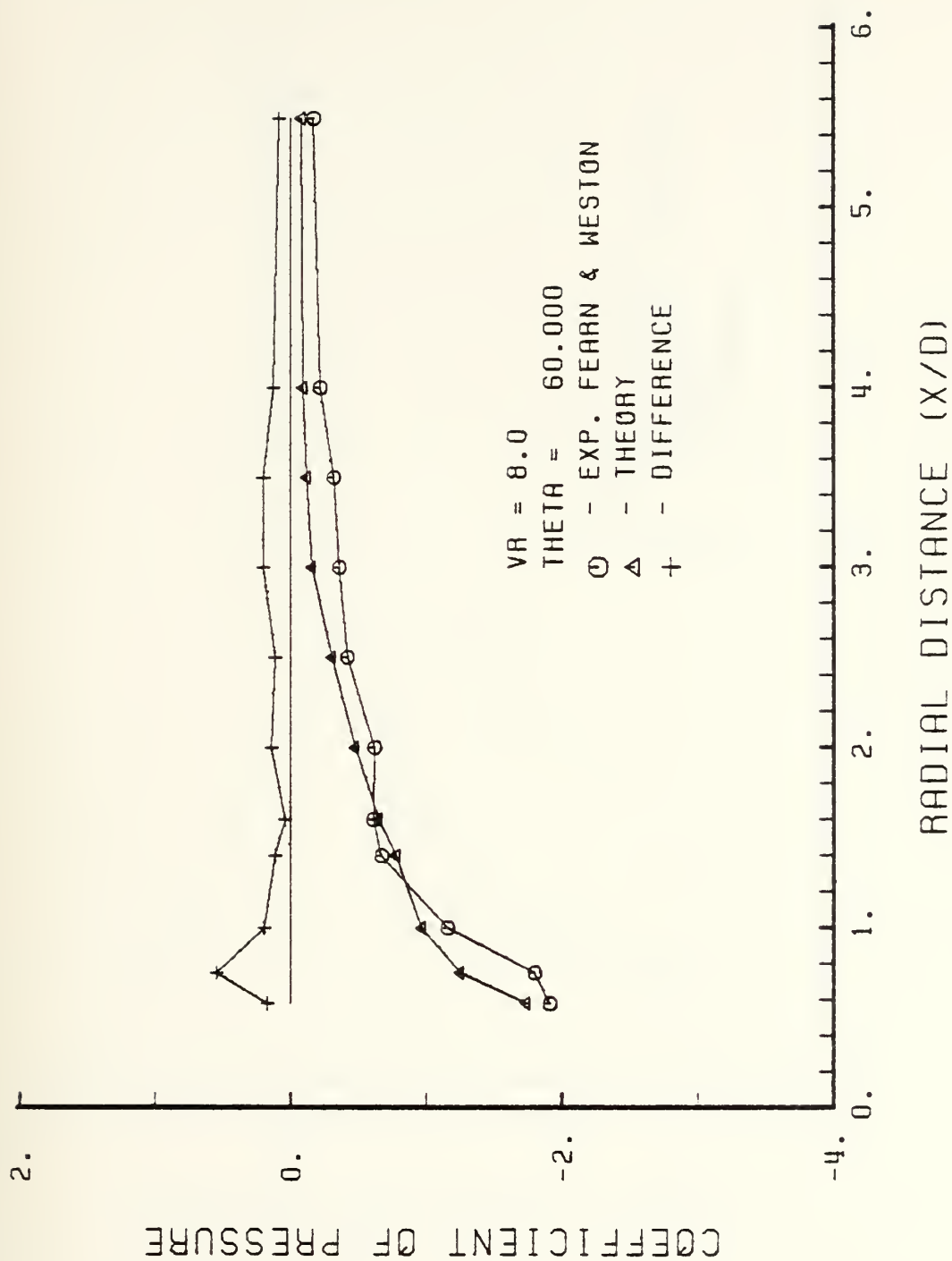


Figure C-6.  $C_p$ 's along radial lines, VR = 8, theta = 60 degrees.



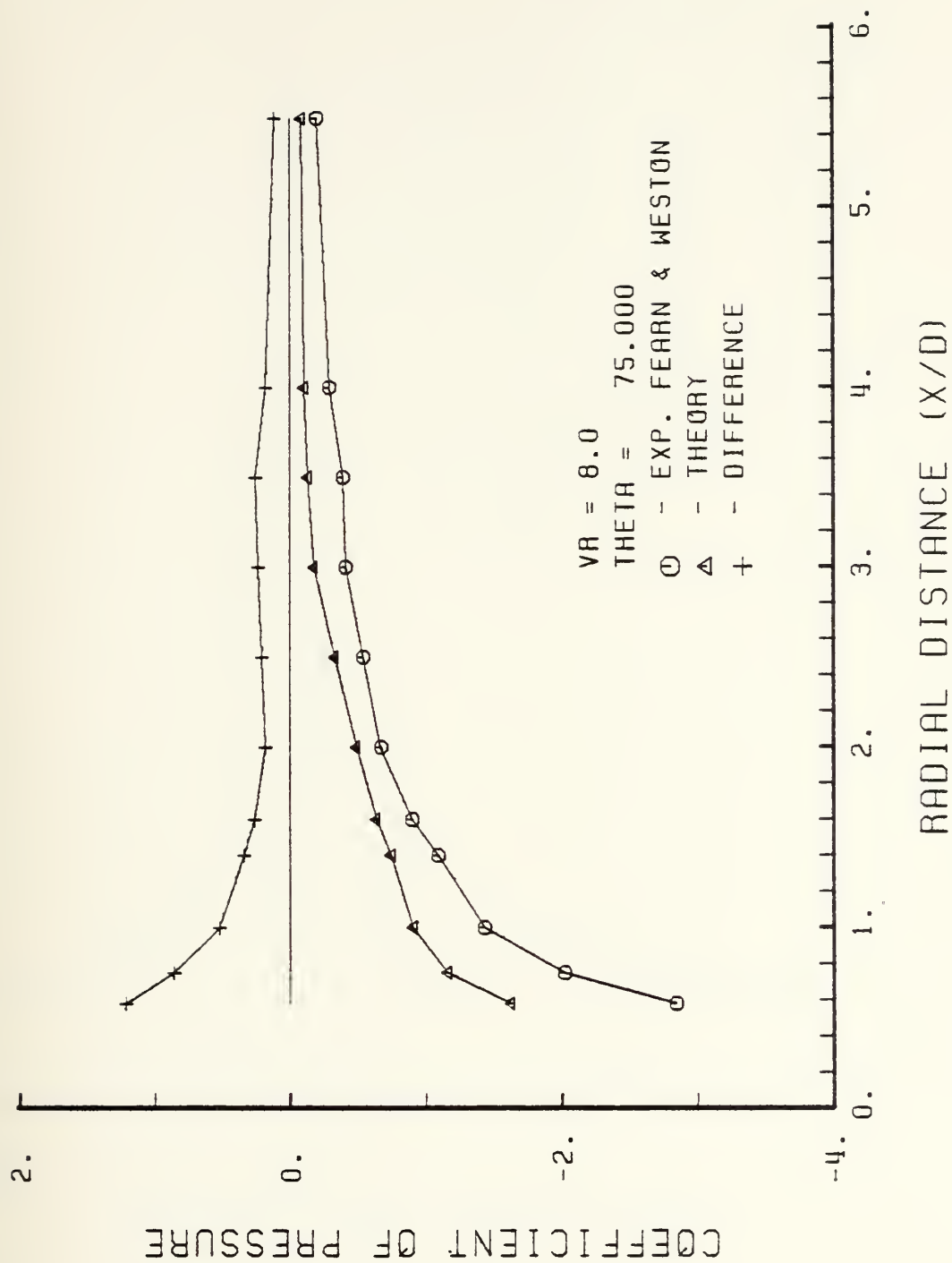


Figure C-7.  $C_p$ 's along radial lines, VR = 8, theta = 75 degrees.



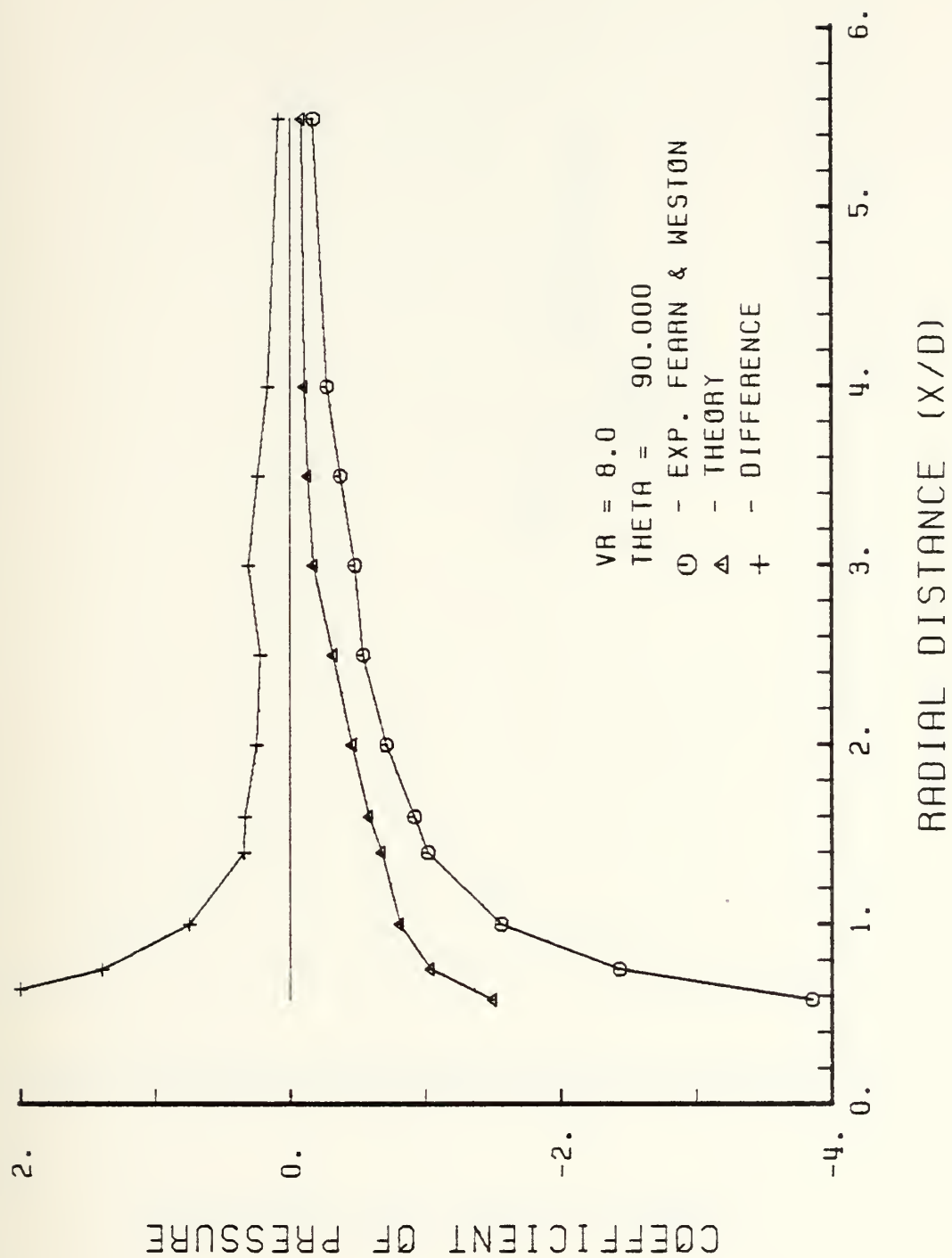


Figure C-8.  $C_p$ 's along radial lines, VR = 8, theta = 90 degrees.



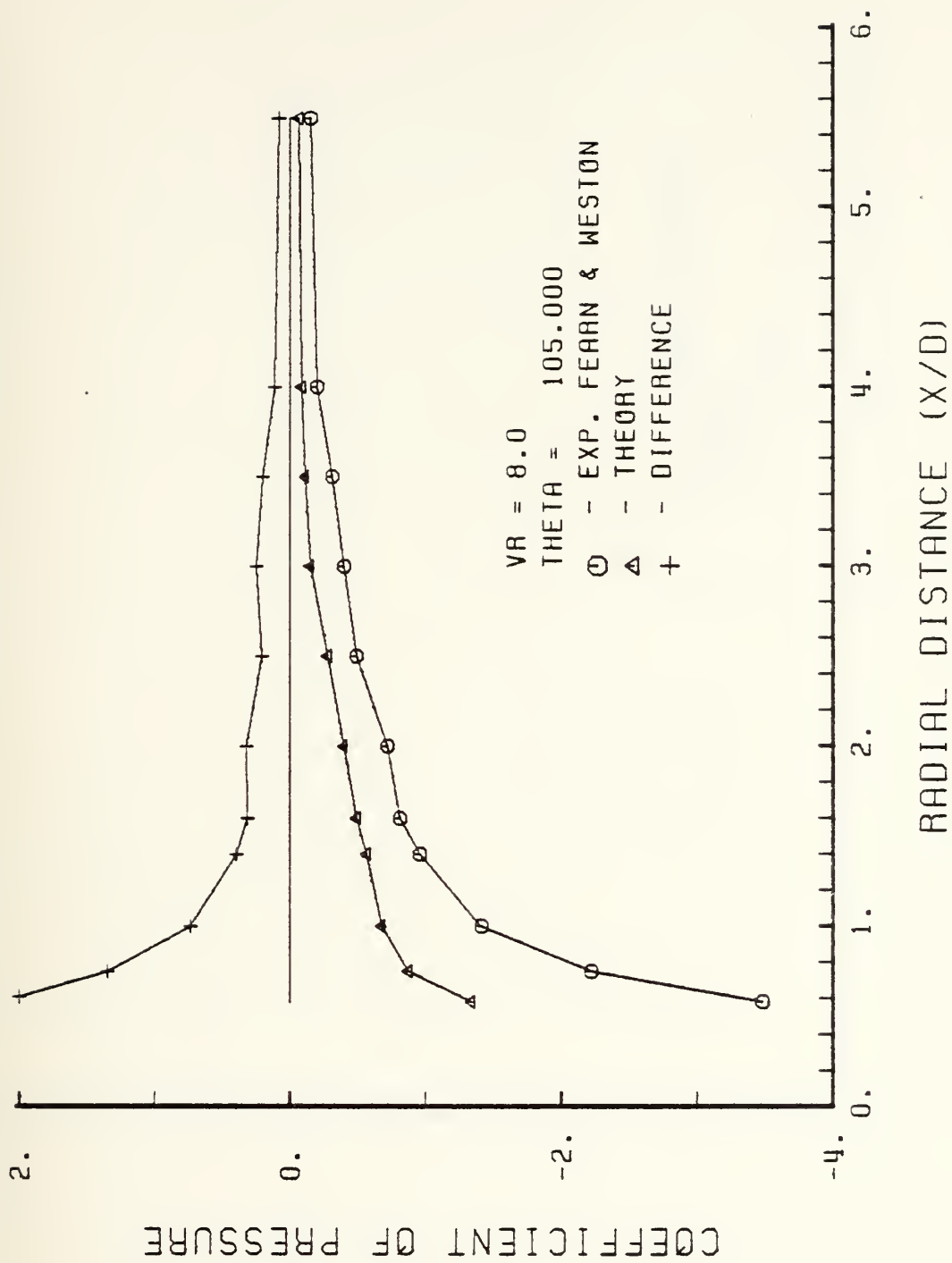


Figure C-9.  $C_p$ 's along radial lines, VR = 8, theta = 105 degrees.





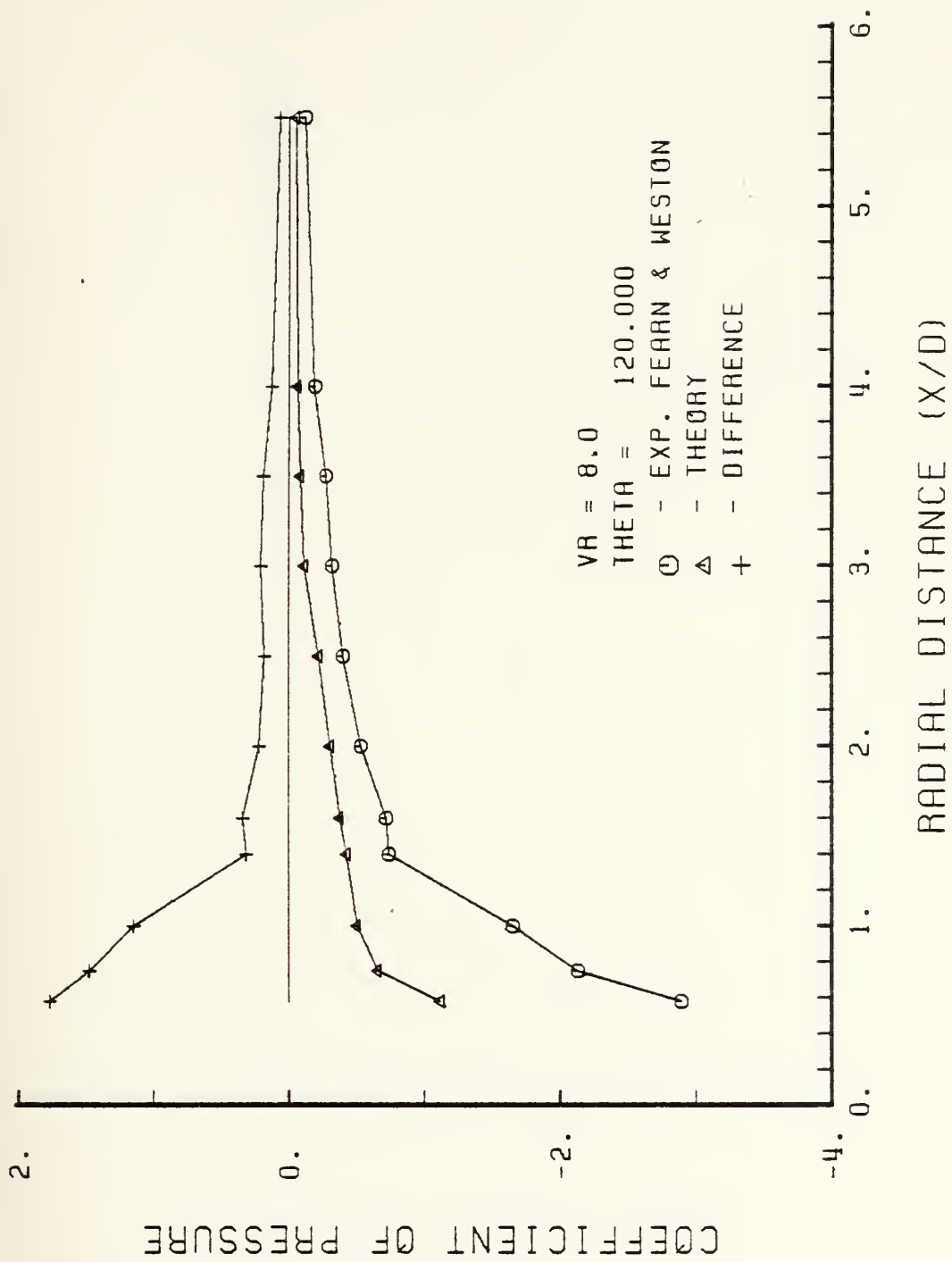


Figure C-10.  $C_p$ 's along radial lines, VR = 8, theta = 120 degrees.



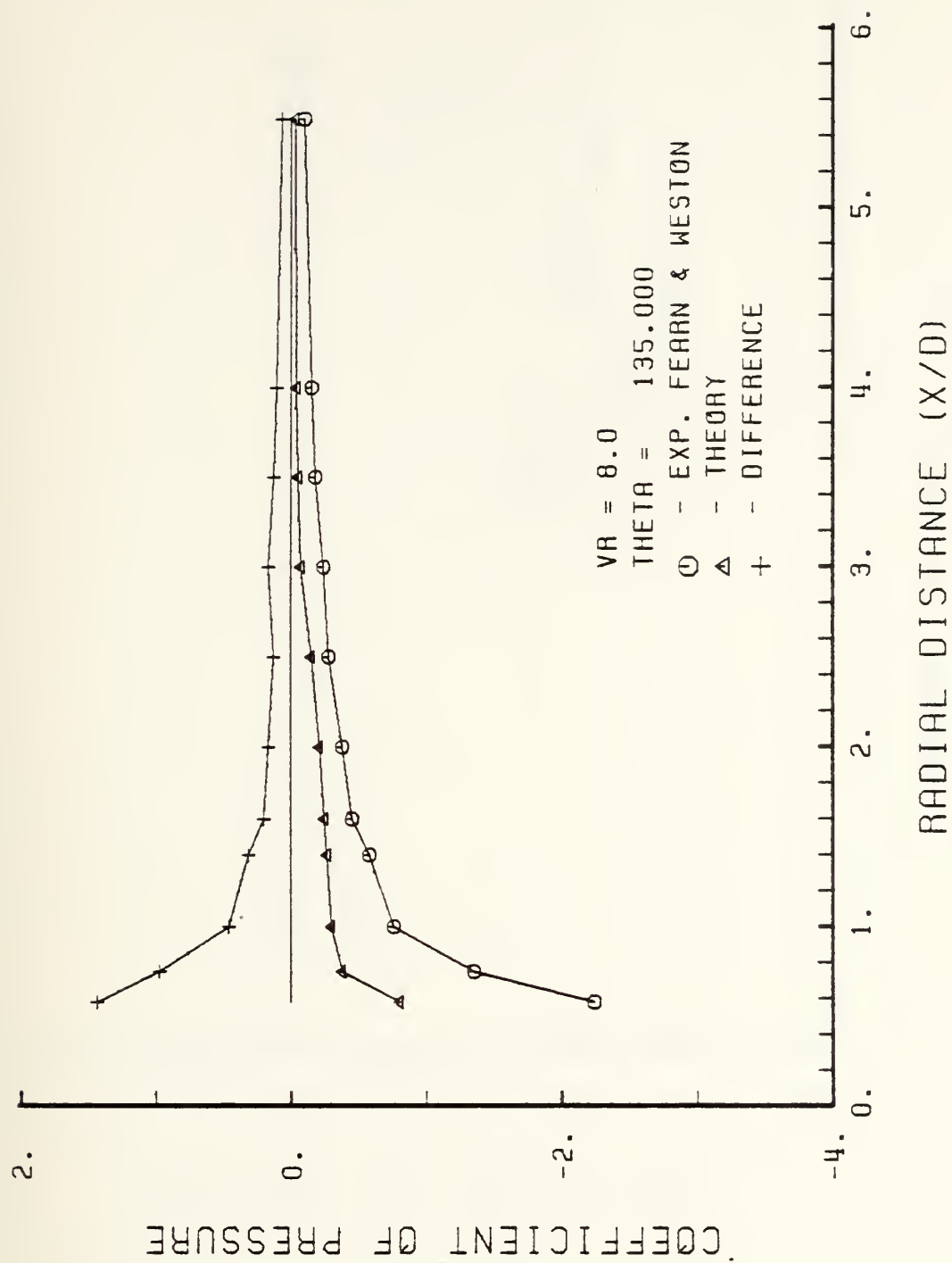


Figure C-11.  $C_p$ 's along radial lines, VR = 8, theta = 135 degrees.



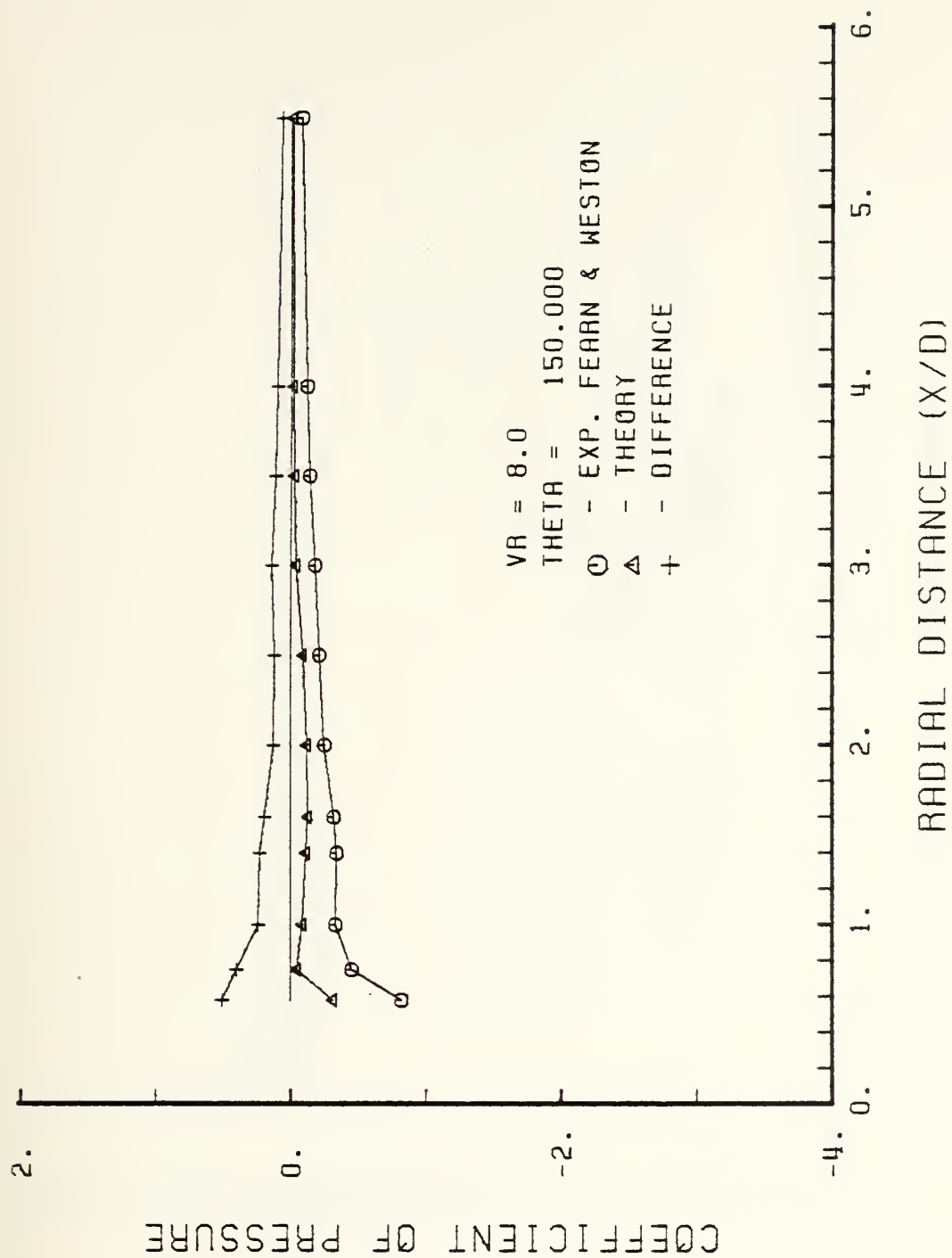


Figure C-12.  $C_p$ 's along radial lines, VR = 8, theta = 150 degrees.



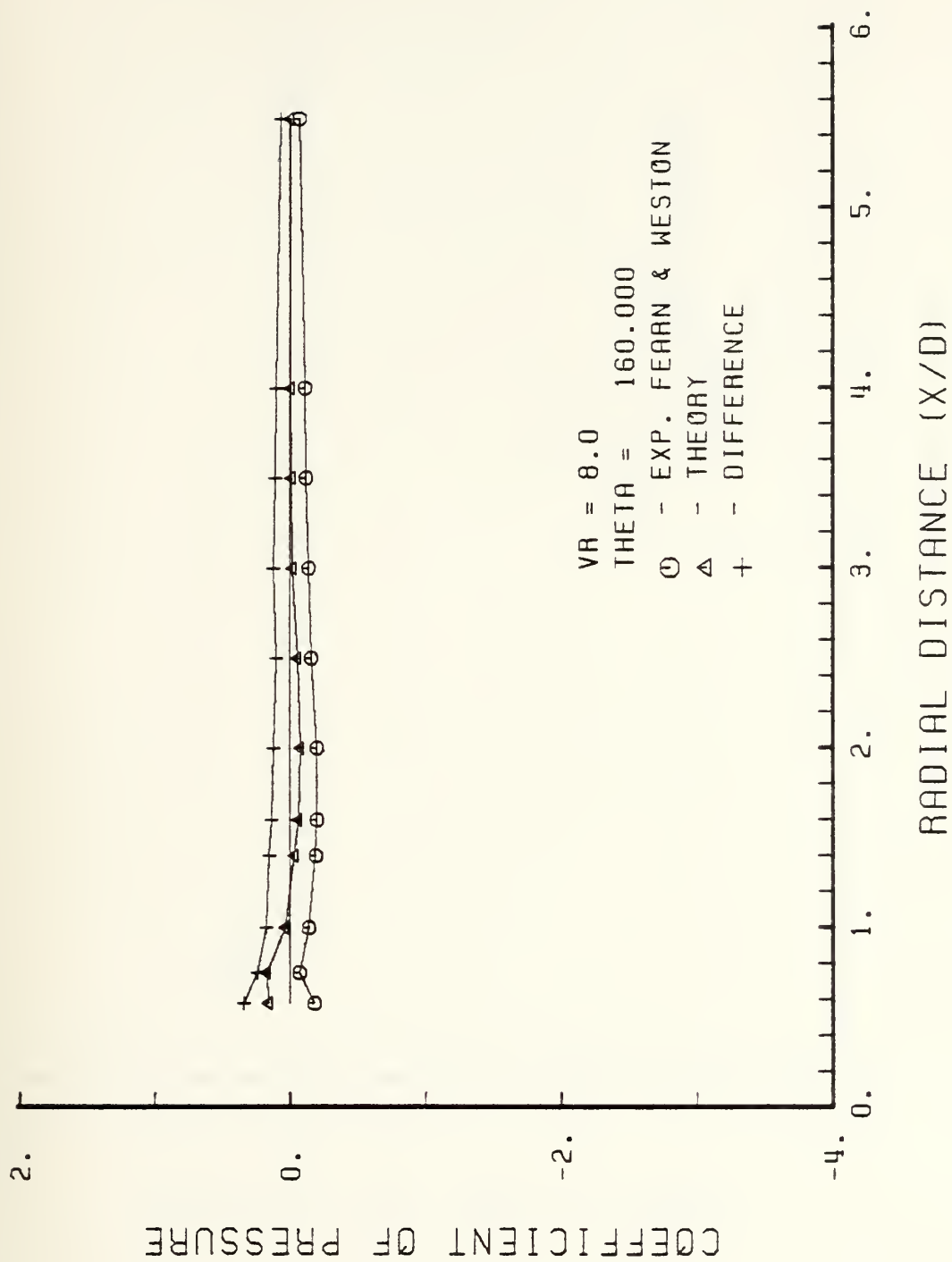


Figure C-13.  $C_p$ 's along radial lines, VR = 8, theta = 160 degrees.





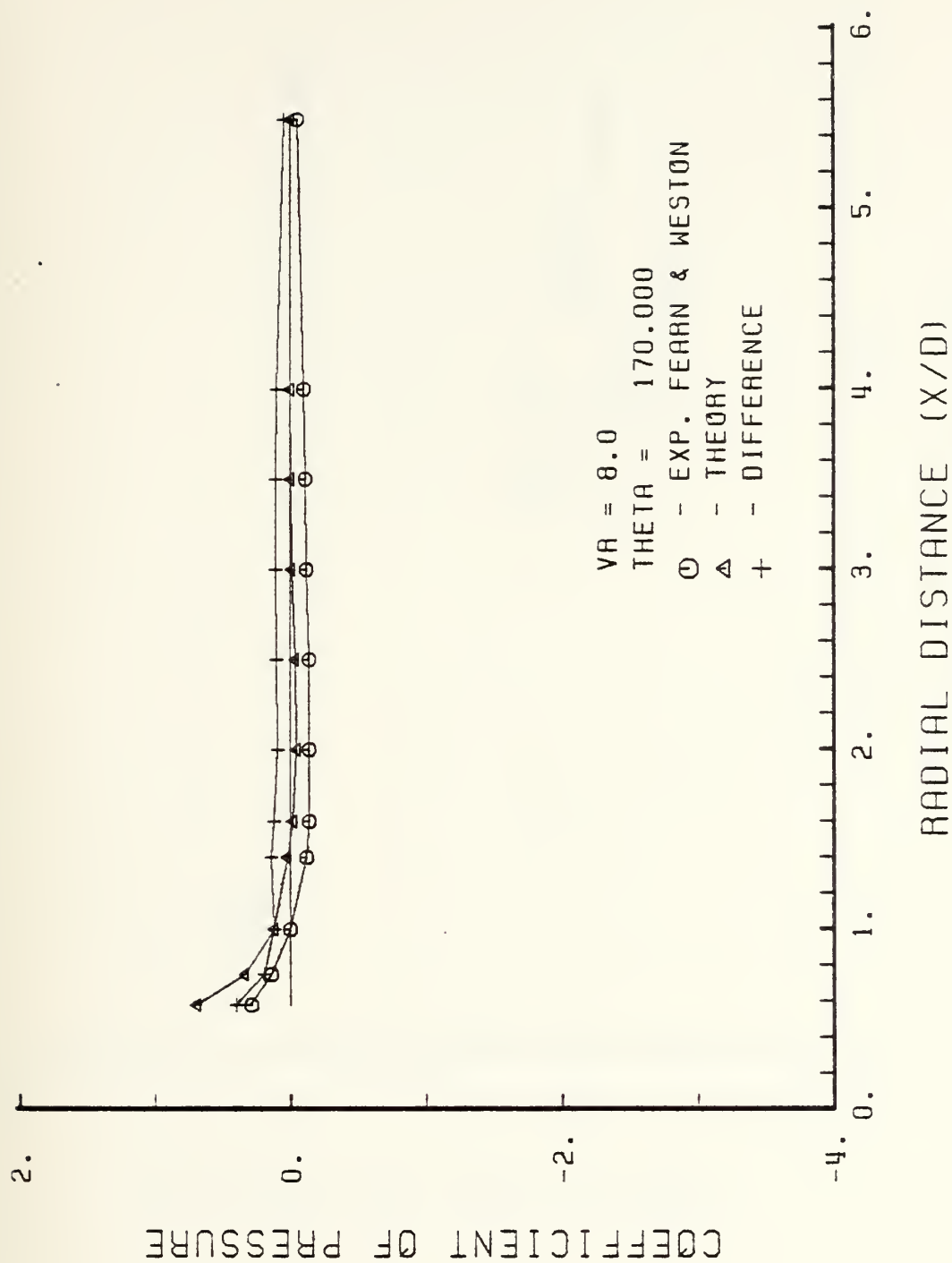


Figure C-14.  $C_p$ 's along radial lines,  $VR = 8$ ,  $\theta = 170$  degrees.



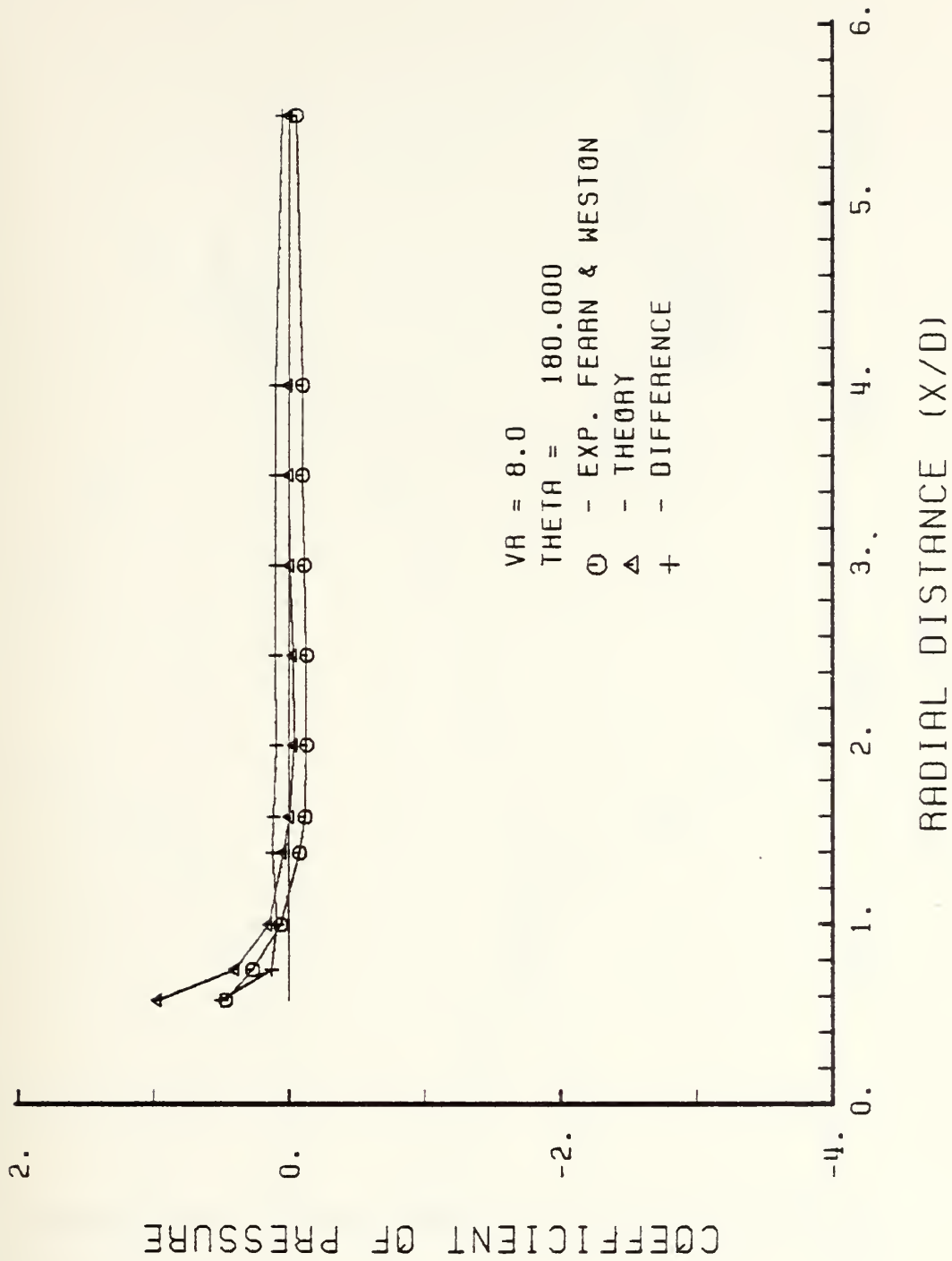


Figure C-15.  $C_p$ 's along radial lines, VR = 8, theta = 180 degrees.



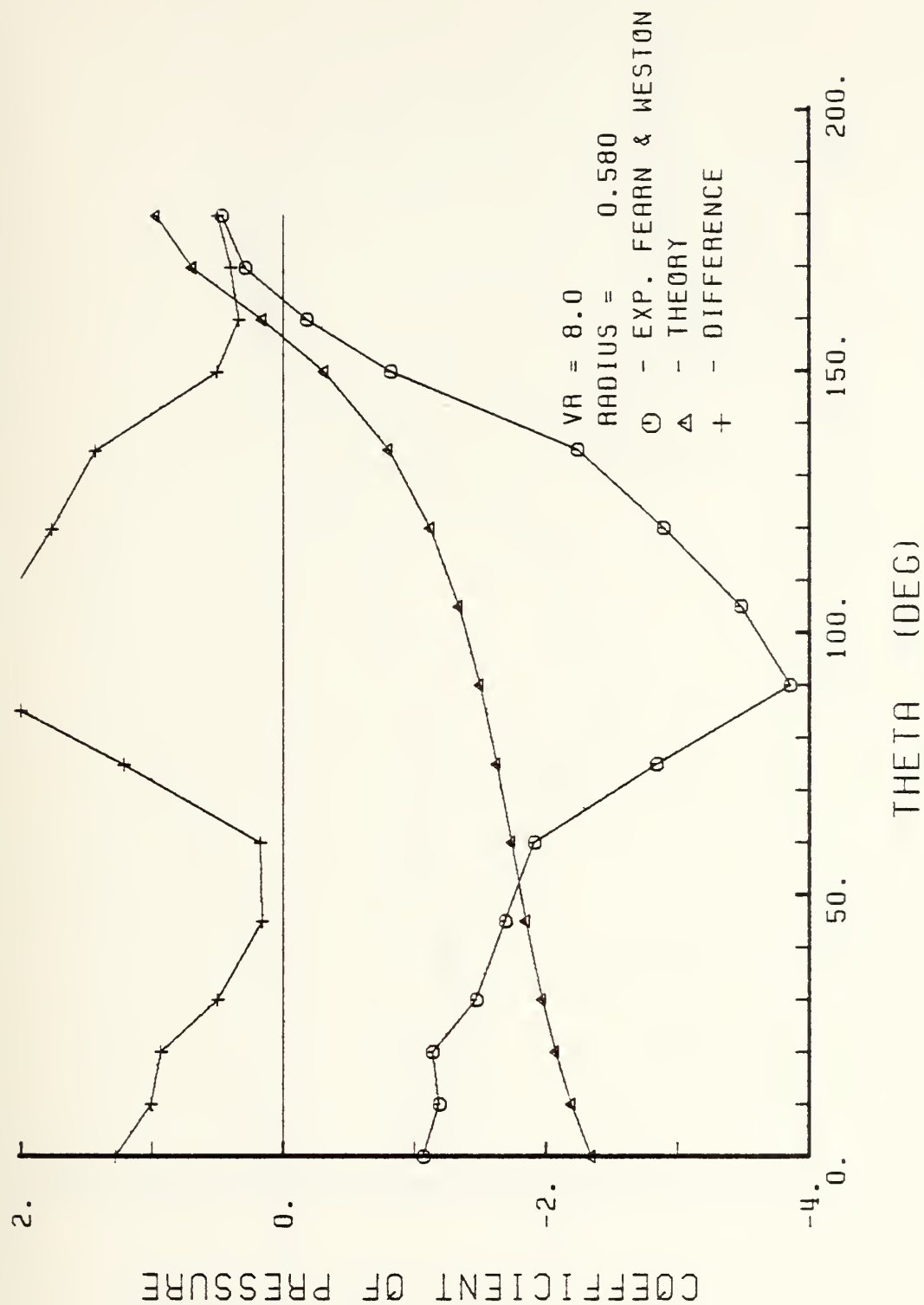


Figure C-16.  $C_p$ 's along circumferential arcs, VR = 8, radius = .58 dia.



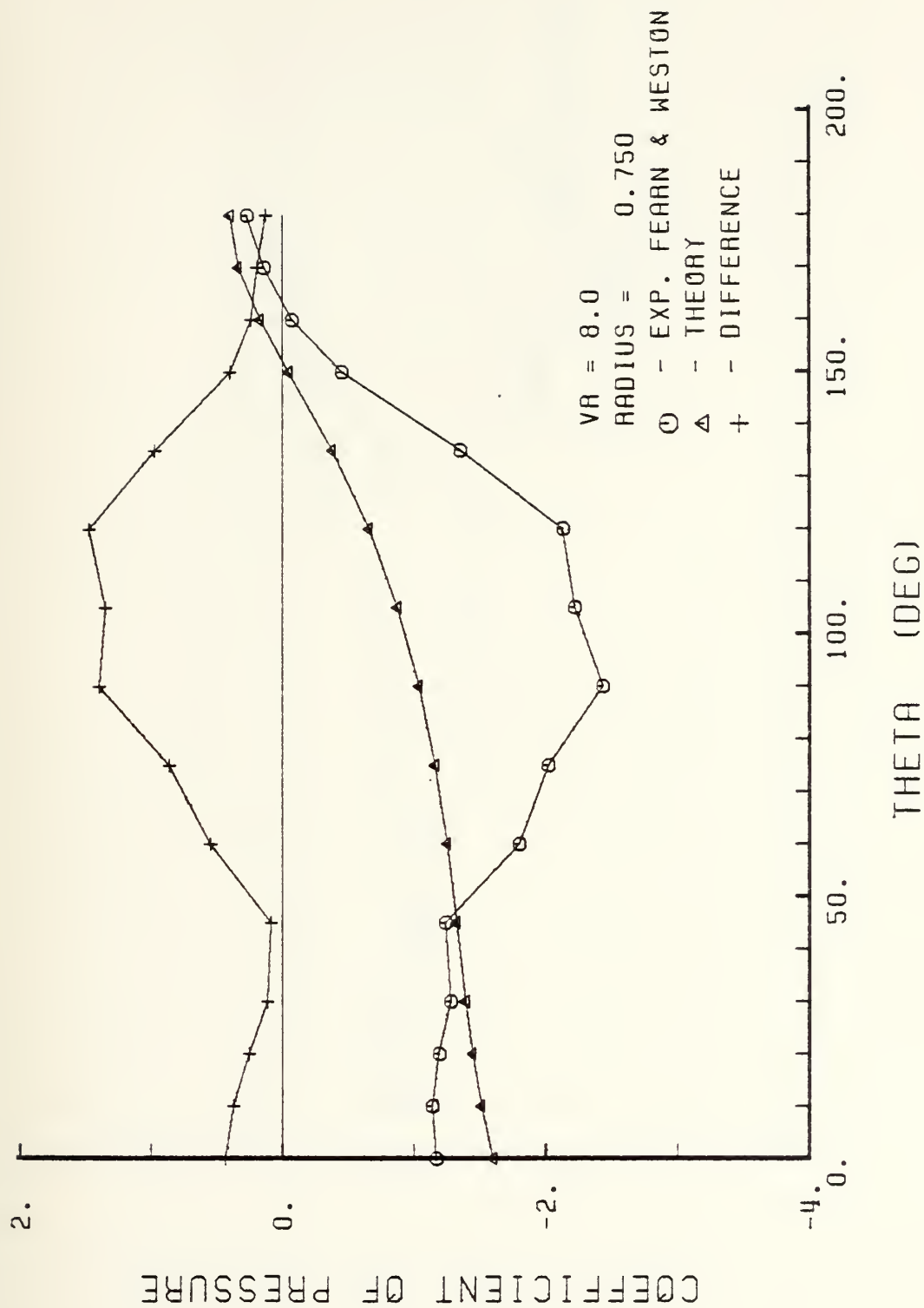


Figure C-17.  $C_p$ 's along circumferential arcs, VR = 8, radius = .75 dia.





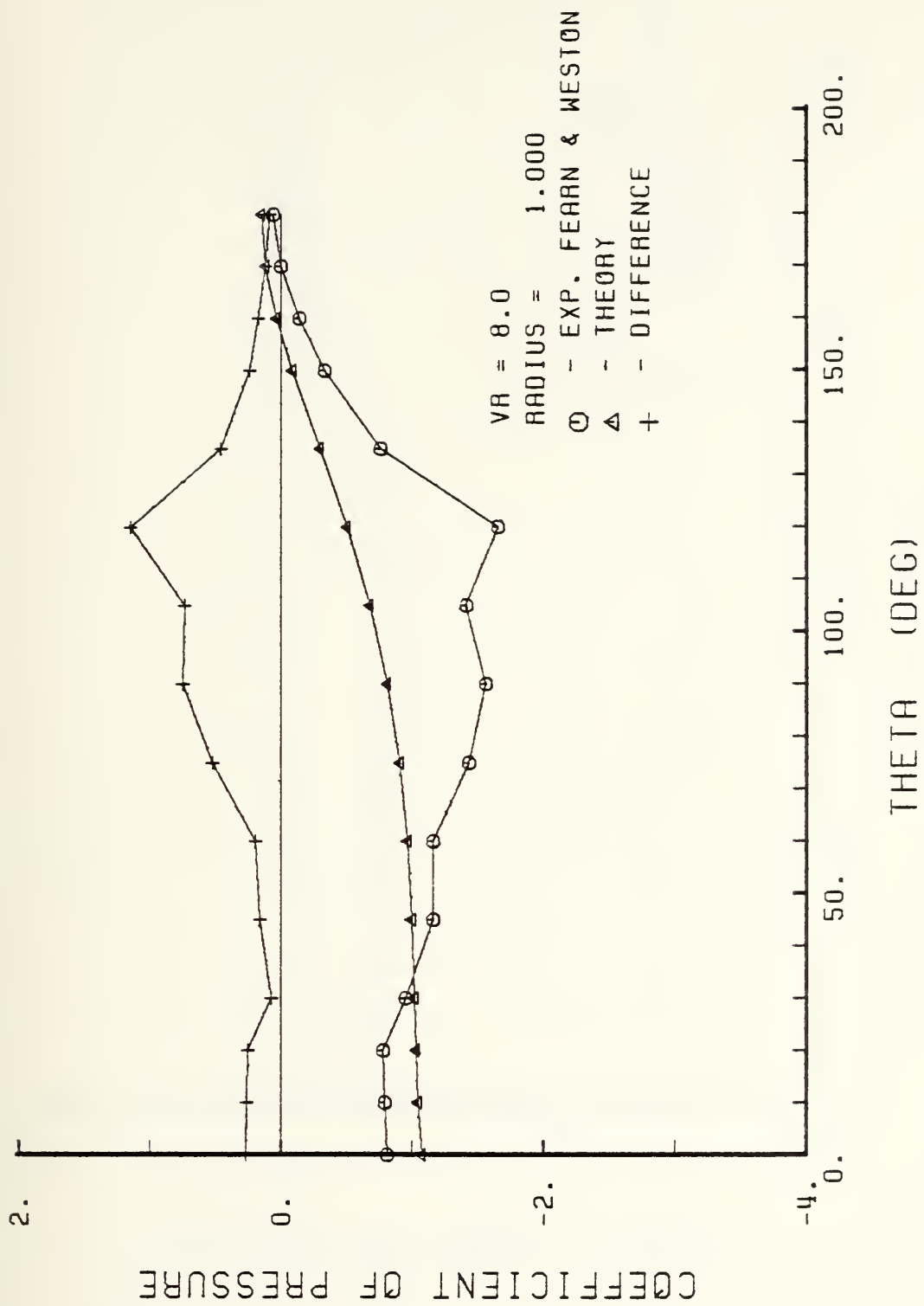


Figure C-18.  $C_p$ 's along circumferential arcs, VR = 8, radius = 1 dia.



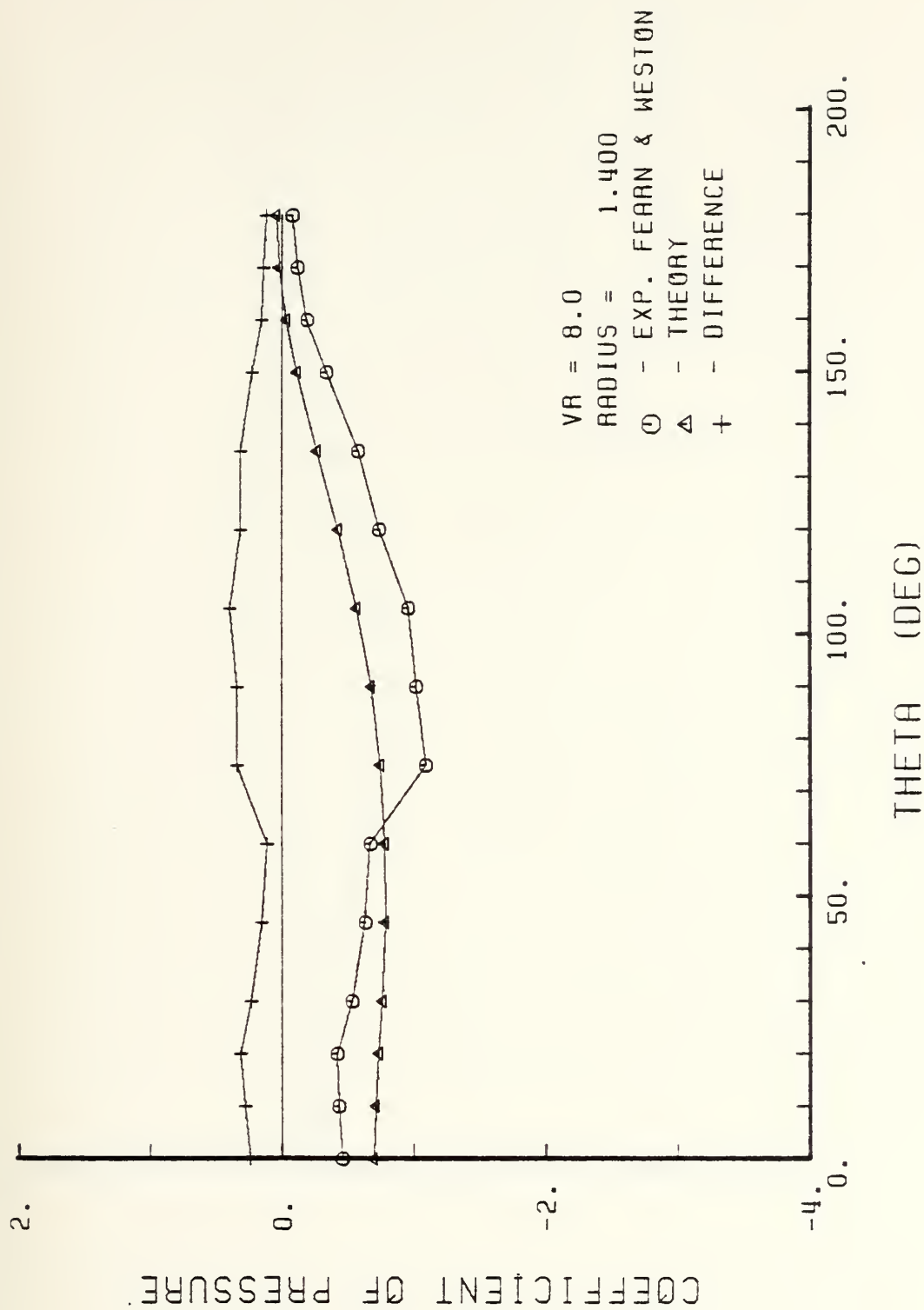


Figure C-19.  $C_p$ 's along circumferential arcs, VR = 8, radius = 1.4 dia.



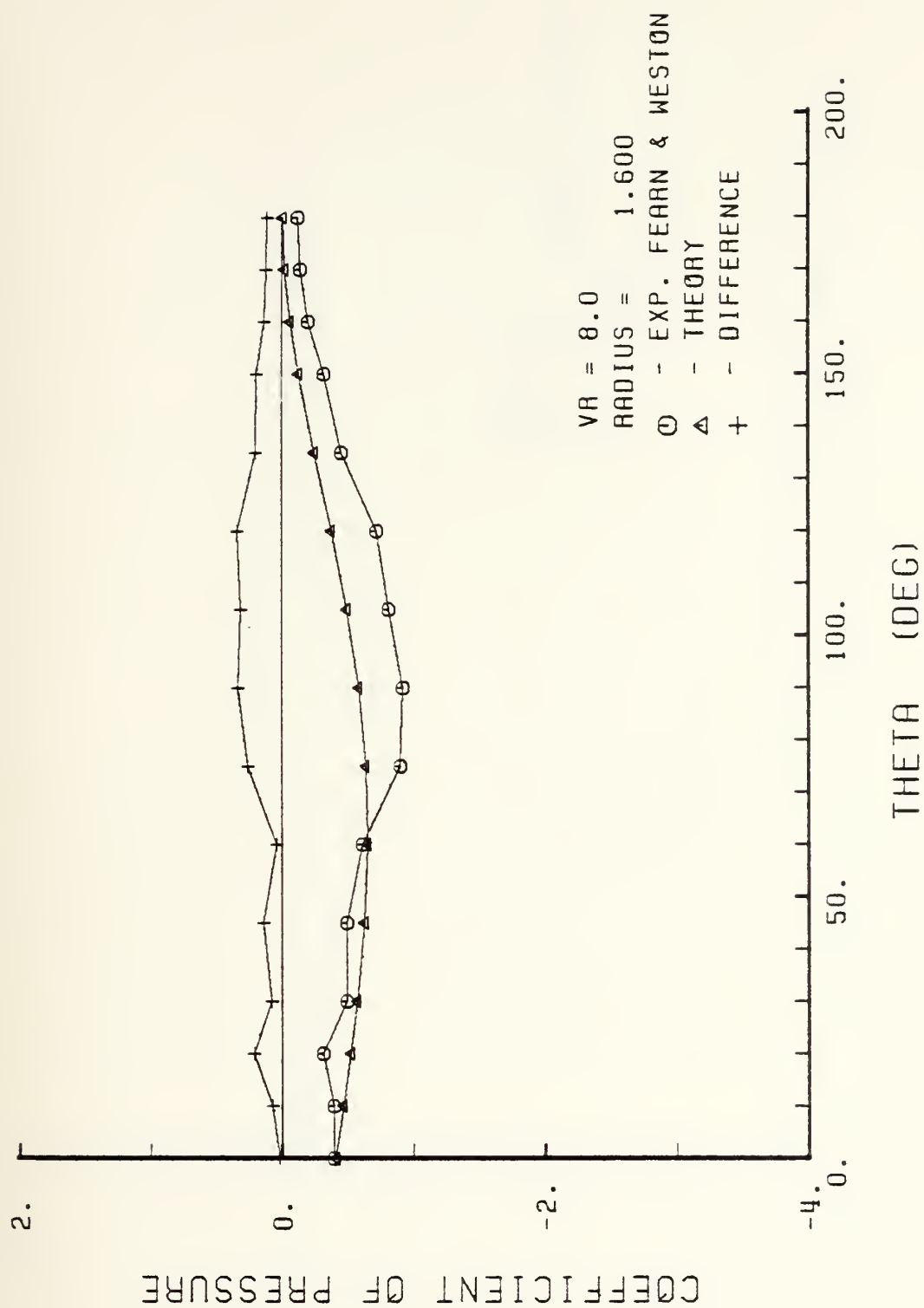


Figure C-20.  $C_p$ 's along circumferential arcs, VR = 8, radius = 1.6 dia.



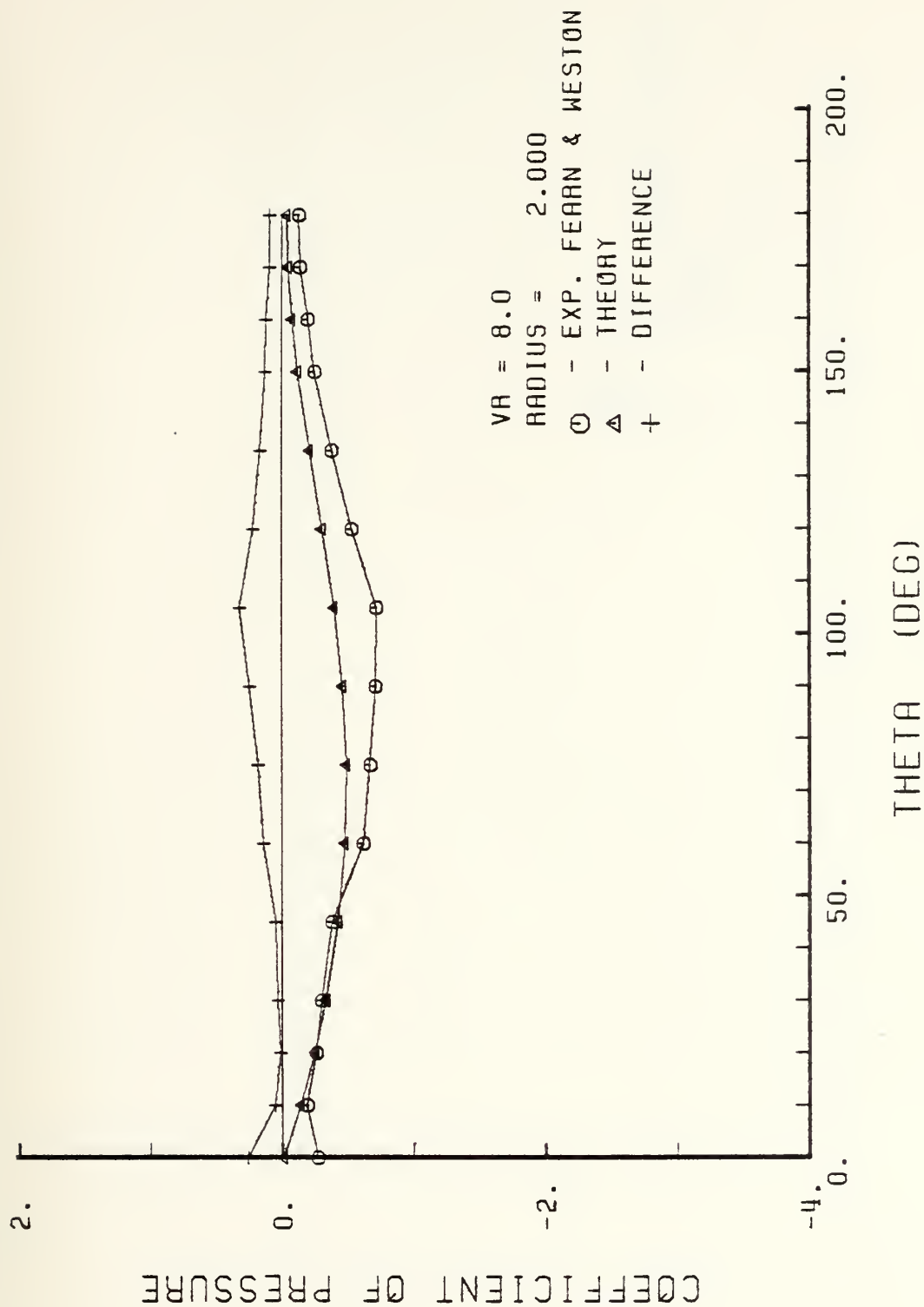


Figure C-21.  $C_p$ 's along circumferential arcs, VR = 8, radius = 2 dia.





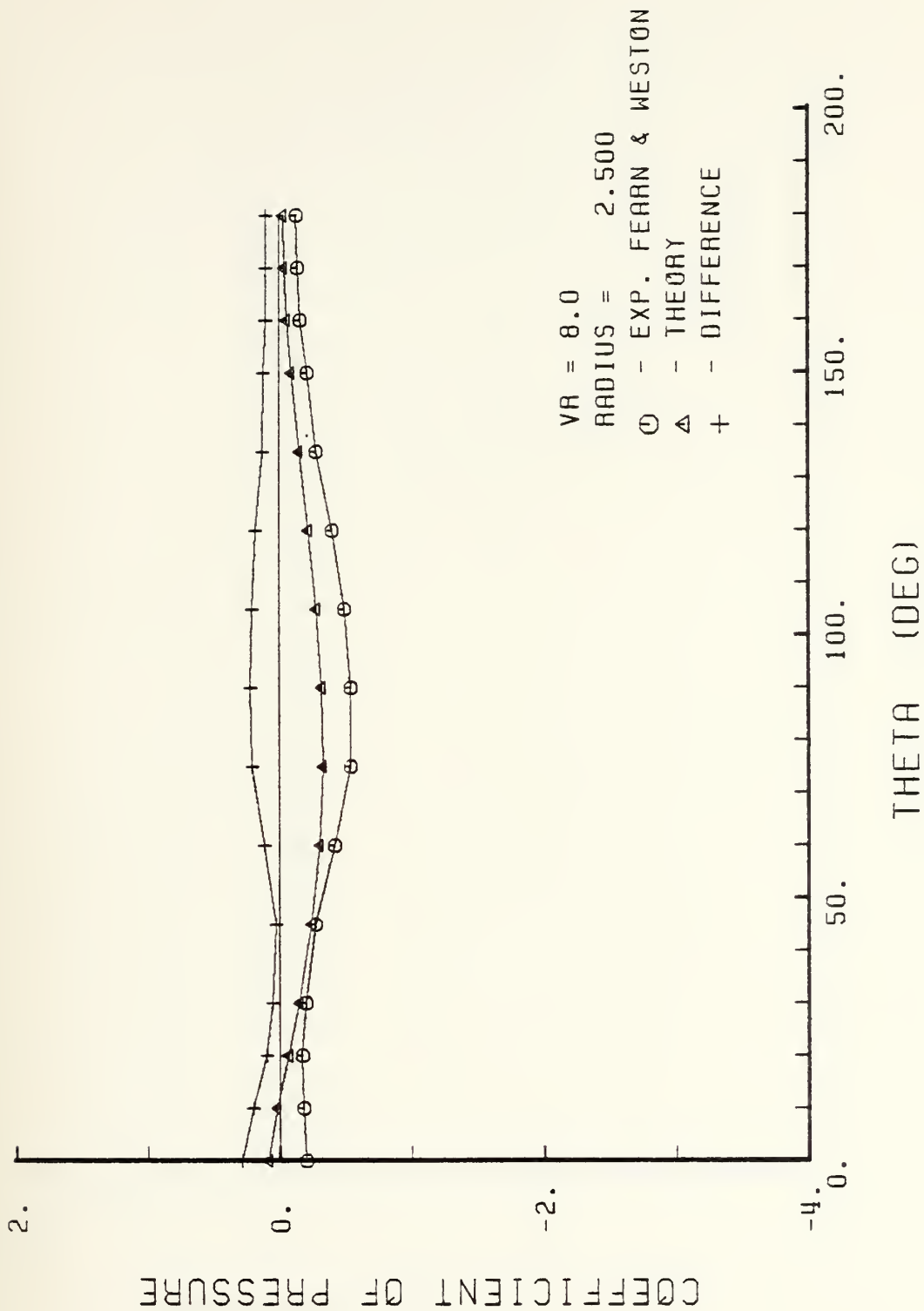


Figure C-22.  $C_p$ 's along circumferential arcs, VR = 8, radius = 2.5 dia.



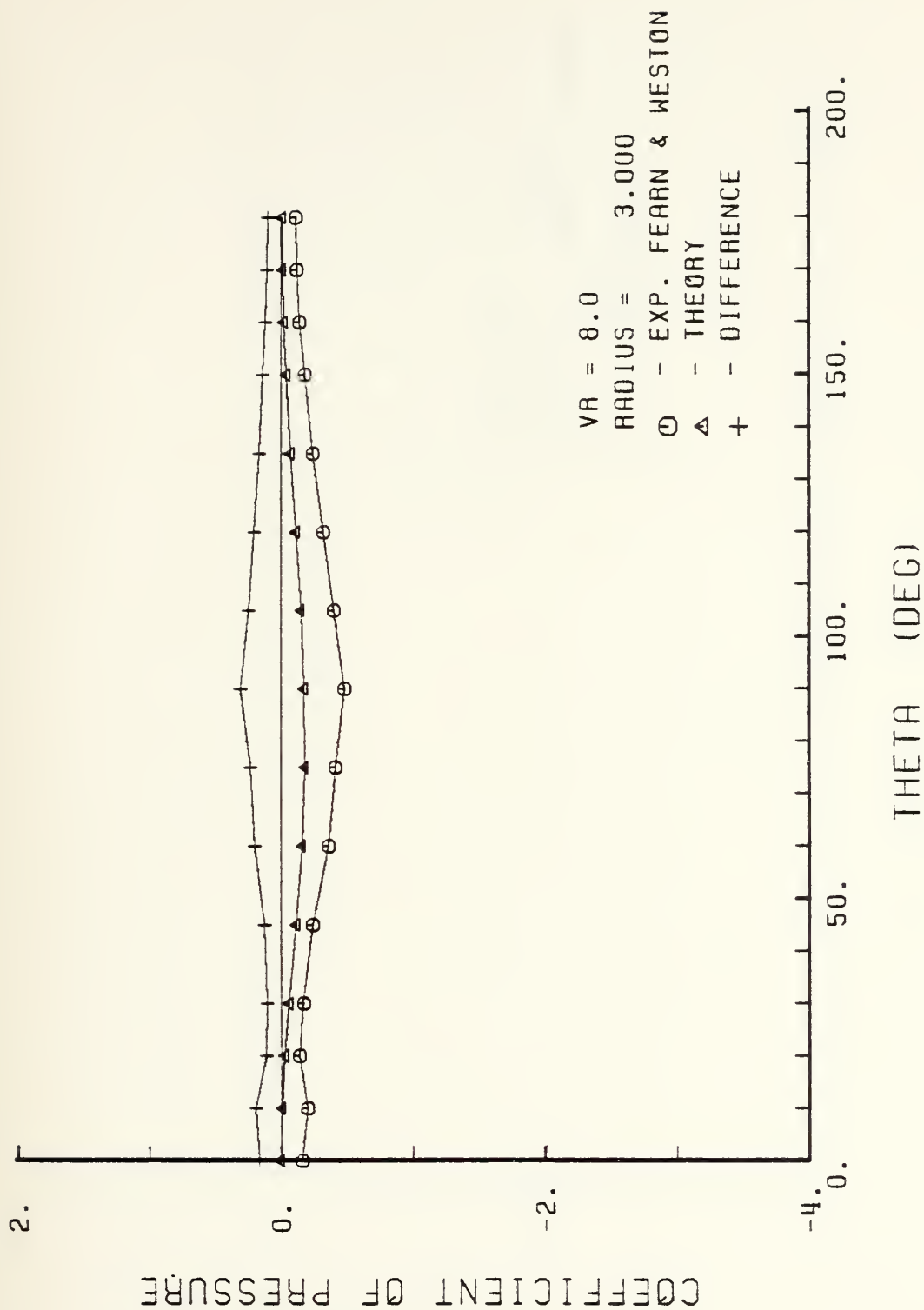


Figure C-23.  $C_p$ 's along circumferential arcs,  $VR = 8$ , radius = 3 dia.



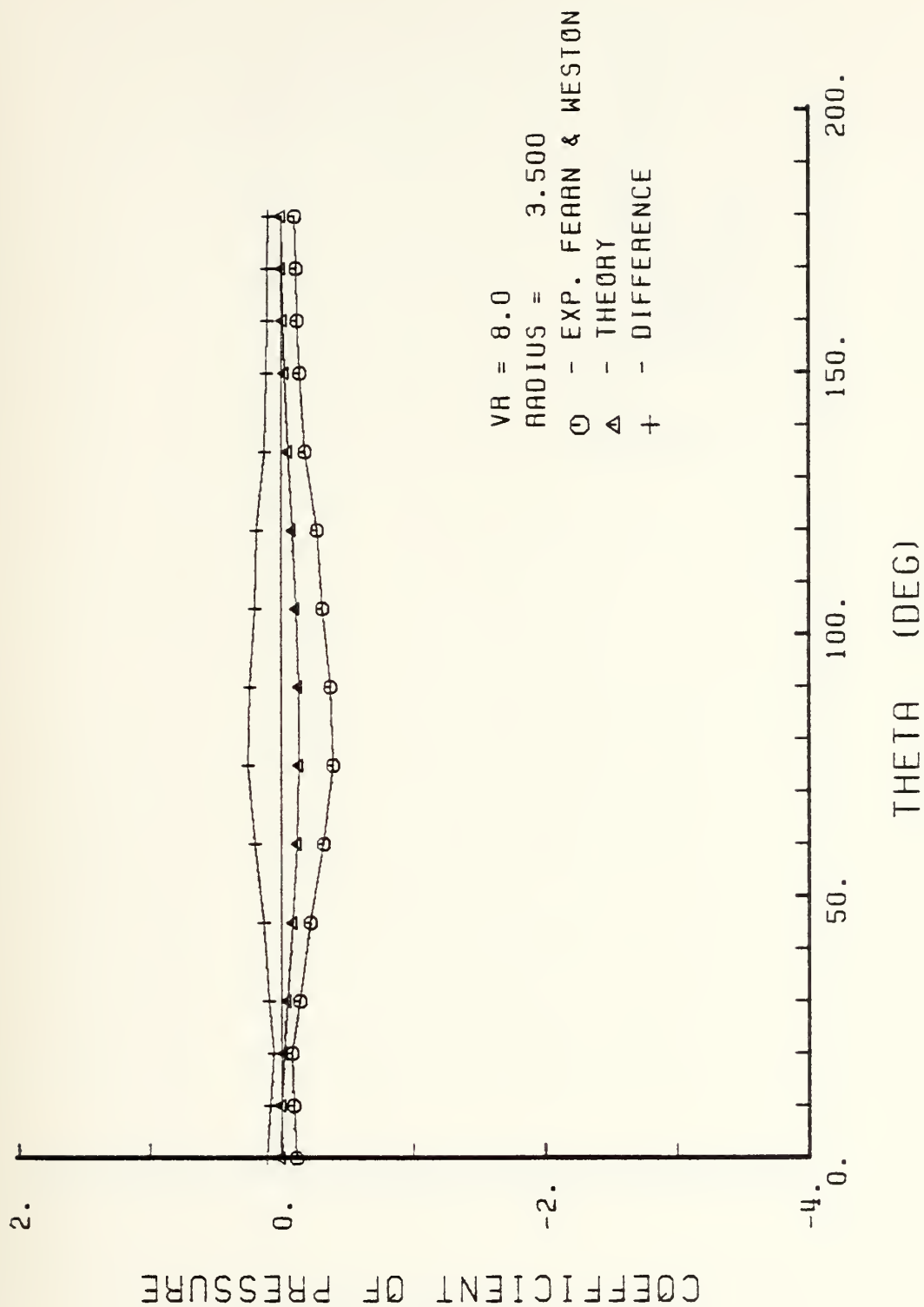


Figure C-24.  $C_p$ 's along circumferential arcs, VR = 8, radius 3.5 dia.



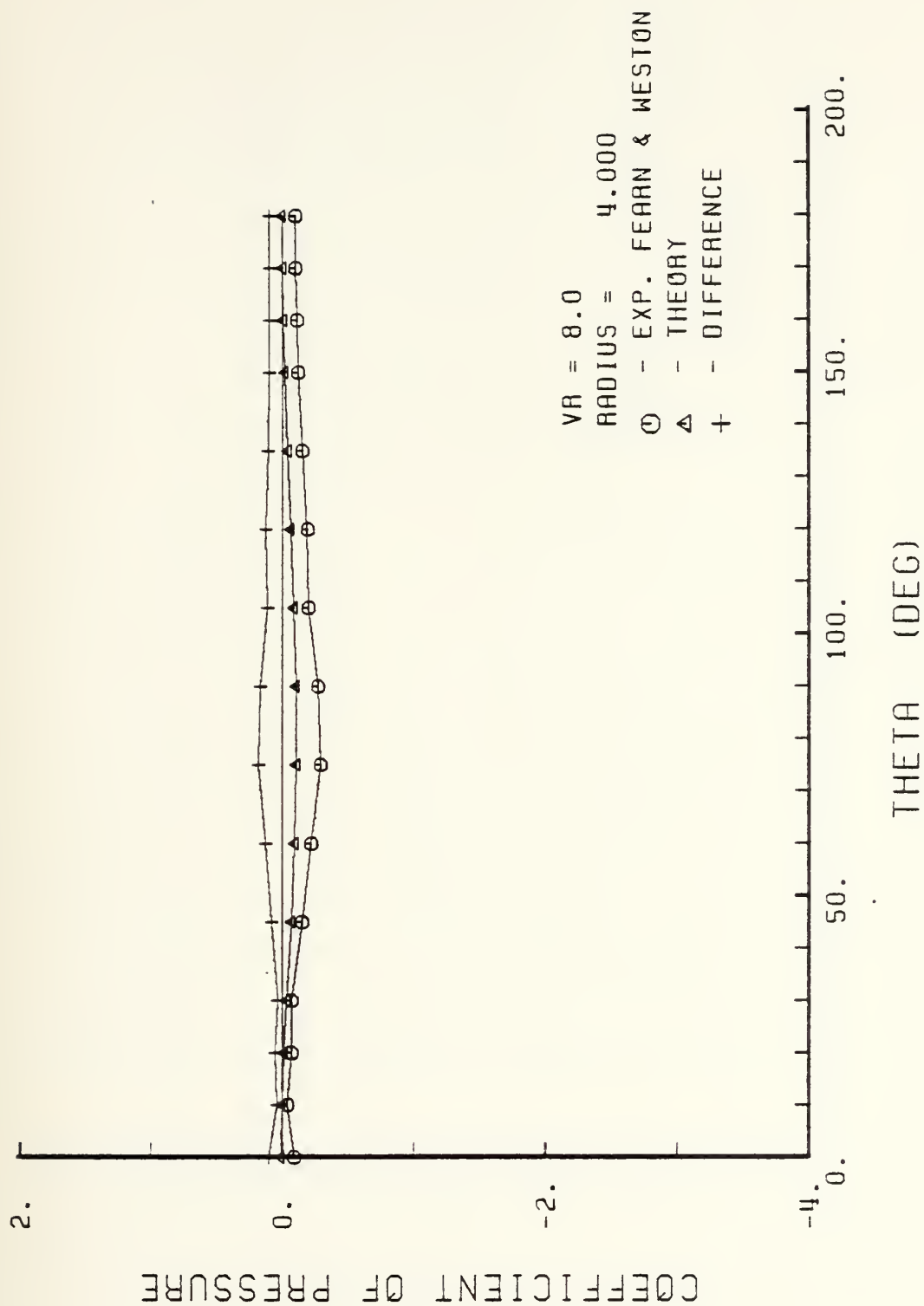


Figure C-25.  $C_p$ 's along circumferential arcs, VR = 8, radius = 4 dia.





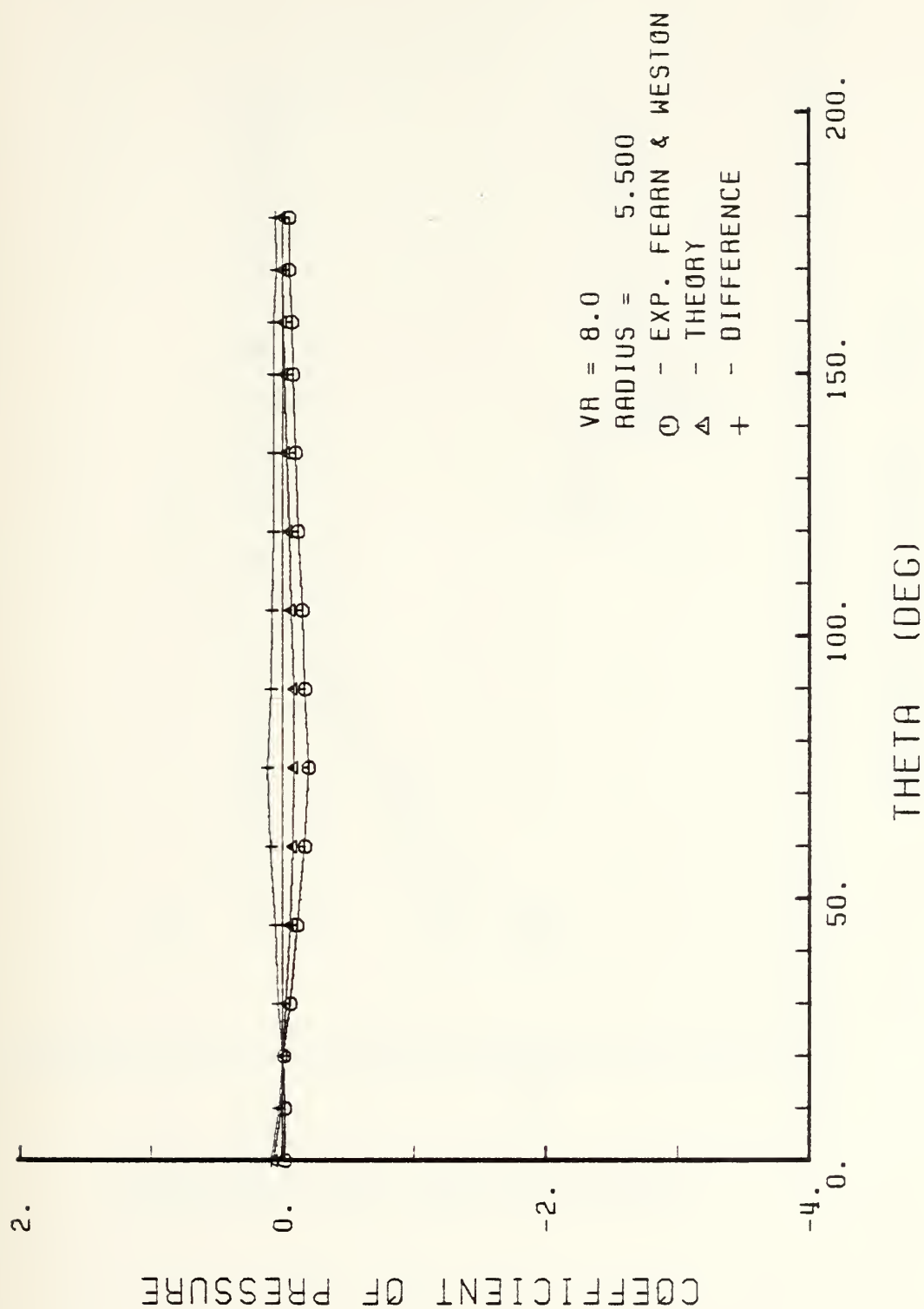


Figure C-26.  $C_p$ 's along circumferential arcs, VR = 8, radius = 5.5 dia.



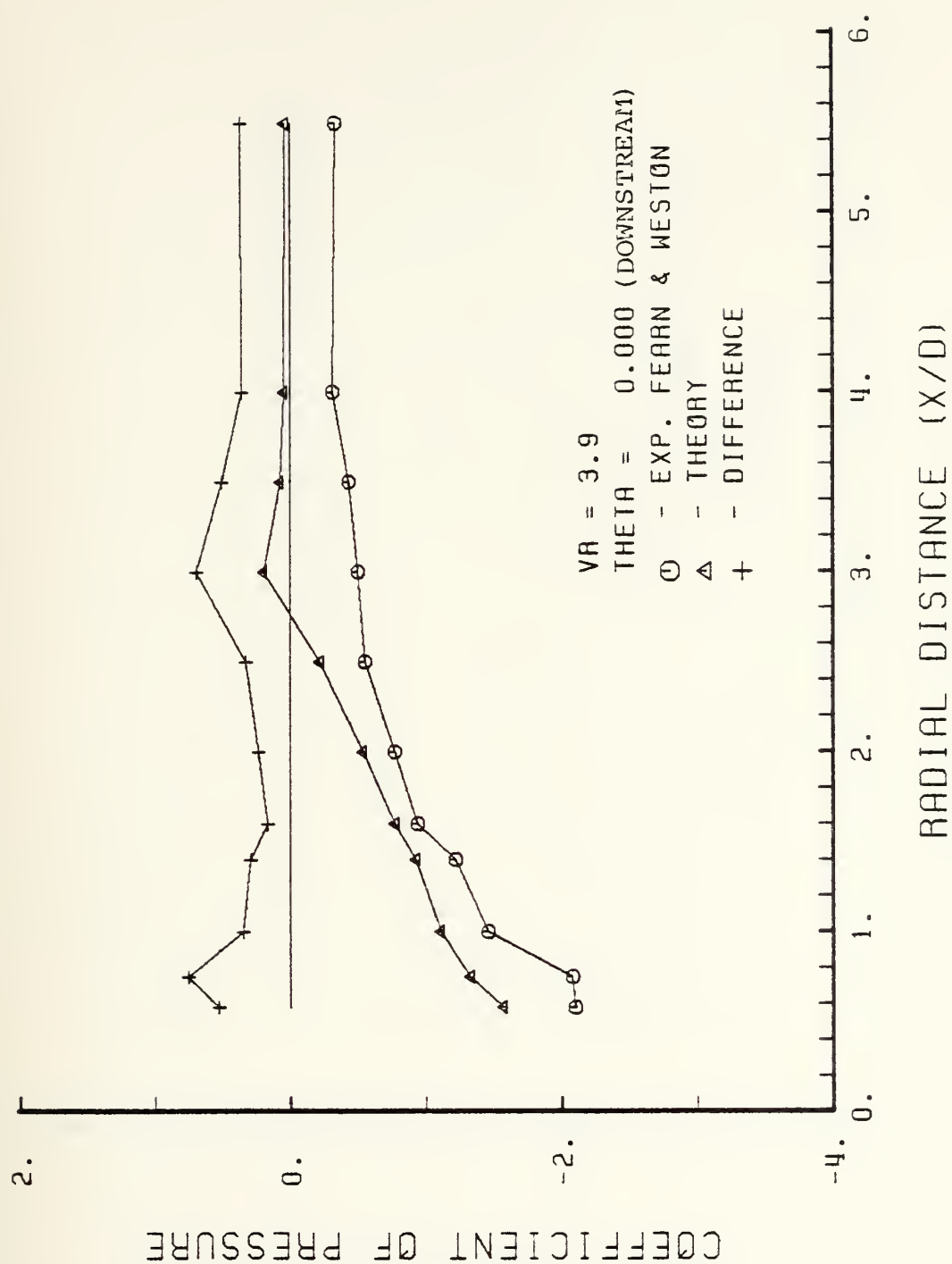


Figure C-27.  $C_p$ 's along radial lines, VR = 3.9, theta = 0 degrees.



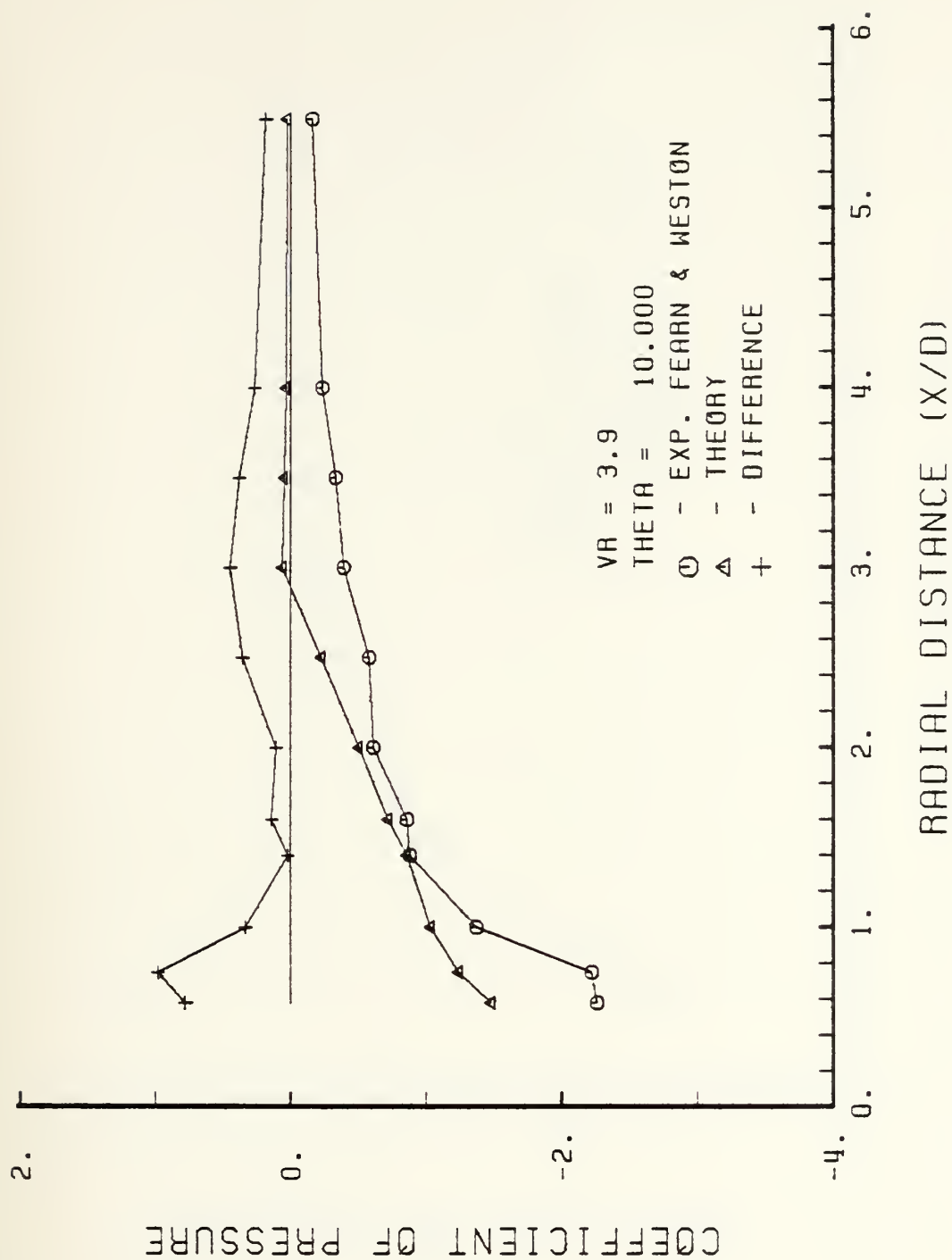


Figure C-28.  $C_p$ 's along radial lines, VR = 3.9, theta = 10 degrees.



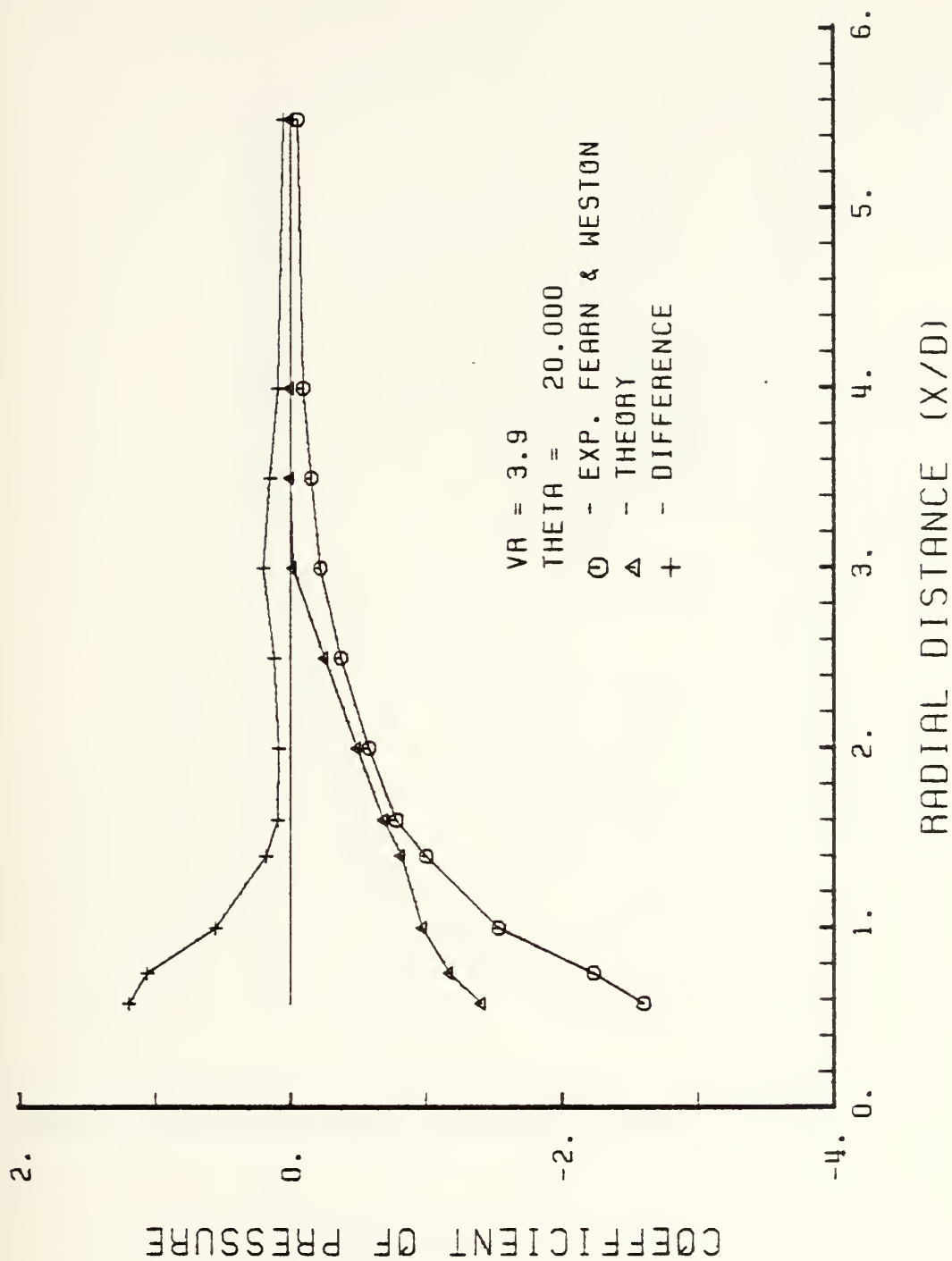


Figure C-29.  $C_p$ 's along radial lines, VR = 3.9, theta = 20 degrees.





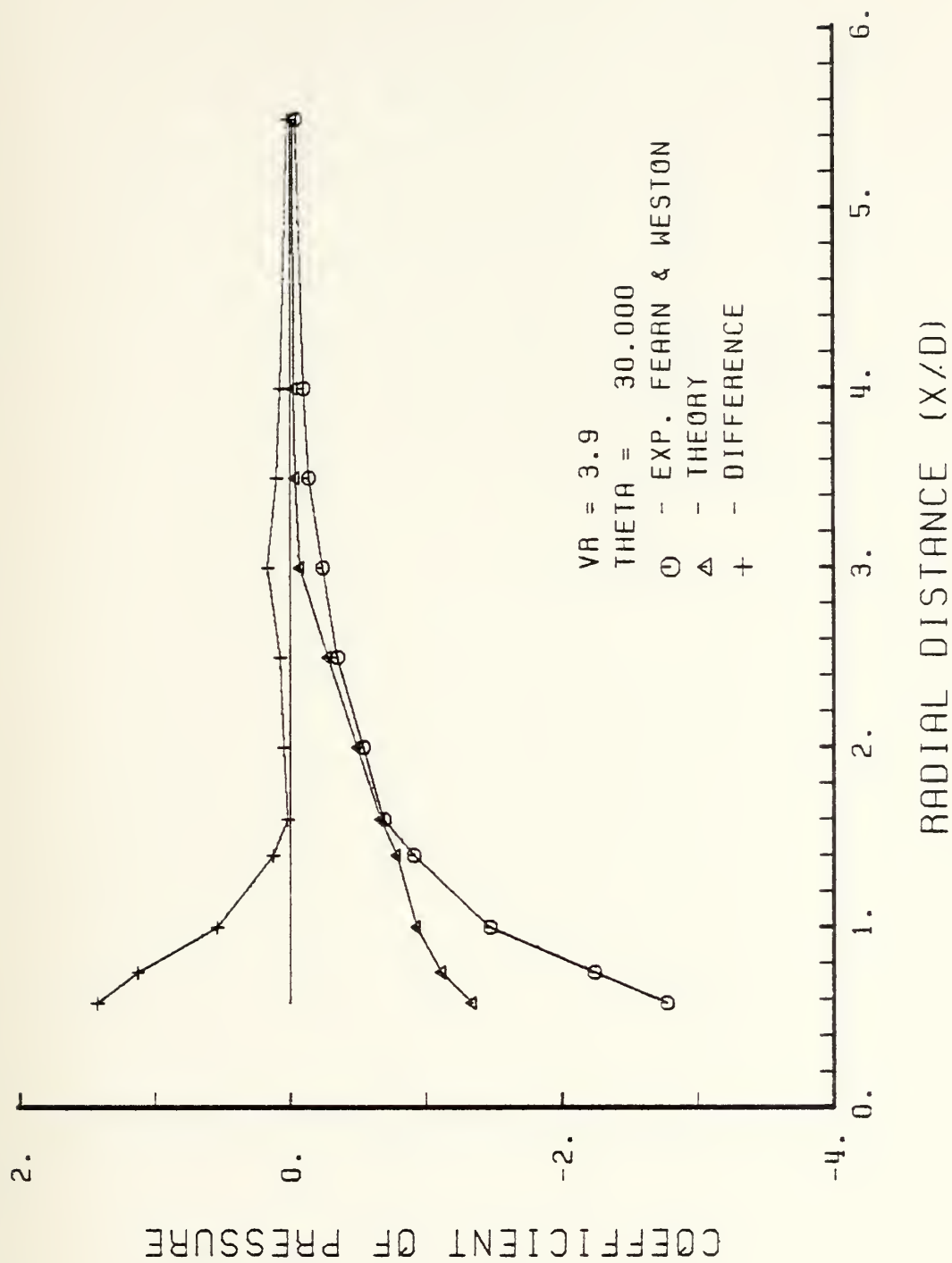


Figure C-30.  $C_p$ 's along radial lines,  $VR = 3.9$ ,  $\theta = 30$  degrees.



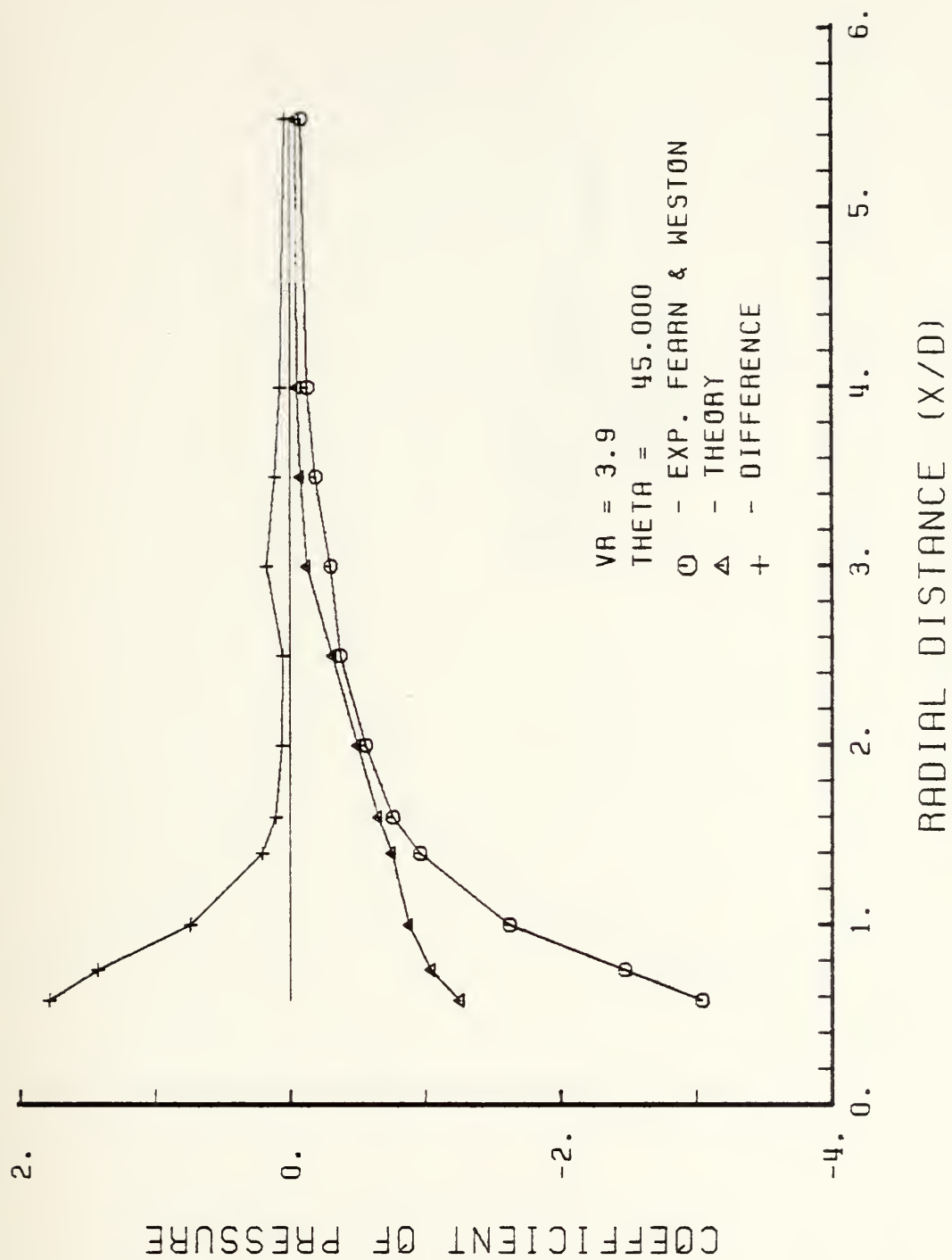


Figure C-31.  $C_p$ 's along radial lines, VR = 3.9, theta = 45 degrees.



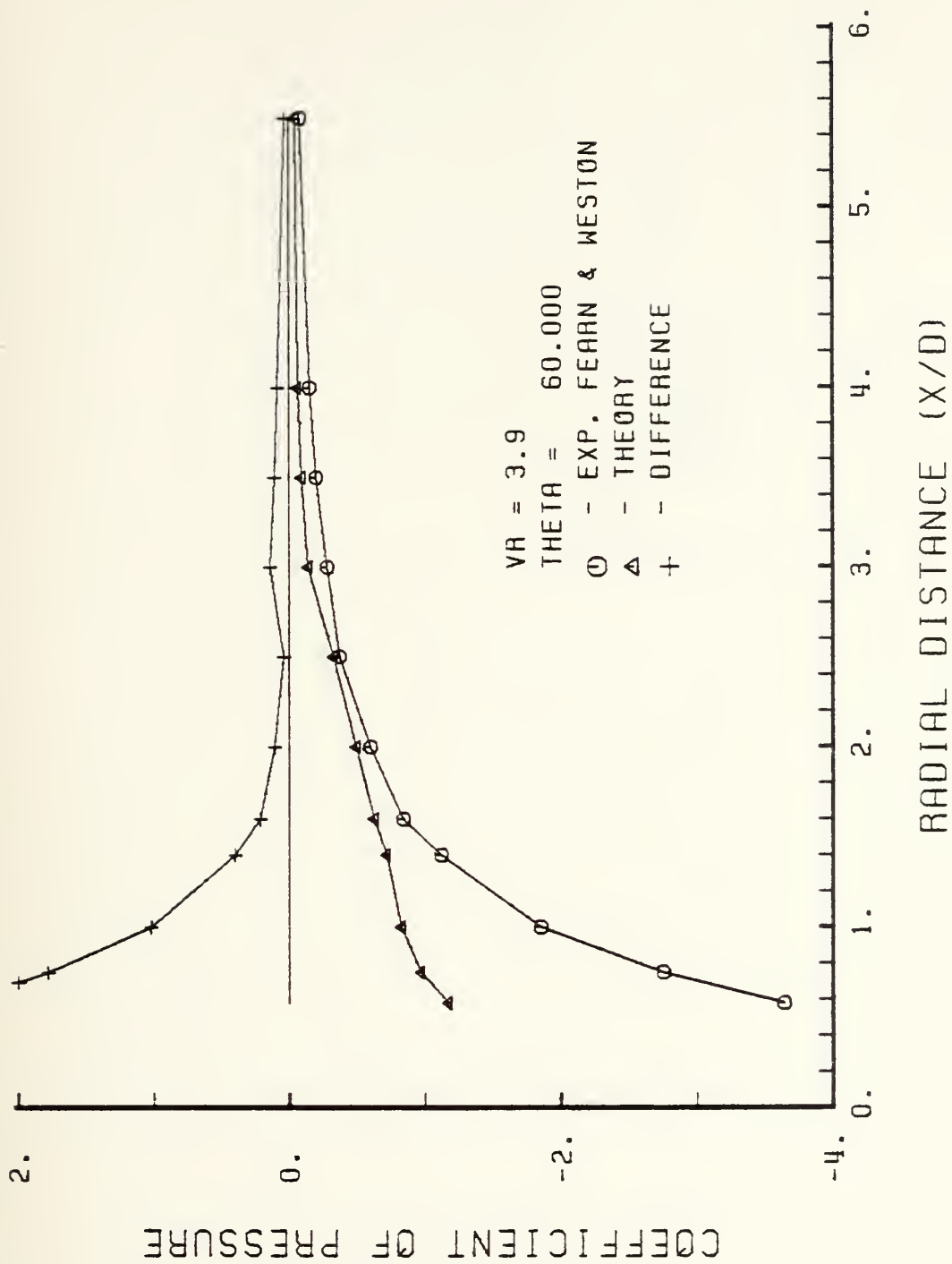


Figure C-32.  $C_p$ 's along radial lines, VR = 3.9, theta = 60 degrees.



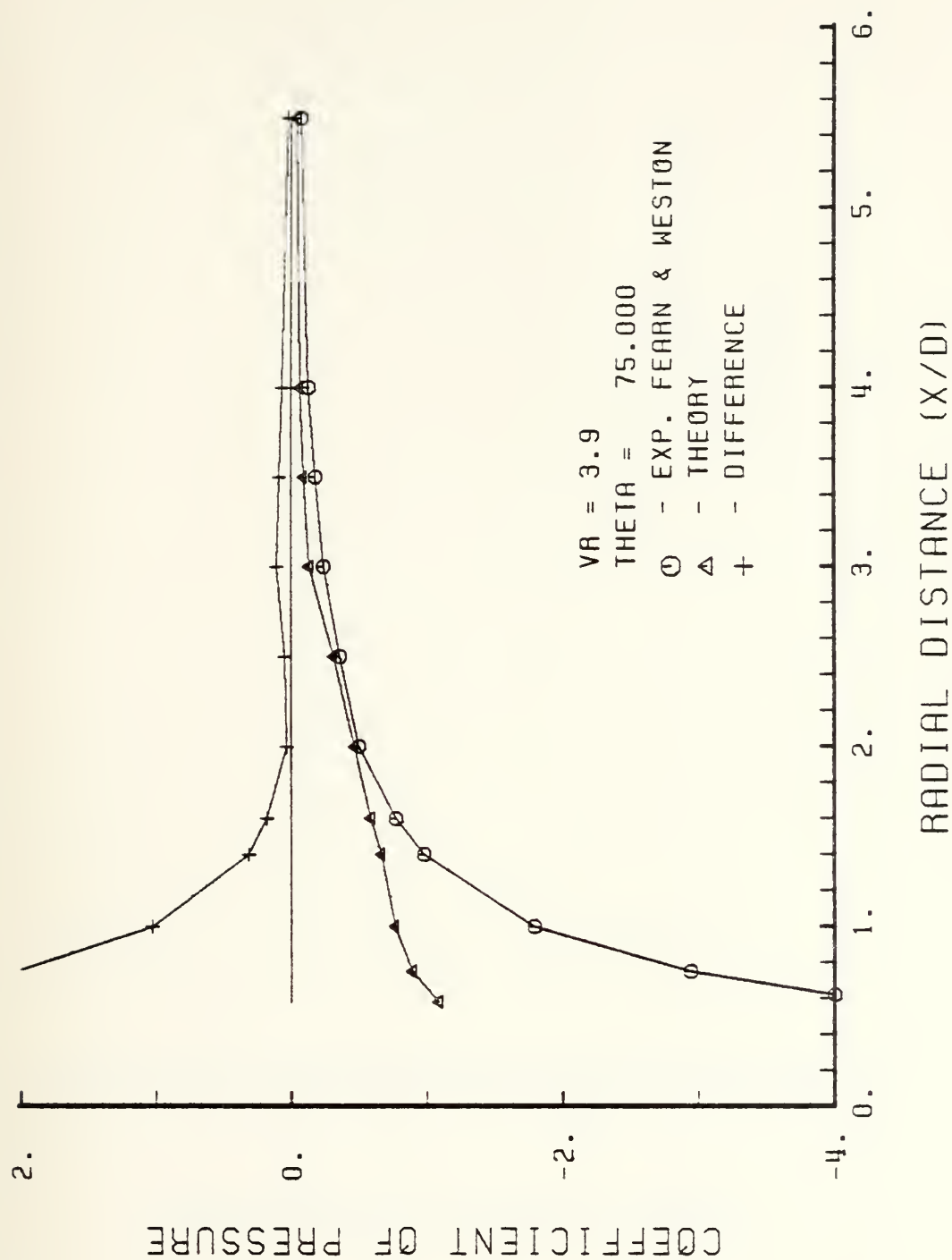


Figure C-33.  $C_p$ 's along radial lines,  $VR = 3.9$ ,  $\theta = 75$  degrees.





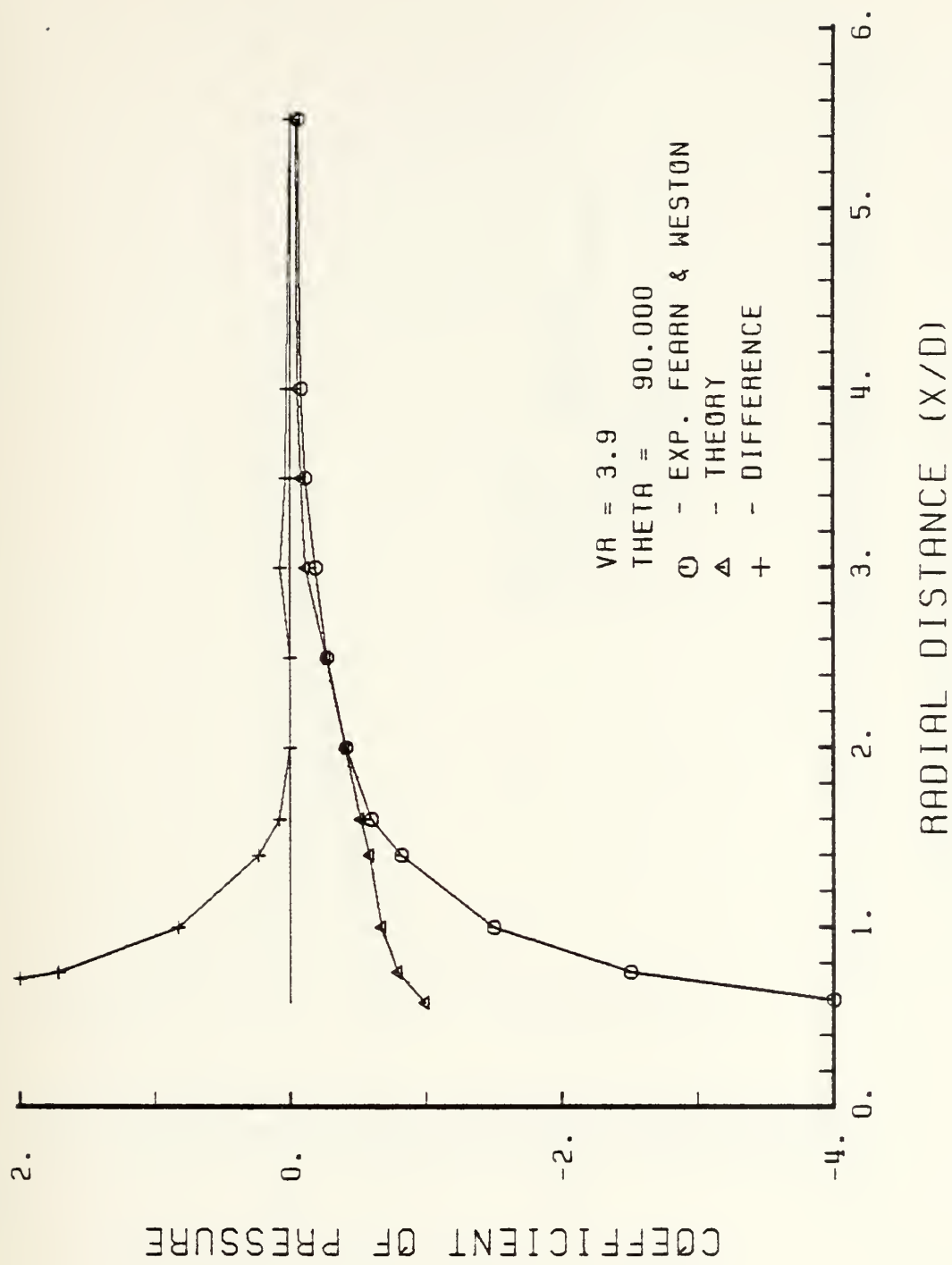


Figure C-34.  $C_p$ 's along radial lines, VR = 3.9, theta = 90 degrees.



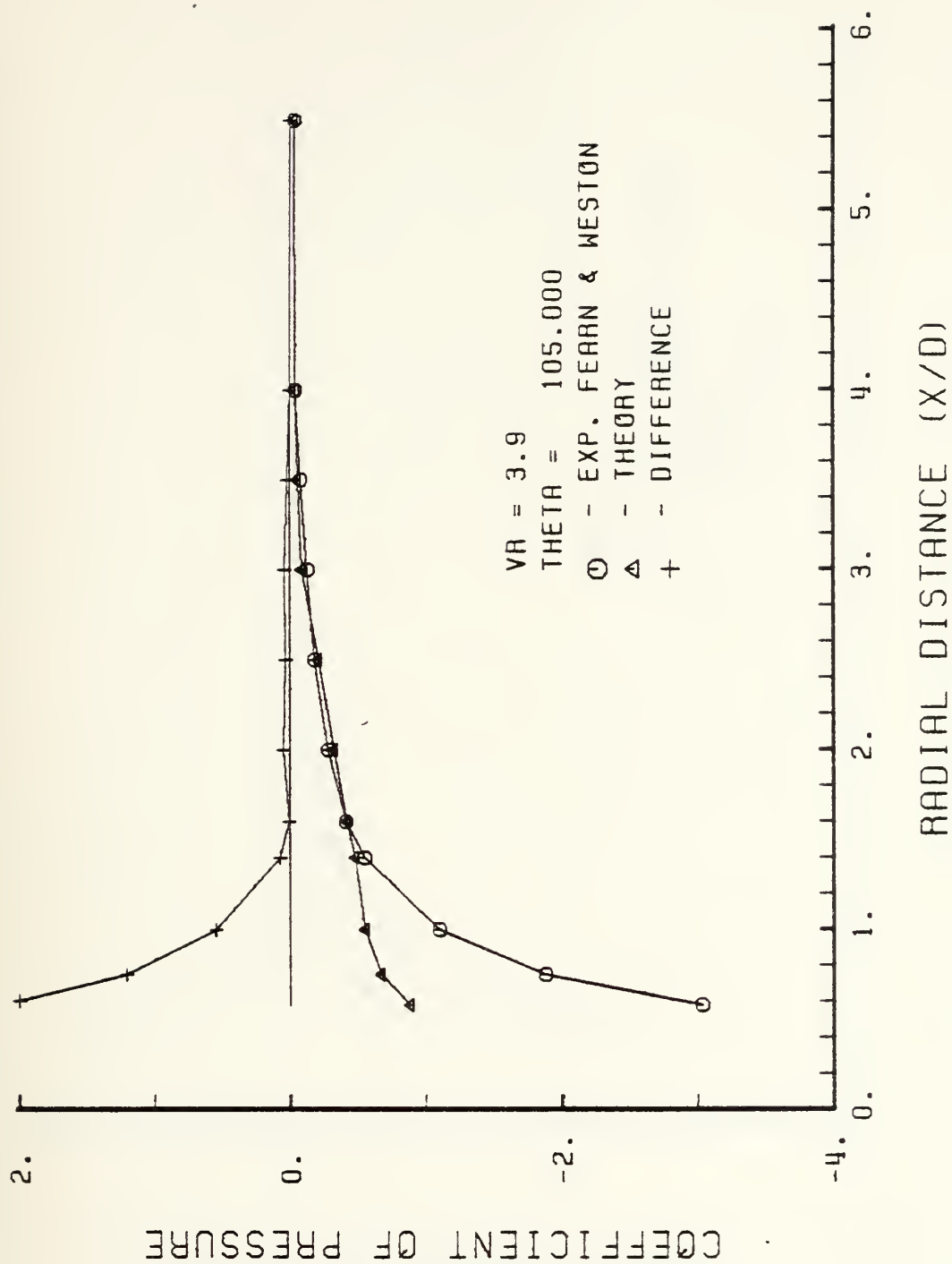


Figure C-35.  $C_p$ 's along radial lines, VR = 3.9, theta = 105 degrees.



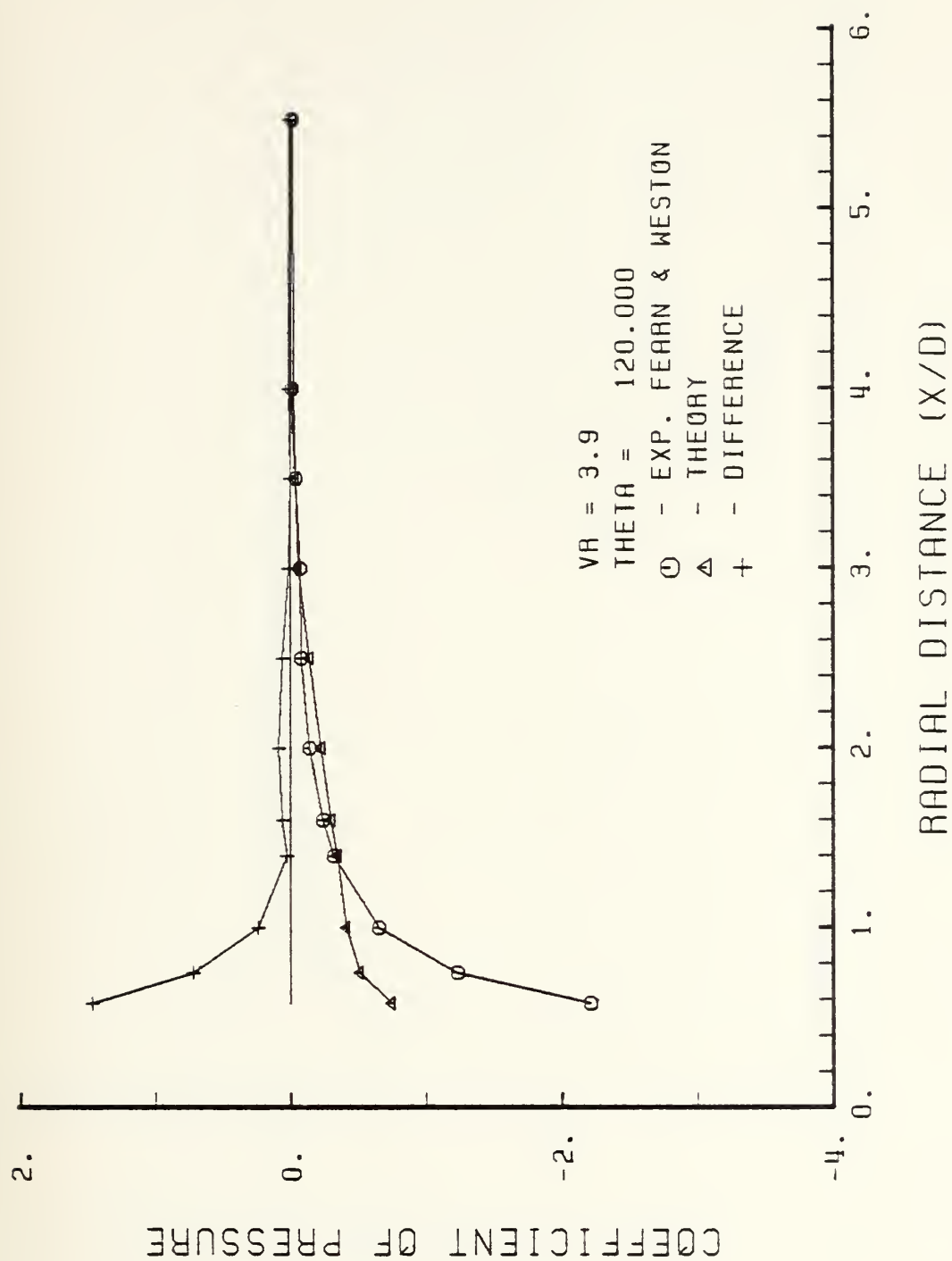


Figure C-36.  $C_p$ 's along radial lines, VR = 3.9, theta = 120 degrees.



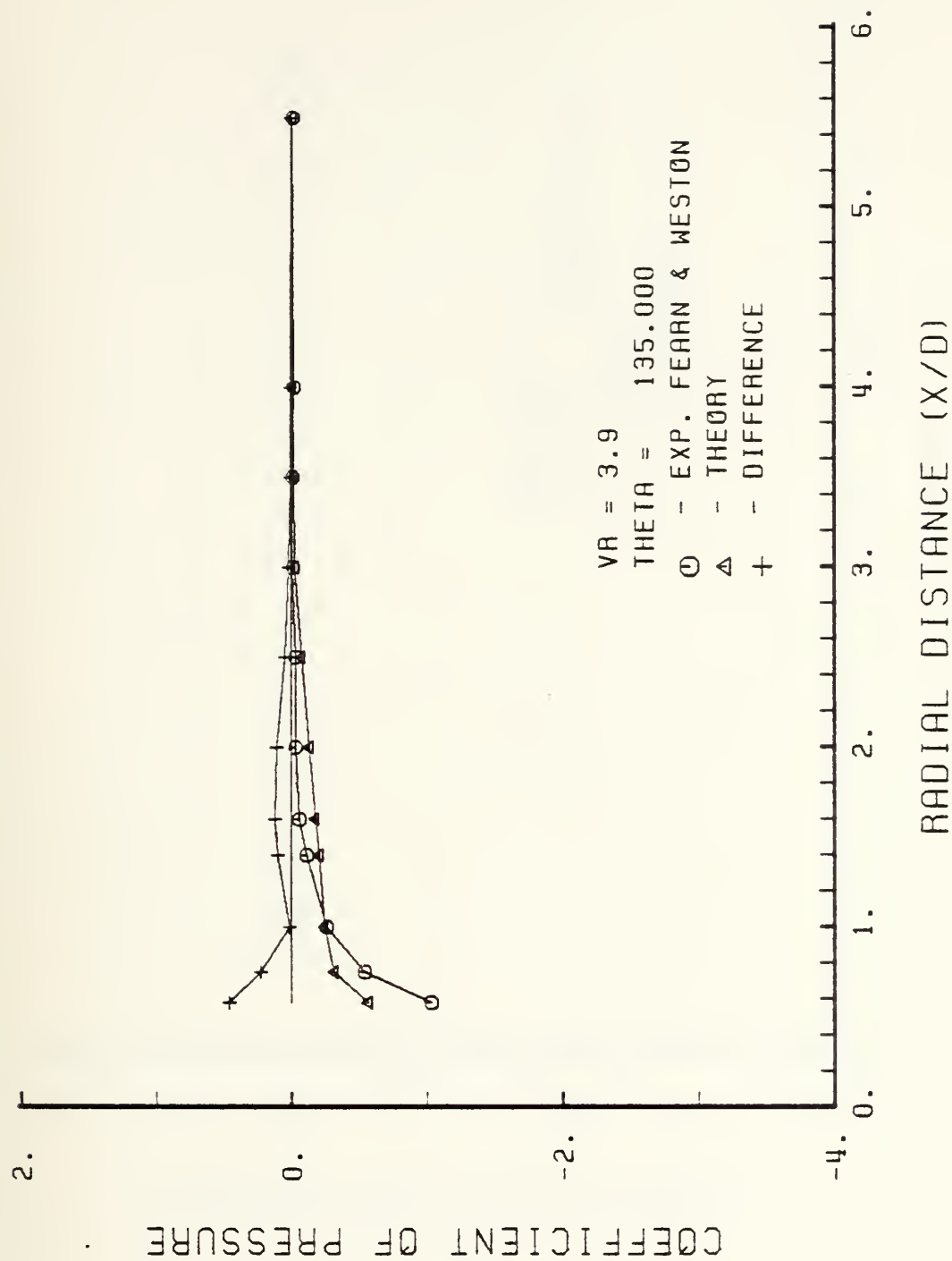


Figure C-37.  $C_p$ 's along radial lines, VR = 3.9, theta = 135 degrees.





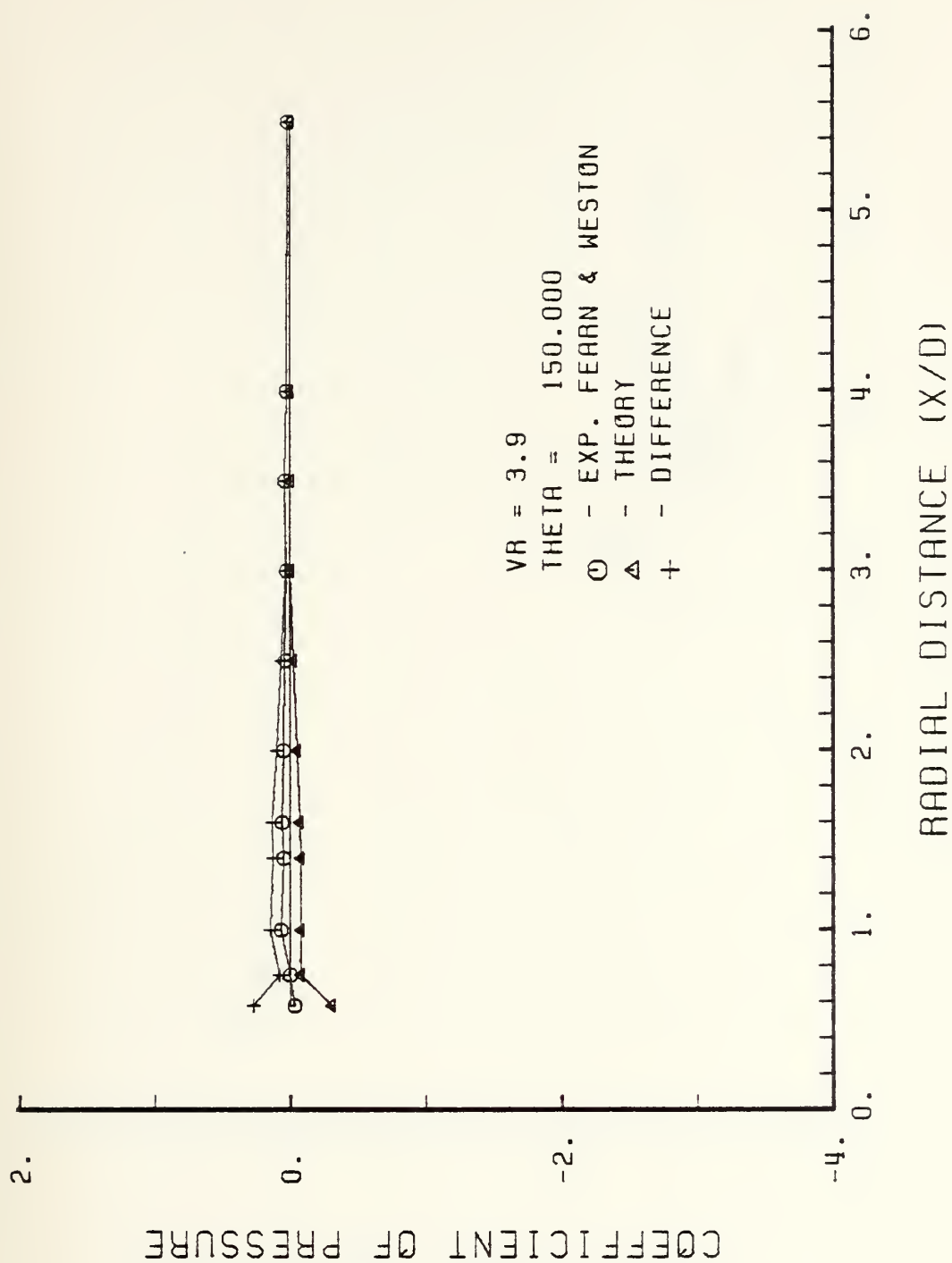


Figure C-38.  $C_p$ 's along radial lines, VR = 3.9, theta = 150 degrees.



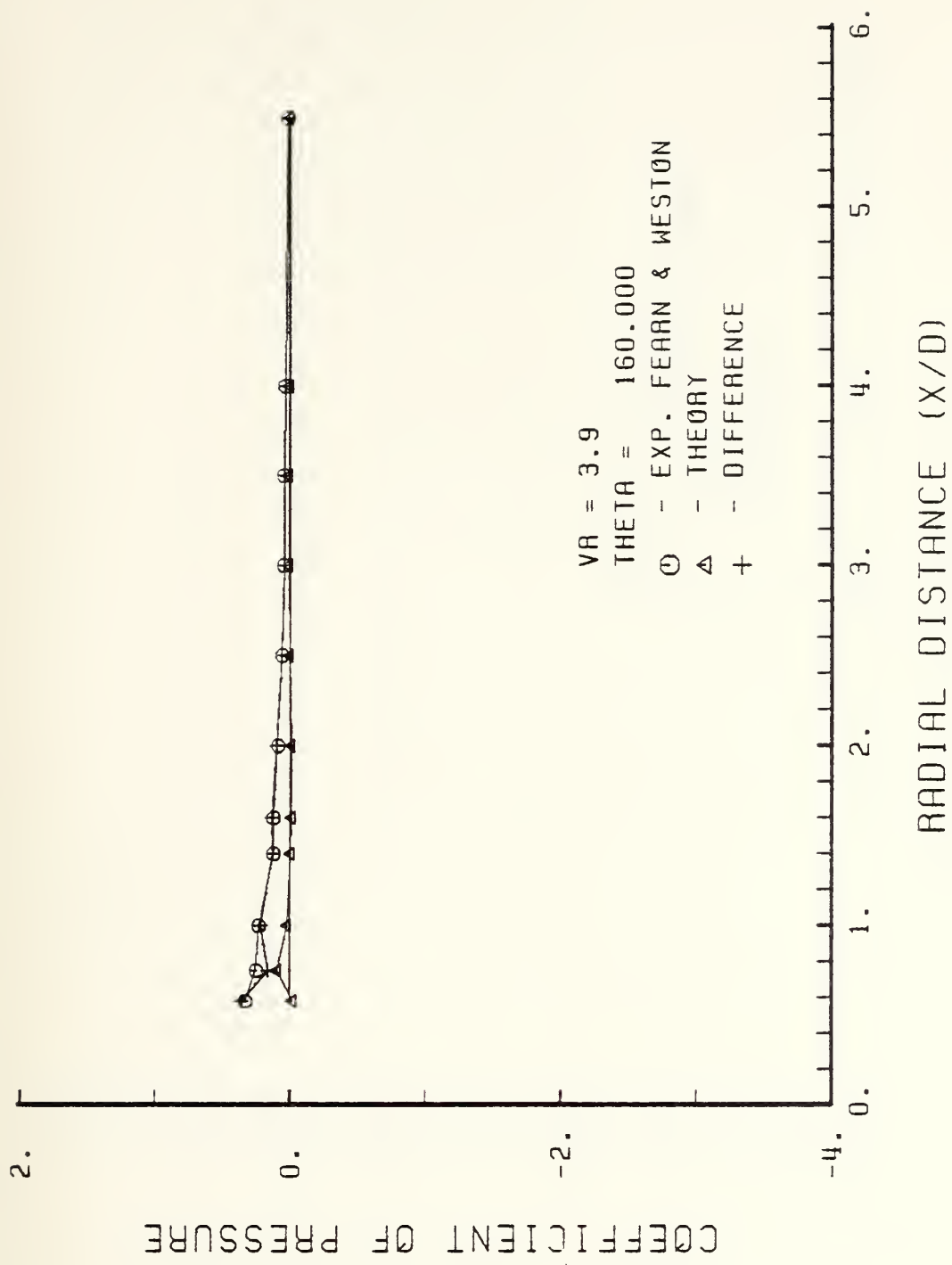


Figure C-39.  $C_p$ 's along radial lines, VR = 3.9, theta = 160 degrees.



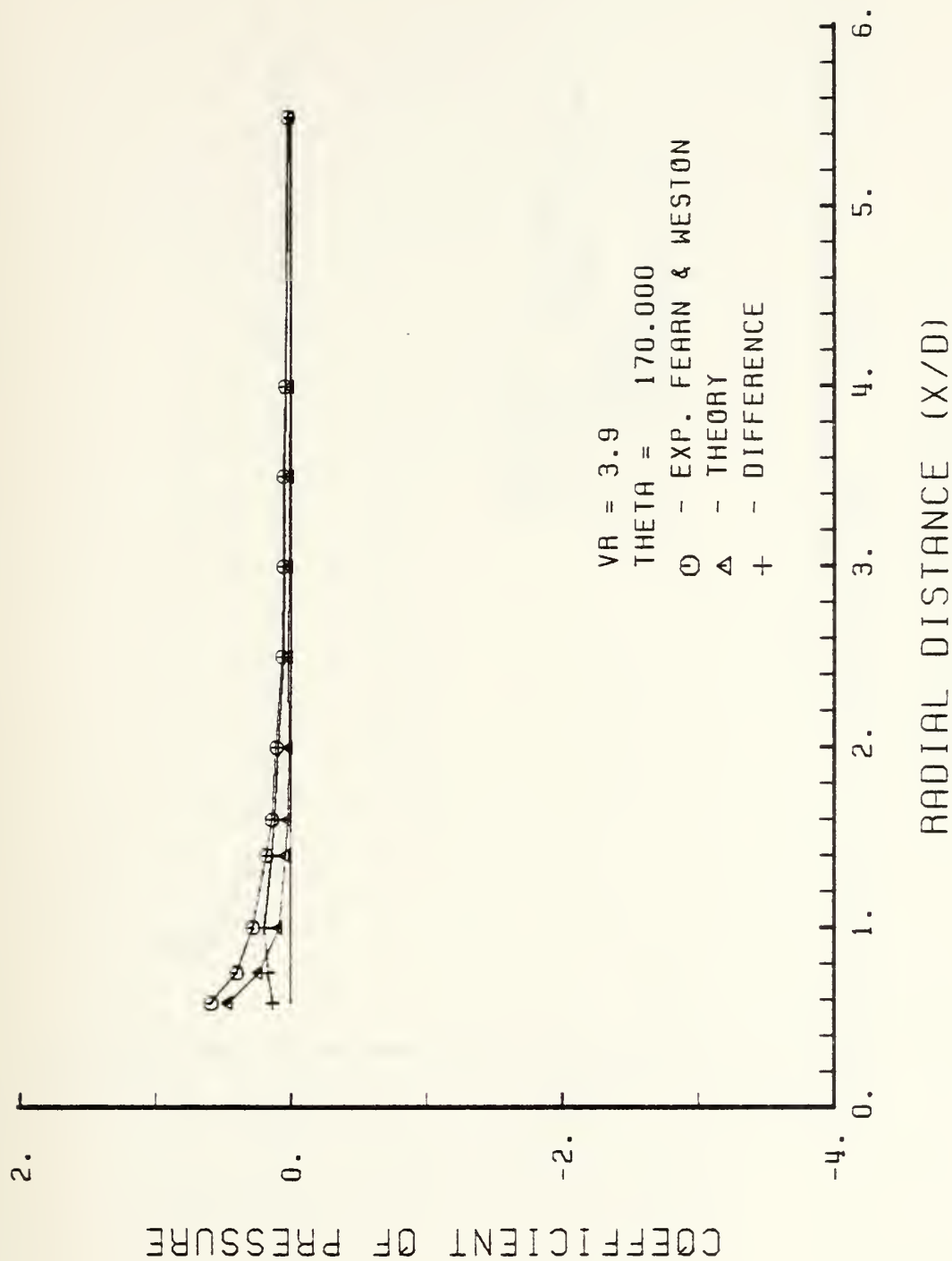


Figure C-40.  $C_p$ 's along radial lines, VR = 3.9, theta = 170 degrees.



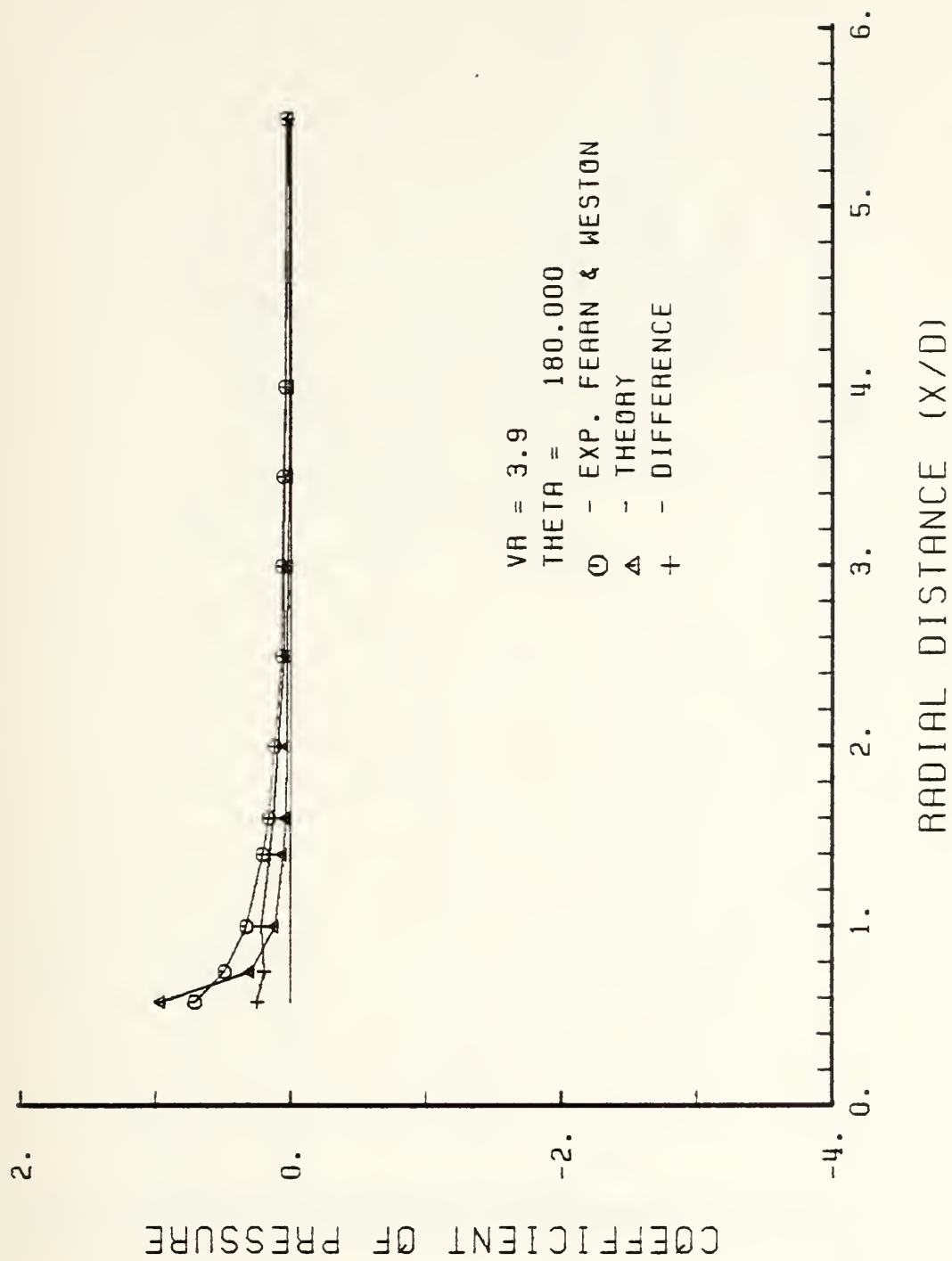


Figure C-41.  $C_p$ 's along radial lines,  $VR = 3.9$ ,  $theta = 180$  degrees.





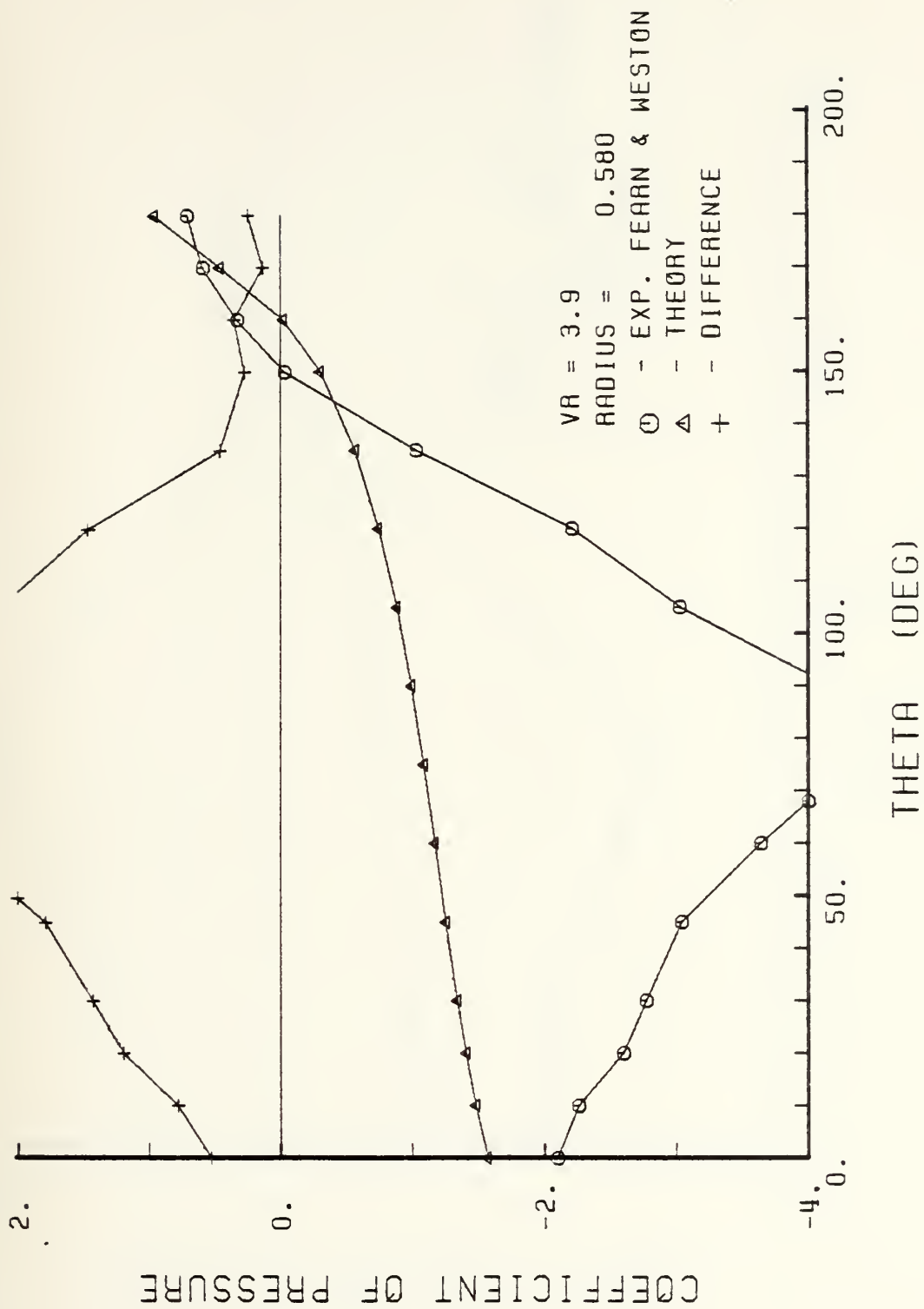


Figure C-42.  $C_p$ 's along circumferential arcs, VR = 3.9, radius = .58 dia.



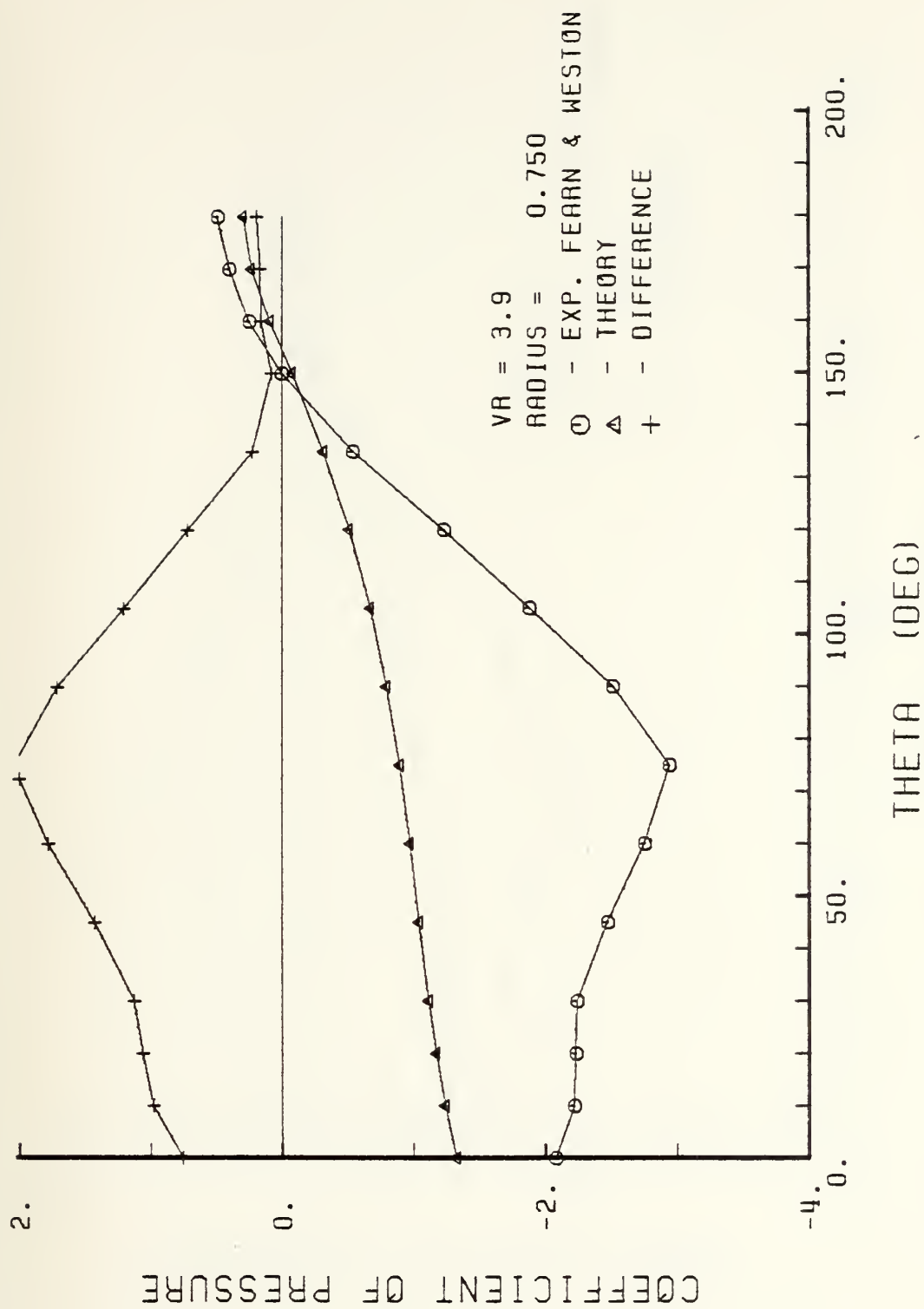


Figure C-43.  $C_p$ 's along circumferential arcs, VR = 3.9, radius = .75 dia.



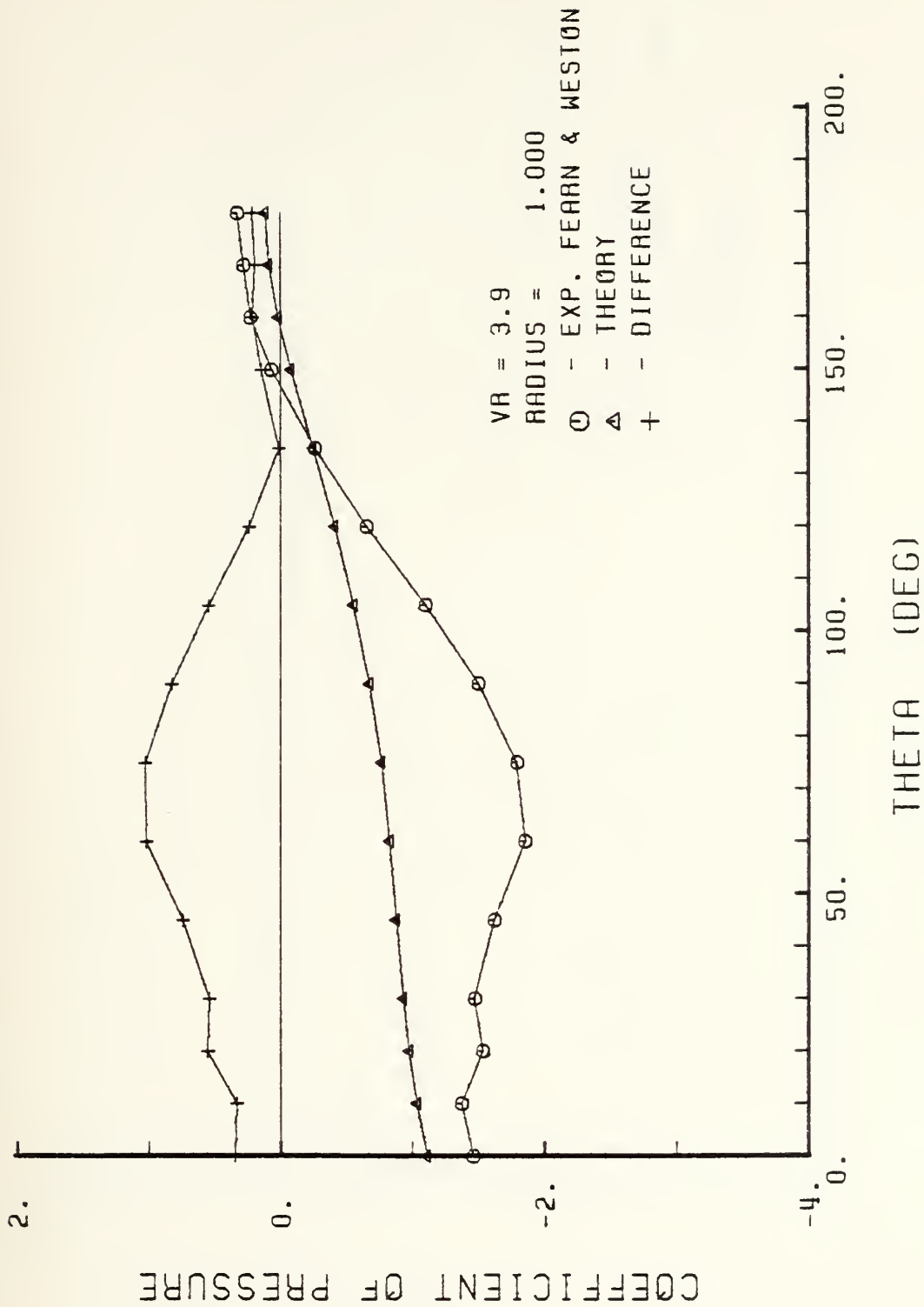


Figure C-44.  $C_p$ 's along circumferential arcs, VR = 3.9, radius = 1 dia.



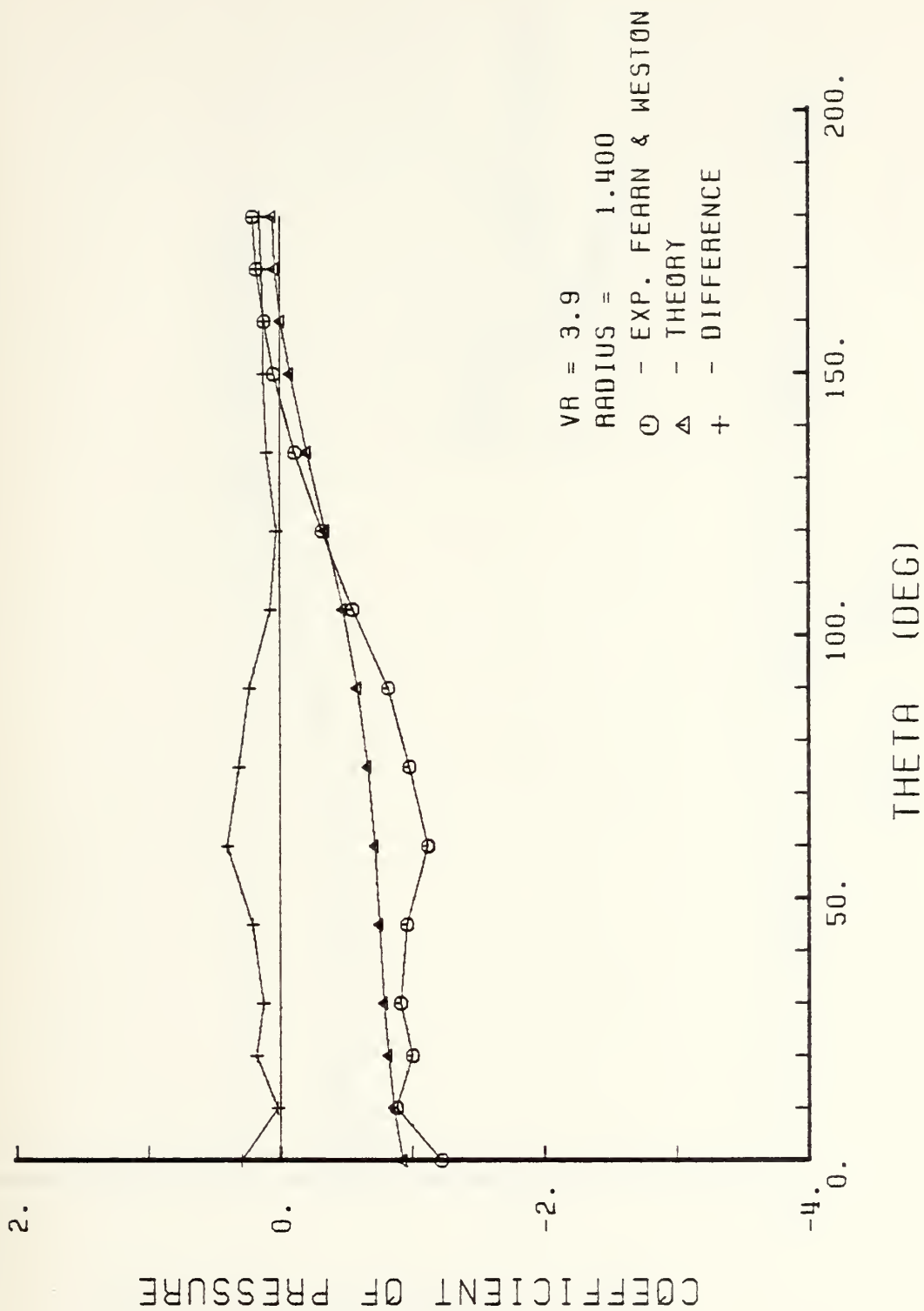


Figure C-45.  $C_p$ 's along circumferential arcs, VR = 3.9, radius = 1.4 dia.





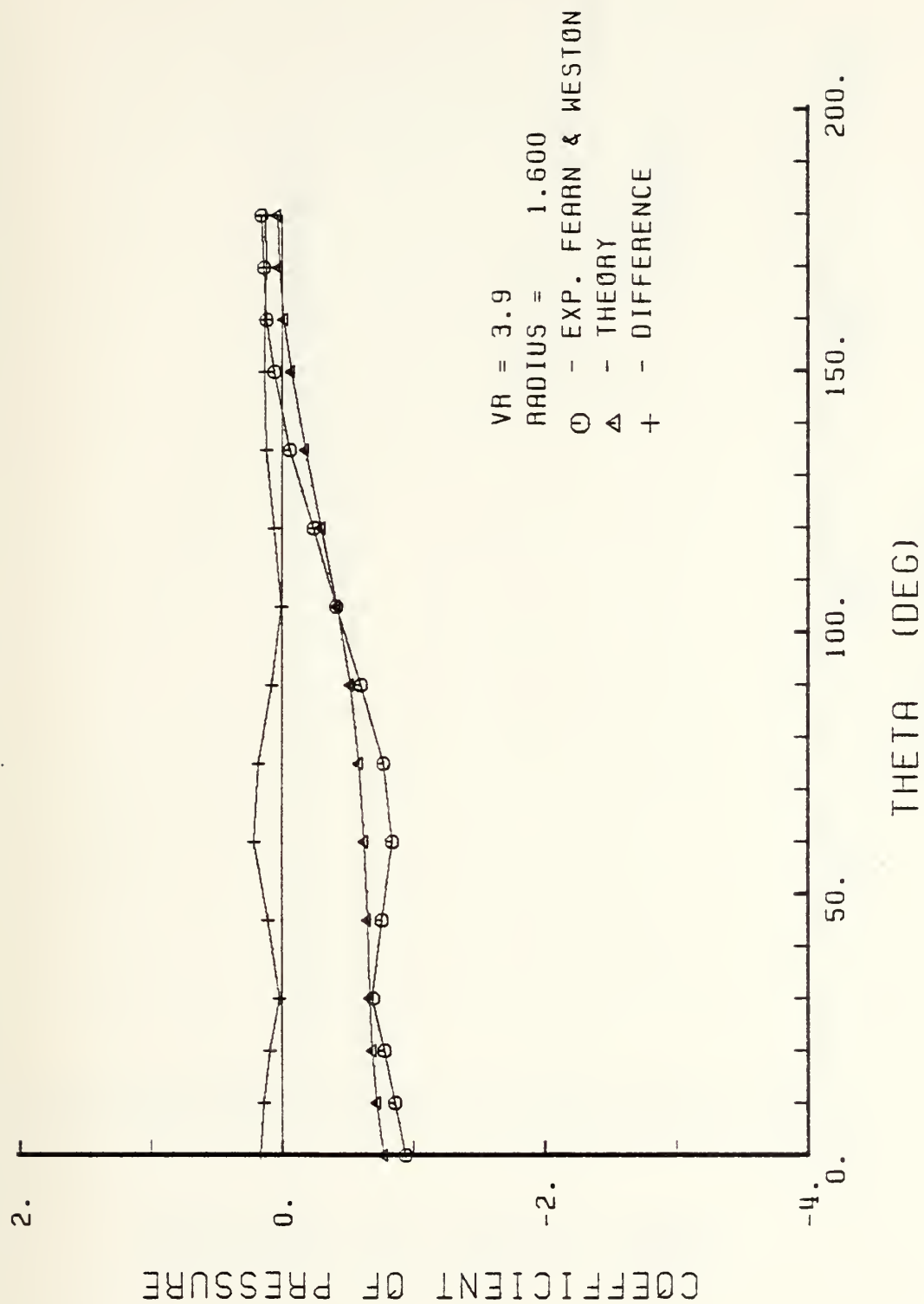


Figure C-46.  $C_p$ 's along circumferential arcs, VR = 3.9, radius = 1.6 dia.



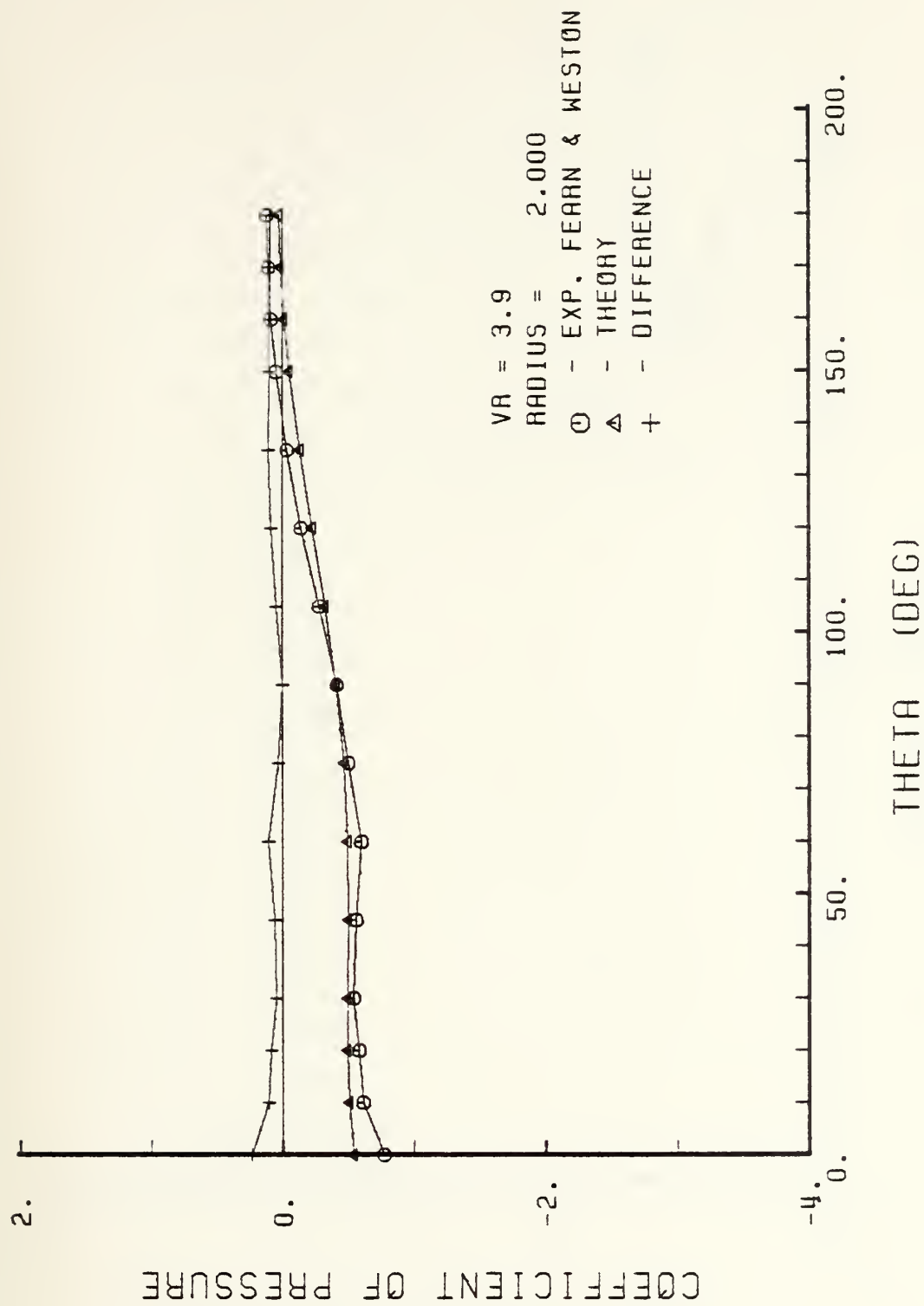


Figure C-47.  $C_p$ 's along circumferential arcs, VR = 3.9, radius = 2 dia.



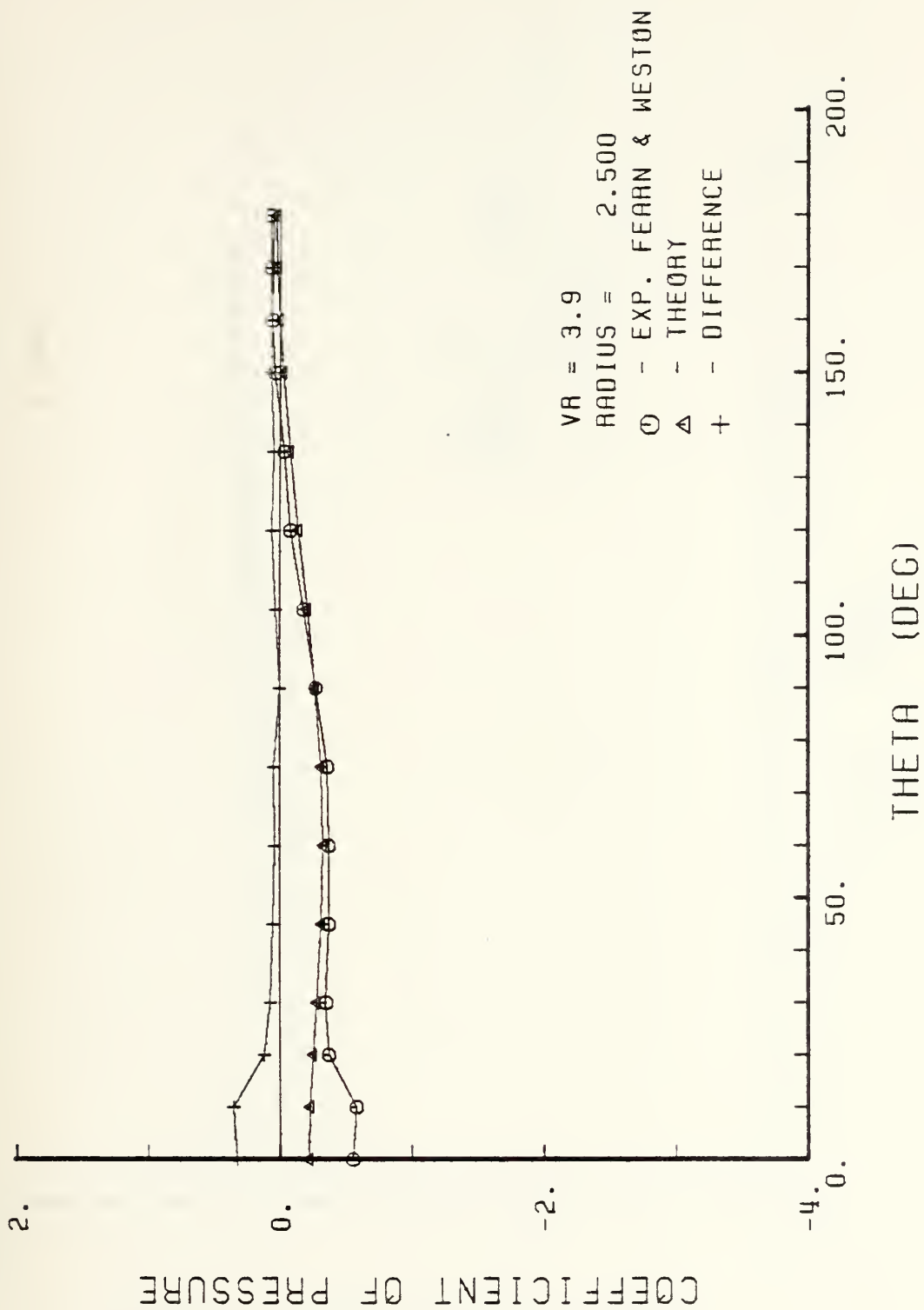


Figure C-48.  $C_p$ 's along circumferential arcs, VR = 3.9, radius = 2.5 dia.



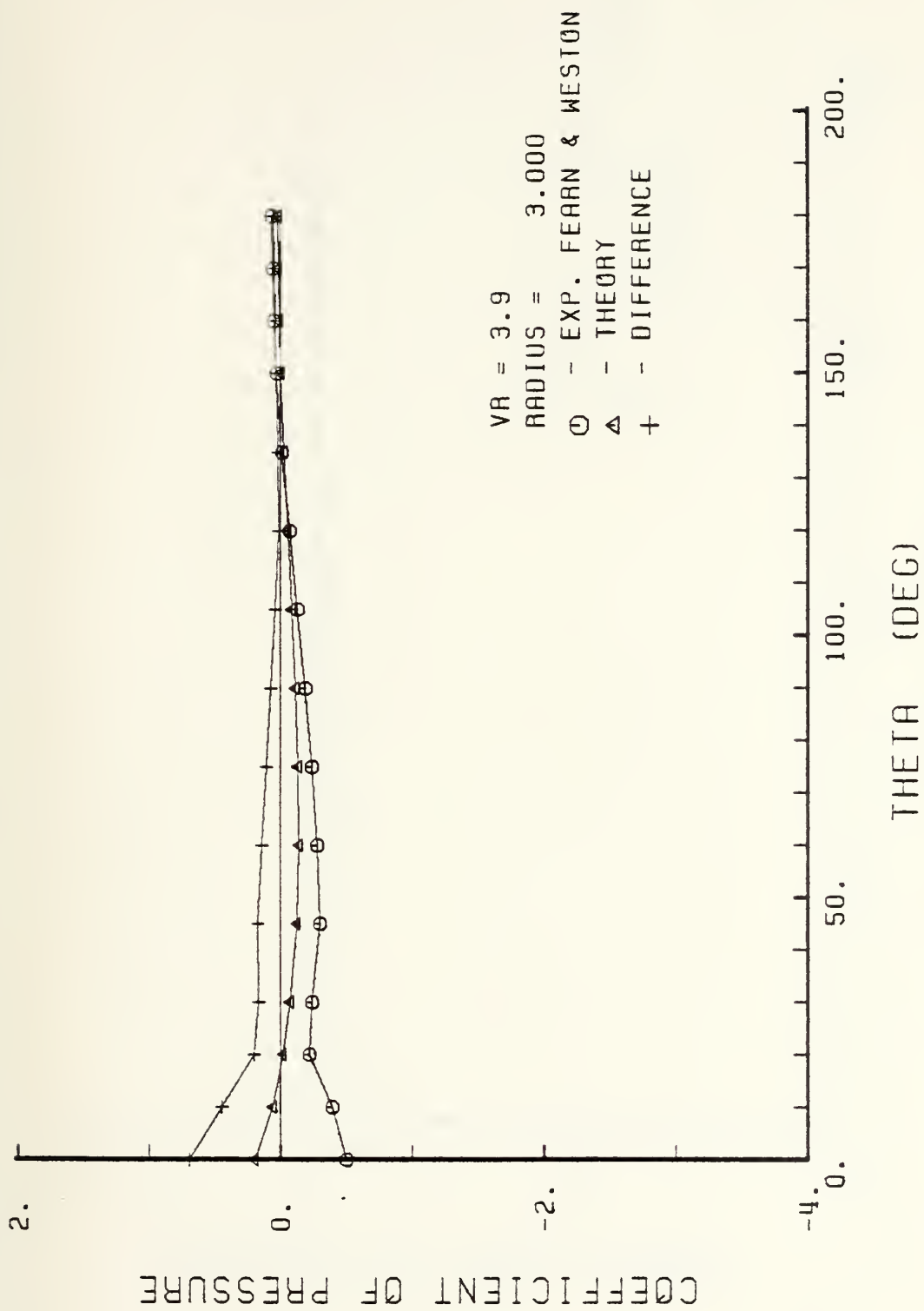


Figure C-49.  $C_p$ 's along circumferential arcs, VR = 3.9, radius = 3 dia.





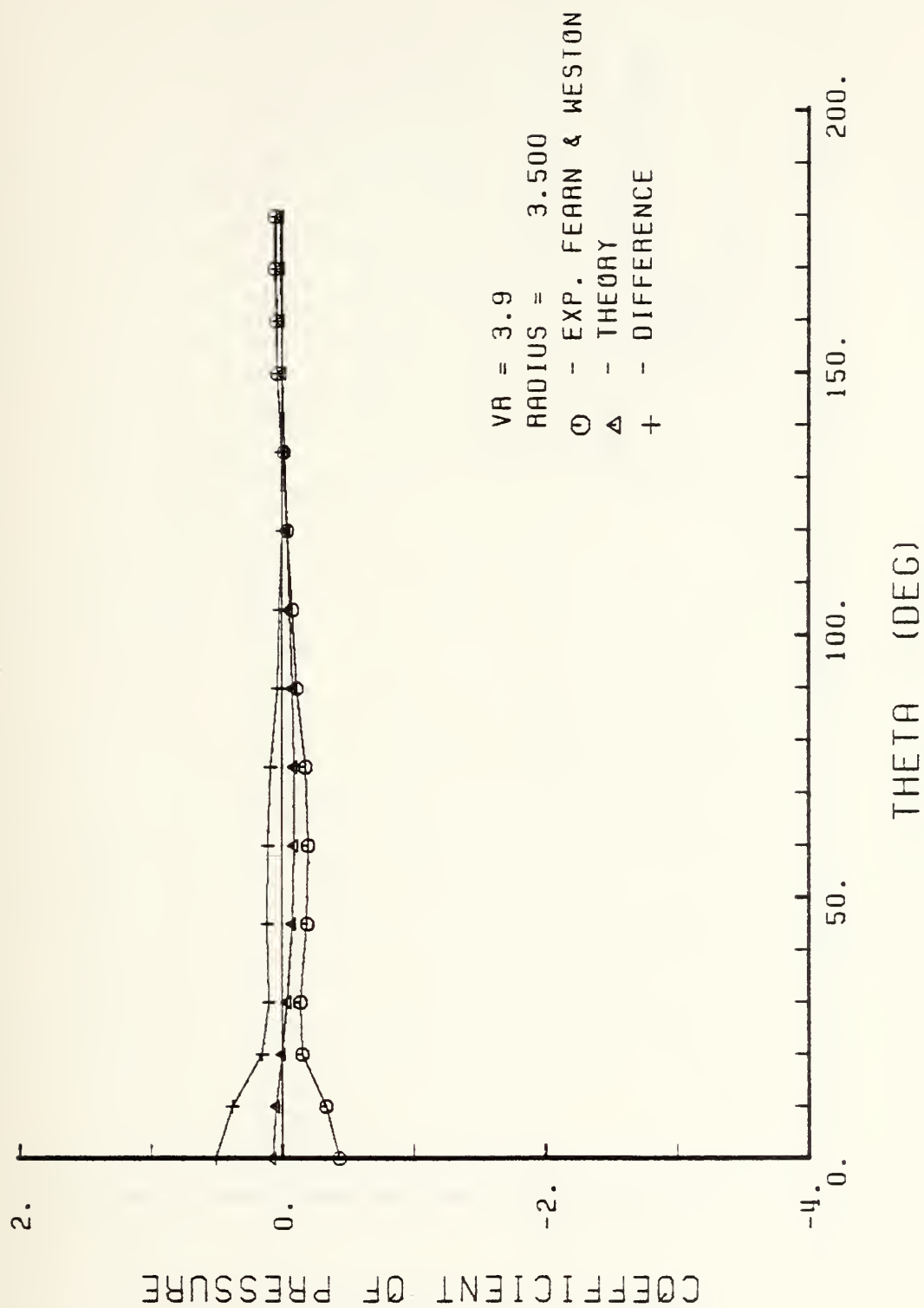


Figure C-50  $C_p$ 's along circumferential arcs, VR = 3.9, radius = 3.5 dia.



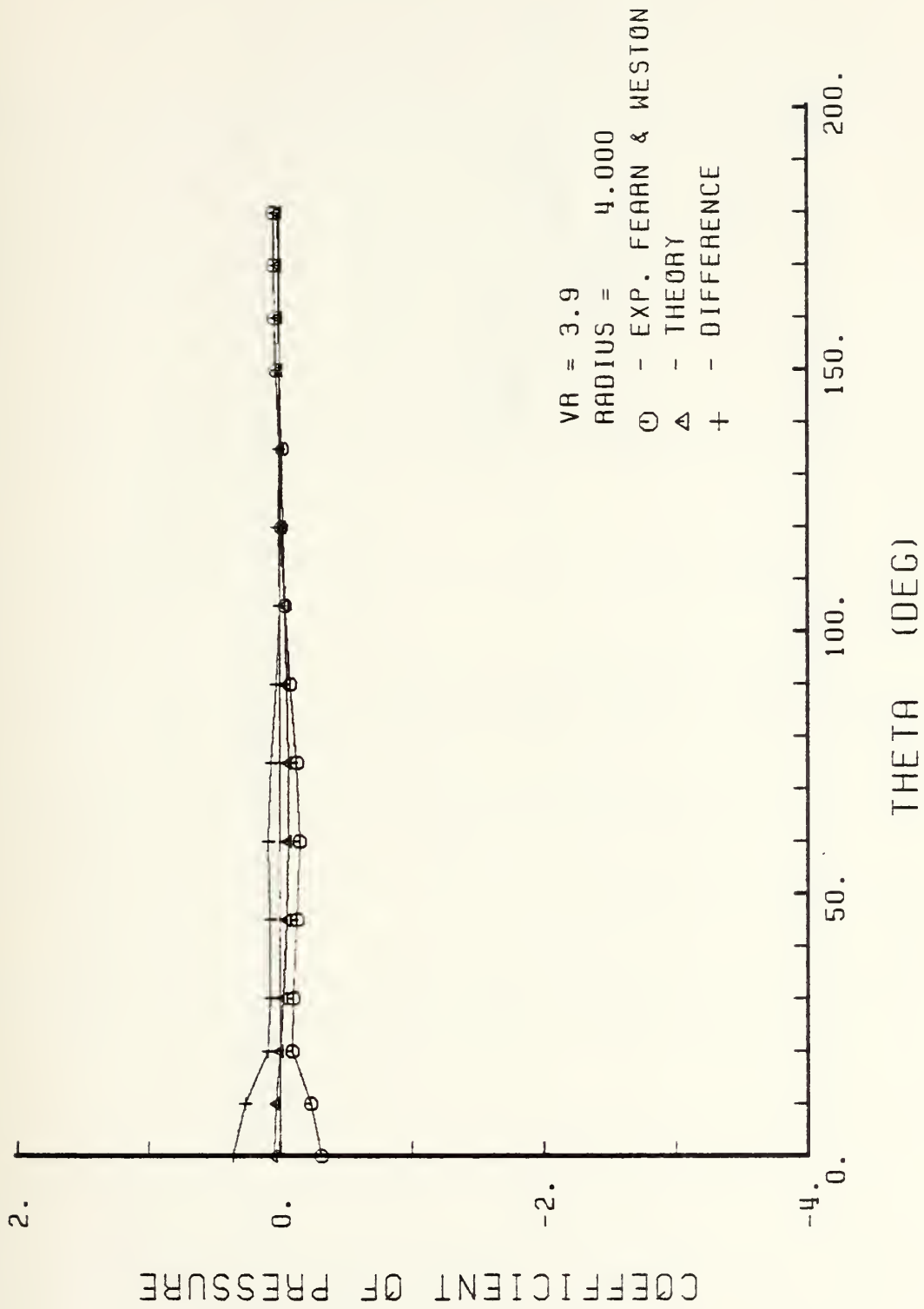


Figure C-51.  $C_p$ 's along circumferential arcs, VR = 3.9, radius = 4 dia.



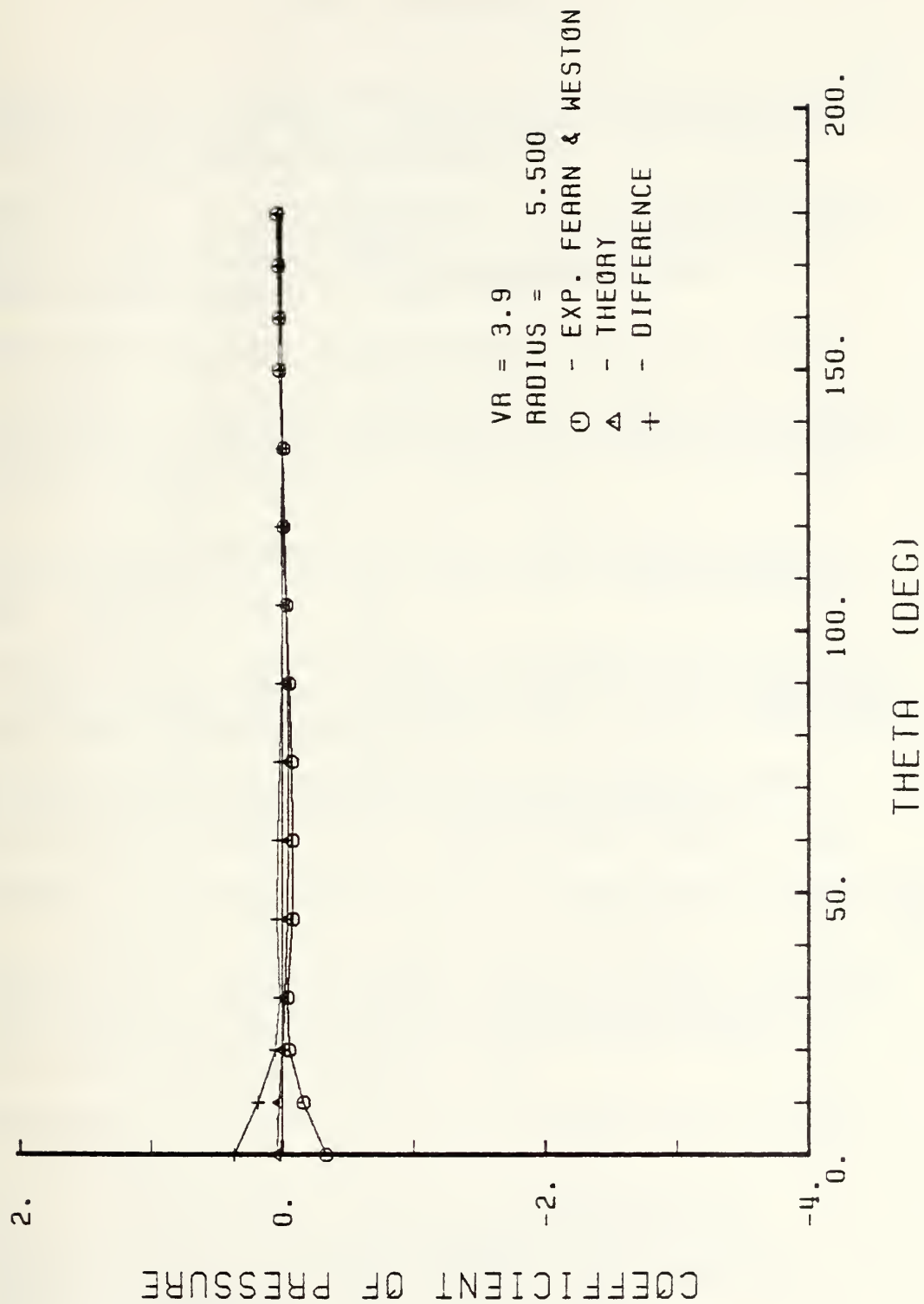


Figure C-52.  $C_p$ 's along circumferential arcs, VR = 3.9, radius = 5.5 dia.



## LIST OF REFERENCES

1. English, J. W., "The Design and Performance of Lateral Thrust Units for Ships, Hydrodynamic Considerations", R.I.N.A. Quarterly Transactions, Vol. 105, 1963
2. Chislett, M. S. and Bjorheden, O., "Influence of Ship Speed on the Effectiveness of a Lateral-Thrust Unit" Hydro-og Aerodynamisk Hydro-og Aerodynamisk Laboratorium Report No. Hy-8, 1966
3. Principles of Naval Architecture, S.N.A.M.E., 1967
4. Bradbury, L. J. S. and Wood, M. N., "The Static Pressure Distribution Around a Circular Jet Exhausting Normally from a Plane Wall into an Airstream", C.P. No. 822, British A.R.C., 1965
5. Fearn, R. L. and Weston, R. P., "Induced Pressure Distribution of a Jet in a Crossflow" NASA Technical Note NASA TN D-7916, 1975
6. Wooler, P. T., "On Flow Past a Circular Jet Exhausting at Right Angles from a Flat Plate or Wing", Journal of the Royal Aeronautical Society, Vol. 71, No. 675, 1967
7. Waterman, B. W., "Analysis of Jet-Crossflow Interactions with Application to Ship Bow Thrusters", Unpublished thesis, Naval Postgraduate School, 1980
8. Keffer, J. F. and Baines, W. D., "The Round Turbulent Jet in a Crosswind", Journal of Fluid Mechanics, Vol. 15, 1963
9. Schmidt, H., "Aenderung einer Parallelstromung entlang einer ebenen Platte durch einen quer gerichteten Freistrah", Zeitschrift fur Flugwissenschaften und Weltraum forschung, Sept/Oct 1979
10. Jordinson, R., "Flow in a Jet Directed Normal to the Wind", R&M No.3074, Brit. A.R.C., 1958
11. Wu, J. C. and Wright, M. A., "A Blockage-Sink Representation of Jet Interference Effects for Noncircular Jet Orifices" Analysis of a Jet in a Subsonic Crosswind, NASA SP-218, 1969





# INITIAL DISTRIBUTION LIST

	No. Copies
1. Defense Technical Information Center Cameron Station Alexandria, Virginia 22314	2
2. Library, Code 0142 Naval Postgraduate School Monterey, California 93940	2
3. Department Chairman, Code 69 Mx Department of Mechanical Engineering Naval Postgraduate School Monterey, California 93940	1
4. Professor R. H. Nunn, Code 69 Nn Department of Mechanical Engineering Naval Postgraduate School Monterey, California 93940	5
5. LCDR Bradford B. Waterman 468 Oak Street East Bridgewater, Massachusetts 02333	1
6. LCDR Thomas C. Cooper 1535 Green Valley Road Orangeburg, South Carolina 29115	1







Thesis

C75407 Cooper

c.1

Theoretical modeling  
of fluid interactions  
produced by ship bow  
thrusters.

197720

Thesis

C75407 Cooper

c.1

Theoretical modeling  
of fluid interactions  
produced by ship bow  
thrusters.

197720

thesC75407

Theoretical modeling of fluid interactio



3 2768 002 09417 9

DUDLEY KNOX LIBRARY